JAERI-M
84-049

DATA ON IONIZATION, EXCITATION, DISSOCIATION AND DISSOCIATIVE IONIZATION OF TARGETS BY HELIUM ION BOMBARDMENTS (I)

(TARGET IONIZATION, EXCITATION, DISSOCIATION AND DISSOCIATIVE IONIZATION INDUCED BY SEVERAL KeV TO 3.5 MeV HELIUM IONS INCIDENT ON A THIN GAS TARGETS)

March 1984

Nobuo ODA* and Junji URAKAWA*

日本原子力研究所
Japan Atomic Energy Research Institute

JAERI-Mレポートは，日本原子力研究所が不定期に公刊している研究報告書です。
入手の問合わせは，日本原子力研究所技術情報部情報資料課（〒319-11茨城県那珂郡東海村）あて，お申しこしください。なお，このほかに財団法人原子力弘済会資料センター（〒319-11 茨城県那珂郡東海村日本原子力研究所内）で複写による実費頒布をおこなっております。

JAERI-M reports are issued irregularly.
Inquiries about availability of the reports should be addressed to Information Section, Division of Technical Information, Japan Atomic Energy Research Institute, Tokai-mura, Naka-gun, Ibaraki-ken 319-11, Japan.

編集兼発行　日本原子力研究所
印　　刷　㈱高野高速印刷

Data on Ionization, Excitation, Dissociation and Dissociative Ionization of Targets by Helium Ion Bombardments (I).

(Target ionization, excitation, dissociation and dissociative ionization induced by several keV to 3.5 MeV helium ions incident on thin gas targets)

Nobuo ODA* and Junji URAKAWA*

This report presents a compilation of the experimental data on cross sections for the ionization, excitation, dissociation and dissociative ionization processes of targets in helium ion impacts on atoms and molecules under a single collision condition. These measurements were carried out in the energy range from several keV to 3.5 MeV. A systematic survey has been made on the literatures from 1975 to the end of 1982. A list of references is also given, including relevant papers published before 1975.

keywords : Ionization, Excitation, Dissociation, He Ash, A&M Data, Fusion

---

This work was supported by a research contract of Japan Atomic Energy Research Institut with Tokyo Institute of Technology in fisical year 1982.

* Tokyo Institute of Technology, Research Laboratory for Nuclear Reactor, Ookayama, Meguro-ku, Tokyo 152

ヘリウムイオン衝撃による標的の電離，励起，解離および解離性電離に関するデータ（Ⅰ）

（薄い気体標的に入射した数keV～3.5MeVのヘリウムイオンによるターゲットの電離，励起，解離および解離性電離）

織田暢夫*・浦川順治*

（１９８４年２月１日受理）

この報告書は，ヘリウムイオンを原子分子に１回衝突の条件の下で衝撃した場合の標的の電離，励起，解離および解離性電離の諸過程の断面積の実験データを収集したものである。収集したデータのエネルギー範囲は，数keVから3.5MeVである。文献の調査範囲は１９７５年から１９８２年の終りまでであるが，関連した１９７５年以前の文献を含めて，リストとして加えている。

この報告は，昭和５７年度に日本原子力研究所より，東京工業大学に委託した調査報告書を改めてまとめたものである。

＊　東京工業大学

CONTENTS

目　　次

1. Introduction

The target ionization, excitation, dissociation and dissociative ionization processes are of importance in the understanding of many fields such as plasma physics, radiation physics, atmospheric physics and so on. Also their significance in more practical applications such as the design of particle accelerators, controlled thermonuclear devices and space vehicles became increasingly apparent. Especially in magnetically-confined fusion plasma, the ionization and excitation processes are responsible for the plasma-cooling due to ejected cold electrons[1)] and the photon emission.

In this report a compilation is made systematically of the experimental data on cross sections for the ionization, excitation, dissociation and dissociative ionization processes of targets in helium ion impacts on atoms and molecules under the single collision condition. These measurements were carried out in the energy range from several keV to 3.5 MeV. A systematic survey has been made on the literatures from 1975 to the end of 1982.

2. Related Collision Processes

In a He^+-Atom interaction, the following changes can take place in the charge states of a projectile and a target atom (see Table I): 1) Capture of one electron by He^+ with removal of a part of target electrons to the continuum state; 2) Excitation of the target atom or elastic scattering. Target ionization with removal of a part of target electrons to the continuum state; 3) Projectile ionization with removal of a part of the target electrons to the continuum state.

Table I. Elementary processes with change of the charge states of the projectile and the target atom in the He^+-A interaction, where A is the target atom.

No	Reaction Process		Name of Process
1)	$He^+ + A \rightarrow He^0 + A^{n+} + (n-1)e$	for $n \geq 1$	Single charge transfer (n=1) Single charge transfer with electron production ($n \geq 2$)
2)	$He^+ + A \rightarrow He^+ + A^{n+} + ne$	for $n \geq 0$	Excitation or Elastic scattering (n=0) Ionization ($n \geq 1$)
3)	$He^+ + A \rightarrow He^{++} + A^{n+} + (n+1)e$	for $n \geq 0$	Pure stripping (n=0) Ionization with stripping ($n \geq 1$)

In the He^{++}-Atom interaction, the following changes can occur in the charge states of the projectile and the target (see the table II): 1) Double electron capture with removal of (n-2) electrons to the continuum state; 2) Single electron capture with removal of (n-1)

electrons to the continuum state; 3) Excitation of the target atom or elastic scattering. Target ionization with removal of n electrons of target electrons to the continuum state.

Table II. Elementary processes with change of the charge states of the projectile and the target atom in the He^{++}-A interaction.

No	Reaction Process		Name of Process
1)	$He^{++}+A \rightarrow He^{0}+A^{n+}+(n-2)e$	for $n \geq 1$	Double charge transfer (n=2) Double charge transfer with electron production ($n \geq 3$)
2)	$He^{++}+A \rightarrow He^{+}+A^{n+}+(n-1)e$	for $n \geq 1$	Single charge transfer (n=1) Single charge transfer with electron production ($n \geq 2$)
3)	$He^{++}+A \rightarrow He^{++}+A^{n+}+ne$	for $n \geq 0$	Excitation or Elastic scattering (n=0) Ionization ($n \geq 1$)

For molecular targets, it is to be noted that the above processes may be accompanied by dissociation. If A is a diatomic molecule, the following reactions occur:

$$A^{n+} \rightarrow \begin{cases} (BC)^{n+} & \text{---------- Nondissociation} \\ B^{m+}+C^{l+} & \text{for } m+l=n \text{ ---------- Dissociation} \end{cases}$$

, where A=BC.

In all the processes mentioned above, the excitation of either the target and/or the projectile may be included. However, in this report, the survey on the experimental data is limited to cross sections for the

changes of the states of the target atom and molecules, that is, cross sections for the slow ion production, the electron production, the excitation, dissociation, and dissociative ionization of targets. As can be seen from Tables I and II, the measurement of a physical quantity is related to many kinds of elementary processes. Therefore it is necessary to evaluate the measured cross sections by taking account of experimental methods used.

3. Experimental Methods

Experimental methods are classified into the following groups according to their characteristics:

1) Condenser method

Secondary slow ions and electrons are collected by the condenser plates in order to measure the ion and electron current intensities. The cross sections for the secondary ion production σ_+ and the electron production σ_- are determined from these intensities. When the projectile is a fully stripped ion, $(\sigma_+ - \sigma_-)$ is equal to the capture cross section σ_c.

2) Measurement of the partial secondary ion production cross section

The slow ions are extracted from the collision cell filled with the target gas and analyzed with a mass-spectrometer. The total cross section for the production of slow ions is measured using the condenser method. The partial cross section for the production of slow ions with different charge is determined from the ratio of line intensities in the mass spectrograms.

3) Double-differential cross section measurement

The double-differential cross sections (DDCS), differential in energy and angle of ejected-electrons or outgoing ions, are obtained through the measurement of the energy and angular distributions of electrons or ions using the electrostatic energy analyzer at various angles. The total electron production cross sections are obtained from the DDCS by integration with respect to both ejected-electron energy and emission angle. Also, the cross sections for an inner-shell vacancy production, the cross sections for autoionization and electron loss cross sections for fast projectiles are derived from the DDCS for ejected electrons by integration over emission angle and over

the energy in the vicinity of the corresponding Auger peak*, autoionization peak and loss peak, respectively, after subtraction of the continuum background from DDCS. On the other hand, the elastic scattering cross sections and the excitation cross sections are also derived by integration over scattering angle and over energy in the vicinity of the elastic peak and the corresponding excitation peak, respectively, after subtraction of the continuum background from the DDCS for the projectile.

* (This is the case when the fluorescence yields of target atoms are much less than unity. Otherwise, the results have to be corrected for the fluorescence yields.)

4) Emission cross section measurement

Cross sections for the excitation processes are obtained by measuring light intensities resulting from the decay of the excited target atom (molecule) or the excited ion to its ground state, taking account of cascading processes.

5) Measurements of the energy or charge state distribution of secondary ions using a time of flight (TOF) technique

By measuring the time of flight of secondary ions which are accelerated after extracted from the collision region, secondary ions can be separated according to their mass to charge ratios and the kinetic-energy spectra for each are recorded. This technique is also applied to the measurement of the dissociative ionization process of target molecules.

6) Coincidence detection

The pure ionization cross section is determined by means of the detection of product ions in coincidence with the electrons generated from the same events. The coincidence technique is also applied to

studies of non-dissociative and dissociative ionizations. Cross sections σ_{ni} for nondissociative ionization and cross sections σ_{di} for dissociative ionization are separately determined. Cross sections for the target inner-shell ionization and for the electron capture from the target inner-shells, differential in projectile scattering angle, are derived by measuring the scattered-projectiles in coincidence with the Auger electrons or the x-rays.

The cross sections for the elementary processes are determined by simultaneous analysis of the charge states of states of the projectile and the products after the collision with the coincidence technique.

4. Target Ionization

The total cross sections measured by the condenser method, for the formation of slow positive ions σ_+ and for the formation of free electrons σ_-, are related to the cross section for target ionization σ_i, the loss cross section σ_l, and the cross section for electron capture by projectile ion σ_c as follows:

$$\sigma_+ = \sigma_i + \sigma_c$$

$$\sigma_- = \sigma_i + \sigma_l.$$

For fast He^{++} ions we have $\sigma_l=0$

$$\sigma_- = \sigma_i,\ \sigma_c = \sigma_+ - \sigma_-.$$

For fast He^+ ions, free electrons are produced both by ionization of the target and by stripping (ejection of electrons from the projectiles into the continuum): $\sigma_- = \sigma_i + \sigma_l$.

Measurements on σ_l have been obtained by Allison et al.[2] (1956), Jones et al.[3] (1959), Pivovar et al.[4] (1962), and Shah et al.[5] (1977). In the energy region from several keV to one hundred keV, σ_l is often very small compared to σ_c and strongly decreases with decrease of impact energy. On the other hand, since the data of Dmitriev et al.[6] (1962) for the σ_l show that σ_l is by several dozen times larger than σ_c at collision energies above 1500 keV, the difference $\sigma_- - \sigma_+$ can be equated, without great error, to σ_l, for collision energies higher than about 1000 keV.

In this section, total cross section measurements by the condenser method done before 1974 are briefly reviewed and cross sections related to the target ionization are compiled from the literatures published in from 1975 to the end of 1982.

Keene[7] (1949), Fedorenko et al.[8] (1957), Gilbody and Hasted[9] (1957), and de Heer et al.[10] (1957) measured the (apparent) electron capture

cross sections σ_c and the (apparent) ionization cross sections σ_- for many kinds of positive ions (involving He^+) impacts on hydrogen, nitrogen and rare gas in the energy range of a few keV to 180 keV without the use of an axial magnetic field. Slow ions or electrons formed along a beam path were extracted by a transverse electrostatic field and the saturation currents were measured. The corresponding cross sections were derived from the values of these currents, the pressure, the beam current, and the path length. Also, Keene[7] made a magnetic analysis of the slow ions in order to provide the information on the collision products. Fedorenko et al.[8] used a method of detecting fast neutral atoms produced in the ion beam to determine the capture cross section σ_c and estimated the loss cross section σ_1 by inserting values of σ_c so obtained into σ_+ and σ_- measured by the condenser method. de Heer et al.[10] also carried out the direct measurement of loss cross section σ_1.

Gilbody et al.[11] (1963) and de Heer et al.[12] (1966) determined the (apparent) capture cross section σ_c, the total electron production cross section σ_- and the total slow ion production cross section σ_+ for rare gas ions incident on rare gases and hydrogen in the energy range 60 to 450 keV and for helium ions incident on noble and diatomic gases between 10 and 140 keV, respectively, using the condenser method with an axial magnetic field. Gilbody et al.[11] thought that the measurement of the total current to a pair of plates over a definite path length yields the cross section corresponding to σ_c and the measurement of the total positive ion current yields the cross section corresponding to σ_+, and the cross section σ_- is obtained by the relation $\sigma_-=\sigma_+-\sigma_c$. de Heer et al.[12] took into consideration the contribution of σ_1 to σ_-, and, since σ_1 was very small compared to σ_c, neglected σ_1 in the derivation of σ_-.

The cross sections for the productions of slow positive ions and of free electrons by ionization of the gases H_2, N_2, He, Ne, Ar and Kr with He^+ ions were measured in the energy interval 0.2-1.8 MeV by Pivovar et al.[13] (1968). They used, for comparison, two kinds of methods to suppress the secondary electron emission: a method using a screening grid with large transparency, located ahead of the collecting plates, and a method using a magnetic field produced by Helmholtz coils and directed parallel to the beam of primary ions. Comparison of the results obtained with two methods showed that the cross sections σ_+ was the same, within experimental errors, for two methods. On the other hand, for the cross sections σ_-, differences were observed between two methods for light gases (hydrogen and helium). Their comparison of two methods to suppress the secondary electrons showed that the screening grid method is more accurate than the longitudinal magnetic field method for determination of the cross sections σ_+ and σ_-.

Langley et al.[14] (1964) and Puckett et al.[15] (1969) reported the measurement of apparent cross sections for production of slow positive ions σ_+ and of free electrons σ_- by helium ions incident on He, Ne, Ar, H_2, N_2, O_2, and CO in the energy range 0.1 to 1.0 MeV using the conventional condenser plates.

Fedorenko and Afrosimov[16] (1957) determined the cross sections for the production of slow ions with different charge from the ratio of line intensities in the mass spectrograms and the total cross sections for the production of slow ions measured using the condenser method. The measurements were made of the slow ions which were produced in single collisions of He^+, Ne^+ and Ar^+ ions with energies from 3 to 180 keV with helium, neon, argon, and krypton. Solov'ev et al.[17] (1964) also measured σ_+ and the cross sections for the production of slow ions with

different e/m ratios produced by ionization of helium, argon, hydrogen, and nitrogen gases by fast 15-180 keV He atoms and He^+ ions with a mass-spectrometric analysis of the slow ions. The measurements of ionization cross sections (σ_+) and mass spectra produced by 2.2 MeV He^{++} particles impact on simple hydrocarbons, H_2, D_2, O_2, H_2O, and the rare gases were carried out with an α-particle ionization chamber specifically designed to observe primary mass spectra by Rudolph and Melton[18] (1966). The cross sections for formation of Ne^{n+}, Ar^{n+}, Kr^{n+} or Xe^{n+} ions (n=1,2,3) in collisions between He^{2+} ions and the rare gas atoms were measured in the energy region from 0.1 to 8 keV by Latypov et al.[19] (1970). They showed that the appearance of peaks in the cross sections as functions of collision energy in the case of the formation of Ar^{2+}, Kr^{2+}, Xe^{2+}, and Xe^{3+} ions was due to exothermal capture processes concomitant with ionization.

A modulated crossed-beam technique was used to study the ionization of potassium and sodium vapour by 20-100 keV H^+ and He^+ ions by O'Hare et al.[20] (1975). Absolute cross sections σ_- for electron production were determined from the gross yields of electrons using the condenser method. They used mass spectrometric measurements of the relative abundance of secondary ion species together with measurements of the total one-electron capture cross sections to determine cross sections for Na^+, K^+ and K^{2+} formation. The results for He^+ impacts are shown in Fig. 1 and Fig. 2.

Afrosimov et al.[21] (1975) measured directly the cross sections of all the elementary processes (see the Table 1) occurring in the collisions between He^{2+} ions and He atoms in energy region from 1 to 100 keV

with the simultaneous analysis of the charge states of the projectiles and target atoms after collision by the coincidence technique. Fig. 3, Fig. 4, and Fig. 5 show cross sections of the process(2002), the process (2011), and the processes(2022, 2021, 2012, and 2021+2012). Afrosimov et al.[22] (1980) also measured the cross sections for all elementary reactions (see Table 2) involving a change in charge state in He^{++}-H_2 collisions for He^{++} with energies 1.2-100 keV. The measurements were carried out by distinguishing an individual collision by a coincidence method and by simultaneously analyzing the charge states of the fast and slow particles. Furthermore, in the same event, the electronic states of the fast particles after the collision were determined by analyzing the kinetic energies of the resulting ions. The cross sections for the elementary reactions ((1) and (4) in Table 2) are shown in Fig. 6. Fig. 7 and Fig. 8 show the kinetic energy distributions and differential cross sections for the scattering of the fast He^+ ions formed in reaction 4, respectively. Furthermore, cross sections for elementary reactions (see Table 2 and figure captions) are shown in Fig. 9 and 10.

Shah and Gilbody[23),24)] (1981, 1982) determined cross sections for ionization of ground state hydrogen atoms and molecules by positive ions including 125-2200 keV He^{2+} ions using a crossed-beam coincidence technique. Collision products were identified by time-of-flight spectroscopy and counted in coincidence with electrons from the same ionizing events. Cross sections σ_{ni} for non-dissociative ionization and cross sections σ_{di} for the sum of the dissociative ionization channels were separately determined for target molecules H_2. A fast-ion coincidence technique was also used to show that the main contribution to these large values of σ_{di} comes from the transfer ionization process. Cross sections for H^+ and He^+ impact on H are shown in Table 3. Fig. 11

shows their experimental values normalized to values predicted by the first Born approximation at their highest energies (2.2 MeV) together with various theoretical values. The cross sections σ_{ni} and σ_{di} for non-dissociative and dissociative ionizations, respectively, of H_2 by H^+ and He^{2+} ions are given in Table 4. Also, Table 5 shows the transfer ionization cross sections σ_{ti}. The cross sections σ_{ni}, σ_{di} and σ_{ti}, together with total cross sections $\sigma_i=(\sigma_{ni}+\sigma_{di})$ for H^+ and He^{2+} ions in H_2 are shown in Fig. 12.

The absolute electron production cross sections for He^+ and He^{2+} impacts on argon in the energy range 0.3-2.0 MeV, differential in angle and energy of the ejected electrons, were reported by Toburen and Wilson[25] (1979). Ejected electron energy spectra were measured for emission angles from 15° to 125° and for ejected-electron energies from a few eV to several keV using a cylindrical-mirror electrostatic analyzer which has a solid acceptance angle of approximately 6×10^{-5} sr and an energy resolution of 3.5% (full width at half-maximum (FWHM)). The basic features of the electron energy spectra resulting from ionization of argon by He^+ and He^{2+} ions are illustrated for small and large emission angle in Fig. 13 and Fig. 14, respectively. Angular distributions of electrons of selected energies for 2.0-MeV, 1.2-MeV helium ion energies were presented in Fig. 15, Fig. 16, and Fig. 17, respectively. Also, to gain a clearer understanding of the effects of projectile stripping (electron loss) and continuum charge transfer, Toburen and Wilson made a comparison of angular distributions in Fig. 18 for electron energies at which the contributions of the above processes are maxima, i.e., where the velocities of the ion and ejected electron are same. The total electron production cross sections were obtained from the double-differential cross sections by integration with respect to both

ejected electron energy and emission angle. A comparison of their integrated electron emission cross sections with the corresponding cross sections for the formation of free electrons (σ_-) is shown in Fig. 19.

The absolute electron production cross sections for 20 keV H^+, 5-20 keV H_2^+ and 5-20 keV He^+ impacts on argon, differential in angle and energy of the ejected electrons, were measured for electron energies of 2-26 eV at ejection angles 30° and 90° by Sataka et al.[26] (1979). The ejected-electrons were energy analyzed by a 30° parallel plate electrostatic analyzer. The electrostatic analyzer has an energy resolution of 1.7% and an angular resolution of 2.3°. Fig. 20 shows the double-differential cross sections measured at 30° for 5, 10, 15 and 20 keV He^+ impacts on argon.

Toburen et al.[27] (1980) also measured yields of secondary electrons (δ rays), differential in ejected electron energy and emission angle, for 0.3 to 2.0 MeV helium ion impacts on water molecules in vapor phase. An example of the cross section surfaces obtained from these measurements in shown in Fig. 21, where cross sections for ionization of water vapor by 0.3 MeV/amu He^+ and He^{2+} ions are shown. A comparison of the ejected electron energy spectra for the highest and lowest energies of He^+ and He^{2+} ions is shown in Fig. 22 for selected electron emission angles. Angular distributions for emission of electrons of selected energies are shown in Fig. 23a for 0.075 MeV/amu He^+ ions and in Fig. 23b for 0.2 MeV/amu He^+ and He^{2+} ions. A comparison of He^+ and He^{2+} cross sections at 0.3 and 0.5 MeV/amu is given in Fig. 24 which shows effects of screening and projectile stripping similar to those for the lower ion energies given in Fig. 23a. The total ionization cross section, the mean electron energy, and the stopping cross section can be obtained by integration of the measured double-differential cross sections. A

compilation of the total ionization cross section, σ_T, the mean electron energy, $\bar{\varepsilon}$, and the stopping power due to the energy loss by the kinetic energy of secondary electrons, $\bar{\varepsilon}\sigma_T$, is shown in Table 6.

The measurements and calculations of the double-differential cross sections for electrons ejected by fast He^+ impacts on helium were performed using the measuring method described in the paper of Toburen and Wilson[25] and the first Born approximation, respectively, by Manson and Toburen[28] (1981). A typical example of calculated angular distributions near the equal velocity for electrons and ions is shown in Fig. 25 along with measured cross sections. Toburen et al.[29] (1981) discussed the dynamic screening by projectile electron in ion collisions using the data measured by Toburen and Wilson[25] and others. Fig. 26 shows single differential cross sections obtained by integration over electron emission angle of the measured double-differential cross sections for electrons ejected by He^+ and He^{2+} impacts on argon.

The autoionization of the helium atom was experimentally studied in He^+ + He collisions between 3 and 140 keV by Bordenave-Montesquieu et al.[30] (1982), using a 127° electrostatic analyzer of which the effective acceptance angle varies from 1.09×10^{-4} to 0.67×10^{-4} sr and the energy resolution varies from 1.1% to 0.67% depending on the slit width. Above 10 keV, the shapes and excitation cross sections of the $2s^2\ ^1S$, $2s2p\ ^3P$, $2p^2\ ^1D$ and $2s2p\ ^1P$ were determined by a numerical fitting procedure; below 10 keV the (^1D+^1P), and $2p^2\ ^1S$ line intensities were obtained by planimetry. Typical examples of agreement between the numerical fitting values and the measured double-differential cross sections are shown in Fig. 27, Fig. 28, and Fig. 29. Angular dependence of the excitation cross sections (single-differential cross sections) for the autoionization states of the helium atom is shown in Figs. 30-36. In these

figures, the kinematic corrections were taken into consideration in the excitation of the two collision partners. The projectile energy dependence of the excitation cross sections (the single-differential cross sections) is shown in Fig. 37 at θ_{lab} = 150° and 60° for the ^1D, ^1P, ^1S, and ^3P states. Fig. 38 shows the variation of the experimental total cross section for the excitation of the slow particle with collision energy. Total cross sections for the various autoionizing states in He^+ on He are given in Table 7. A comparison of the differential cross sections for emission of electrons by autoionization of the fast and slow particles leads to the conclusion that the quasimolecule model could not explain results observed above the collision velocity of about 0.5 a.u..

Tokoro et al.[31] (1982) reported experimental results on angular distributions of continuous electrons as well as autoionized electrons ejected from 20 keV He^+ impact on He in the angular range from 30° to 150° with respect to the incident ion beam, using the experimental apparatus and procedure described by Sataka et al.[26]. The angular dependence of excitation cross sections of autoionization states $2s^2\ ^1S$ and $2p^2\ ^1D + 2s2p\ ^1P$ were in good agreement with previous data measured by Bordenave-Montesquieu et al.[30]. Fig. 39 shows the experimental angular distributions of the electrons emitted from $2s^2\ ^1S$ and $2p^2\ ^1D + 2s2p\ ^1P$ autoionizing states. In Fig. 40 is shown a typical electron spectrum observed at 150° for 20 keV He^+ on He. Experimental results for the continuous parts of the electron spectra at detection angles from 30 to 150° are shown in Fig. 41(a). To compare angular distributions more clearly, the ratios $\sigma(E_e, \theta_{lab})/\sigma(E_e, 90°_{lab})$ are plotted in Fig. 41(b).

Absolute cross sections for K-shell ionization by 50- to 600-keV H^+

and He^+ incident on CH_4, N_2 and Ne were measured by Stolterfoht and Schneider[32] (1975). Total cross sections for K-shell ionization were obtained by integrating the Auger spectra with respect to electron energy and emission angle. The measured data are summarized in Table 8. The results for H^+ impact are plotted in Fig. 42.

McKnight and Rains[33] (1976) used Auger-electron spectroscopy to study inner-shell ionization in Ne, N_2, and SF_6 by 1-5 -MeV H^+ and He^+ ions. The electron energy analyzer was a conventional 45° parallel-plate electrostatic analyzer with nominal 0.7% resolution. The subtraction of the continuous electron background was done by fitting an exponential to a region on either side of the Auger peaks. Total ionization cross sections were obtained by integrating the cross section for electron production over the electron energy region of interest. Assuming that the Auger electrons are emitted isotropically in the K-shell processes studied, the differential cross sections obtained at 90° are multiplied by 4π to obtain total electron production cross sections. Because the fluorescence yield is so small for the targets used here, multiple ionization effects which cause the change of the fluorescence yield may be ignored, and the electron production cross section is essentially the K-shell ionization cross section. Their cross sections are given in Table 9 and illustrated in Fig. 43 and Fig. 44. They also showed typical Auger-electron spectra in Fig. 45 and Fig. 46 in order to discuss the multiple ionization effects.

The outer s-shell ionizations of Ne, Ar, and Kr by H_2^+ and He^+ impacts have been studied in the energy range of 100 keV to 1000 keV by Hippler and Schartner[34] (1975). Cross sections for the ionization process (1) have been obtained by measuring light intensities resulting from the decay of the excited ion X^{+*} to its ground state under emission

of light (Eq. (2)).

$$A^+ + X(ns^2np^6\ {}^1S_0) \rightarrow (A^+ + e^-) + X^{+*}(nsnp^6\ {}^2S_{1/2}) \quad (1)$$

$$X^{+*}(nsnp^6\ {}^2S_{1/2}) \rightarrow X^+(ns^2np^5\ {}^2P_{3/2;1/2}) + h\nu. \quad (2)$$

The vacuum ultraviolet monochromator was equipped with a platinum coated grating blazed at 80 nm; the detector was a Valvo channel electron multiplier. The emitted light was observed at an angle of 55° with respect to the ion beam and with the monochromator rotated 45° around its optical axis. Absolute emission cross sections were obtained by comparing the signal rates with those resulting from 400 keV proton impact and using the known proton impact cross sections. Then, absolute cross sections for the outer s-shell ionizations were obtained by multiplying the emission cross section data with appropriate factors obtained from their own relative transition probability measurements. The cross sections are given in Table 10 as functions of the projectile energy E and are plotted in Figs. 47, 48, and 49 in an equal velocity scale.

Rødbro et al.[35] (1979) have measured cross sections for the capture of K-shell electrons (σ_{CK}) from Ne and C (in CH_4) by H^+, He^{2+}, and Li^{3+} projectiles, and of L-shell electrons from Ar by H^+ in an energy range from 0.4 to 3 MeV/amu. The emerging beam was charge analysed while Auger electrons resulting from inner-shell vacancy production in the target were detected with an electrostatic analyzer. An inner-shell capture event was recognized by the coincident detection of an Auger electron and a projectile whose charge state had been reduced by one unit. The ratio of the number of coincidence events to that of singles Auger electrons, after appropriate background corrections, was equal to the ratio of the cross section for single capture from the

shell of interest to that for total vacancy production from that shell. Total Auger-electron yields were obtained from spectra by least-squares-fitting an exponential to the background on either side of the Auger peaks and integrating the remaining area. The cross sections were placed on an absolute scale by setting σ_{VK} (here σ_{VK} is the cross section for total K-vacancy production in the target.) for proton bombardment equal to 8.2×10^{-20} cm^2 and 1.01×10^{-18} cm^2 for 1-MeV protons on neon and 0.5-MeV protons on CH_4, respectively. Their results for σ_{VK} are listed in Tables 11 and 12. The ratio between coincidences R and singles Auger electrons A is equal to σ_{CK}/σ_{VK}. Values of R/A obtained in this experiment are shown in Tables 13 and 14. In all cases they used $\sigma_{CK} = (R/A)\ \sigma_{VK}$. In Figs. 50 and 51 are presented their experimental values for σ_{CK}/Z_1^5 (where Z_1 is projectile nuclear charge). They also showed in Figs. 50 and 51 the Z_1-scaling properties of cross sections for ionization of the target K electron to the continuum σ_i. Experimentally they took this to be the vacancy-production cross section after subtracting the capture contribution, that was, $\sigma_{iK} = \sigma_{VK} - \sigma_{CK}$. In Figs. 52 and 53, they compared the present values of σ_{CK} with the Nikolaev OBK result, divided by 3, and with the results of several more sophisticated calculations.

Target K-shell ionization and K-shell capture cross sections differential in projectile scattering angle have been measured for selected combinations of accelerated ^{1}H, ^{4}He and ^{7}Li ions and gaseous targets of neon and argon in the high energy collision ($\geq$ 1.7 MeV) by Horsdal-Pedersen and Pedersen[36] (1982). The differential K-shell capture and ionization events were identified by scattered-particle, KLL Auger electron coincidence techniques.

Cross sections for single- and double-electron loss (electron

capture plus impact ionization) for H^+, He^{q+}, O^{q+}, and Au^{q+} incident on helium have been measured at velocities from $\sim v_0$ to $\sim 10v_0$ by Hvelplund et al.[37] (1980). Measurements were reported for H^+, He^+, and He^{++} at energies 0.5-5 MeV/amu, for 125- keV/amu O^{q+} (q=1,···,6), 1- MeV/amu O^{q+} (q=3,···,8), 16.8- keV/amu Au^{q+} (q=3,···,17), and 100- keV/amu Au^{q+} (q=5,···,21). The cross sections were measured by a time-of flight spectrometer and put on an absolute scale via condenser-plate measurements where the slow ions were collected. Slow ions produced by the interaction between projectiles and target atoms were collected on the condenser plates by applying a transverse electric field to the target region. This electric field was increased until the collected current reached a saturation value. To estimate the current caused by secondary emission from the surface of the negative plate, a magnetic field was supplied to the target region. Fig. 54 shows their ionization measurements with H^+, He^+, and He^{++} at high velocities. Haugen et al.[38] (1982) also carried out experimental studies of the ionization of helium by fast light ions, to investigate deviations from a q^2 scaling of the ionization cross section by ions of charge q.

Systematic studies were performed for equivelocity H, He, Li, B, C, and O ions, carrying up to a maximum of three to four electrons, at reduced energies of 0.64, 1.44, and 2.31 MeV/amu. Experimental measurements determined the absolute sum of partial-ionization cross sections by the condenser-plate method and the relative contribution of singly and doubly charged ions by time-of-flight spectrometry. Experimental data obtained in this study are shown in Fig. 55. Notable deviation from the q^2 Coulomb scaling at constant velocity is illustrated in Fig. 56 for bare projectiles up to oxygen at the three reduced energies of this study. Also, absolute partial-ionization cross sections were

determined for inelastic interactions involving fully stripped atomic projectiles and noble-gas atoms by Haugen et al.[39] (1982). For helium bombarded with stripped H, He, Li, B, C, and O at reduced energies of 1.44 and 2.3 MeV/amu, the ratio of cross sections for double and single ionization $R = \sigma_{i2}/\sigma_{i1}$ showed a strong dependence on the incident projectile charge.

5. Target Excitation

McKee et al.[40] (1977) used a modulated crossed-beam technique to determine cross sections for the formation of H(2p) and H(2s) atoms in collisions of He^+ with H and H_2 within the energy range 5-26 keV. Cross sections for H(2s) and H(2p) formation for the reactions concerned were determined separately from measurements of the intensity of the Lyman-α radiation emitted from the crossed-beam intersection region both in the presence of and in the absence of an electric field large enough to produce essentially complete quenching of the 2s metastable state. A fast beam of momentum-analysed He^+ ions of the required energy intersected at right-angles a chopped thermal-energy target beam of either H_2 or highly dissociated hydrogen derived from a tungsten tube furnace dissociation source operated at 2600-2700 K. Lyman-α radiation from the beam intersection region was viewed at an angle of 55° with respect to the He^+ beam direction by an open-ended Cu/Be multiplier fitted with a lithium fluoride windowed cell through which pure oxygen gas was passed at atmospheric pressure. Signals from the Lyman-α detector were analysed by a lock-in amplifier whose reference was derived from the target beam chopper. Their measured cross sections $\sigma_{2p}(H_2)$, $\sigma_{2s}(H_2)$, $\sigma_{2p}(H)$ and $\sigma_{2s}(H)$ for formation of H(2p) and H(2s) atoms in $He^+ - H_2$ and $He^+ - H$ collisions are presented in Table 15. In Fig. 57 their measured cross sections for H(2p) and H(2s) formation in $He^+ - H_2$ collisions are compared with the results of Andreev et al.[41] (1967), van Zyl et al.[42] (1967), and Young et al.[43] (1968). Fig. 58 shows their measured cross sections $\sigma_{2p}(H)$ and $\sigma_{2s}(H)$ for H(2p) and H(2s) formation in $He^+ - H$ collisions.

The excitation of the $1s_2$- and $1s_4$-levels (Paschen's notation) of neon and argon by He^+-impact was studied in the energy range of 100 keV

to 1000 keV by Beyer et al.[44] (1976). The light intensities resulting from the decay of the excited target atoms were measured. The corresponding wavelengths lie in the vacuum ultraviolet region (VUV) (73.6/74.4 nm and 104.8/106.7 nm for neon and argon respectively). The apparatus essentially consisted of the target chamber and the optical device consisting of the VUV monochromator and the channel electron multiplier. The VUV monochromator was mounted at 55° with respect to the ion beam and rotated 45° around its optical axis. Absolute emission cross sections for the $1s_2$- and $1s_4$-level in neon and argon were obtained by comparing the signal rates resulting from the 400 keV He^+- and 400 keV H^+-impact respectively using the data of Hippler and Schartner[45] (1974). In Fig. 59, their emission cross section results for the He^+ impact excitation of the $1s_2$- and $1s_4$-levels in neon are compared with the theoretical H^+ impact data of Albat and Gruen[46] (1975), with the experimental H^+ impact results of Hippler and Schartner[45] (1974) and with the H^+- and He^+-impact data of York et al.[47] (1972). In Fig. 60, the He^+ impact data for the excitation of the argon resonance levels are shown together with results of proton impact[45] and the four state calculations of Albat et al.[48] (1975).

Hippler et al.[49] (1978) also presented new data on the direct (1) and charge-exchange (2) excitation of the 2^1P level in He^+-He collisions up to impact energies of 1 MeV.

$$He^+ + He \rightarrow \begin{cases} He^+ + He(2^1P) & (1) \\ He(2^1P) + He^+. & (2) \end{cases}$$

Both processes were detected by measuring light intensities resulting from the decay of the excited $He(2^1P)$ to the He ground state. The wavelength of the corresponding transition lies in the vacuum ultraviolet (VUV) at 58.4 nm. Separation between the target (1) and the

projectile (2) excitation was made by use of the Doppler shift. In Fig. 61, the cross sections for the direct and the charge-exchange excitation, respectively, are given as a function of the impact energy.

He atoms excited to the $1s3d\,^1D$ and $1s4d\,^1D$ levels were produced by collisions of 10-40 keV He^+ ions with He atoms and the splitting of the magnetic depolarization signals of the impact radiation in electric fields was investigated by Müller et al.[50] (1982). The impact radiation emitted by both the thermal He atoms produced by direct excitation and the high-velocity He atoms produced by charge transfer was observed with a photomultiplier from a direction perpendicular to the ion beam. The desired wavelength was selected by interference filters. External electric and magnetic fields E_z and B_z were applied to the collision region and were directed perpendicular to the ion beam and to the direction of observation. Using excitation cross sections and polarization fractions measured by de Heer and van den Bos[51] (1965) and by Wolterbeek Muller and de Heer[52] (1970), the excitation cross sections of the Zeeman sublevels of the $4\,^1D$ levels were evaluated. The results shown in Fig. 62 are based on the values published by Thomas[53] (1972). They finally evaluated the excitation cross sections $\sigma_{|m|}$ of the Zeeman sublevels of the $4\,^1D_2$ level shown in Fig. 63.

Kadota et al.[54] (1982) measured emission cross sections for the $2p \rightarrow 2s$ resonance line and the $3p \rightarrow 2p$ line of Lithium produced by He^{2+} ion impact in the energy region of 15-600 keV. For the 2p level the corresponding excitation cross sections were evaluated. The Li beam was crossed perpendicular by the He^{2+} ion beam and the emission was observed perpendicular to the plane of the He^{2+} and Li beam by means of the Leiss monochromator. The emission cross section for $2p \rightarrow 2s$ by He^{2+} on Li was brought on an absolute scale by comparing the photon flux with that in

the case of 500 eV electrons on Li and taking the emission cross section of Leep and Gallagher[55] (1974), considering polarization effects. The measured resonance emission cross sections (2p → 2s) are shown together with those of Barrett and Leventhal[56] (1981) in Fig. 64 and are given in Table 16. The emission cross sections for 3d → 2p are also shown in Fig. 64 and Table 16. In order to study the high-energy behaviour of the experimental data, the quantities $\sigma_{ex}(2p)\ T/Z^2$ and $\sigma_{em}(3d \to 2p)\ T/Z^2$ are plotted against T in Figs. 65 and 66 both for He^{2+} and e^- impact.

Aldag et al.[57] (1981) determined differential cross sections for 15-100 keV He^+ excitation of atomic hydrogen to its n=2 level for c.m. angles for 0 to 8 mrad. The differential cross sections were obtained from an analysis of the angular distribution of the scattered ions which had lost an energy corresponding to the excitation of the target to its n=2 level. The measurements of the scattered ions were made on the angular energy-loss spectrometer. The energy full widths at half maximum of the peaks in the energy loss spectra were about 1.2 eV in this experiment. Table 17 gives the angular differential cross sections for the process $He^+ + H \to He^+(\theta) + H^*(n=2)$ at various projectile laboratory incident energies measured by them. The experimentally determined differential cross sections for 25 and 100 keV are shown in Figs. 67 and 68. Total cross sections were given for the same process in the 15-200 keV range. The total cross sections were obtained by integrating the differential cross sections $d\sigma/d\Omega$. Fig. 69 shows the total cross sections, σ, determined from the 15-100 keV angular measurements. Also shown for 15-200 keV are apparent total cross sections, σ, determined by integration of $d\sigma/d\Omega$, the averaged apparent differential cross section. The apparent differential cross sections are given in Table 18.

6. Target Ionization with Excitation

Emission spectra in the 2850-4300-Å region produced by 0.7- to 10-keV impact of H^+, H^0, and He^+ on CO_2 and N_2O were observed by Moore[58] (1975). The emission consisted almost exclusively of the A-X and B-X systems of CO_2^+ and the A-X system of N_2O^+. There were no emissions from excited fragments of the parent molecules. The emission cross sections for impact of H^+ and H^0 were given but those for He^+ impact were not shown in his paper.

Wehrenberg[59] (1977) reported cross sections for emission of 3914-Å radiation from collisions of H^+ and He^+ projectiles with N_2 target molecules. The 3914-A photons were emitted in the decay of the $B^2\Sigma_u^+$ state of N_2^+ to the $X^2\Sigma_g^+$ ground state, the vibrational quantum number being zero for both excited and ground state. The energy range of the projectiles in these experiments was from 0.5 to 34.0 keV. Any excited-state population of He^+ was completely removed as the ion beam passed through the 0.4-cm source-extractor gap because of Stark mixing of the 2s and 2p states. Photon collection, selection, and detection were done by a lens-mirror system, an interference filter, and a photomultiplier (EMI 6256SA) used in a photon-counting system. The optical elements observing the collision region intercepted a total of 1.38 sr of the emitting solid angle. The transmission of the interference filter was maximum at 3914-Å and the full width at half maximum was 22-Å. The measured cross sections as a function of incident particle energy are presented in Fig. 70.

7. Dissociation and Dissociative Ionization

There are no data on simple dissociation cross section. Data on dissociative ionization cross section are only results for the experiment in the He^{++} ion-hydrogen molecular collision done by Afrosimov et al.[22] and Shah and Gilbody[24], using the coincidence method. These results are already given in Sec. 4. Relative data on dissociative ionization were obtained from the ionized fragment yield by Edward et al.[60-64] These data are simply reported in this section. By measuring the energy and time-of-flight of fragment ions from molecular breakup, the fragments can be separated according to their mass to charge ratios and the kinetic-energy spectra for each recorded. Edwards et al.[60] applied this technique to the dissociative ionization of N_2 caused by 1-MeV H^+ and He^+ projectiles. The N^+ spectra produced by both H^+ and He^+ are shown in Fig. 71. For the He^+ beam a long high-energy tail is observed in the N^+ spectrum and is shown in Fig. 72. The N^{++} spectra produced by H^+ and He^+ are shown in Fig. 73. The N^{3+} spectrum produced by He^+ is also shown in Fig. 74. Kinetic-energy spectra of the O^+, O^{2+}, and O^{3+} fragments produced by 1-MeV H^+, He^+, and O^+ projectiles were measured by Steuer et al.[61] The apparatus and the time-energy spectroscopy technique used in this experiment were described in reference 60. The energy spectra of O^+, O^{2+}, and O^{3+} fragments were obtained from the energy, time-of-flight two-parameter array with the use of a computer-assisted background-subtraction technique. The results are shown in Figs. 75-77.

Methane was bombarded by 1 MeV H^+, He^+, and O^+ projectiles. Kinetic-energy spectra were presented for fragment ions with integer mass-to-charge ratios of 1, 2, 3, 4, 6, and 12 by Edwards et al.[62] The time-energy-spectroscopy technique was described in reference 60. The

kinetic-energy spectra of the H^+ and H_2^+ fragments are shown in Figs. 78 and 79, respectively, and the kinetic-energy spectra of the C^{q+} fragments produced by O^+ projectiles are shown in Fig. 80.

Wood et al.[63] reported studies of the dissociative ionization of CO and NO induced by 1-MeV H^+, He^+ and O^+ projectiles. The time-energy spectroscopy (TES) technique was used to identify the dissociation fragments according to their mass-to-charge (m/q) ratios, and to record kinetic energy spectra for fragment species. The kinetic energy spectra of the fragments observed in the dissociation of CO are shown in Figs. 81-84. In order to facilitate the visual presentation, the spectra were normalized to approximately the same height in the figures. The full scale values of yields per unit charge and pressure are given in the figure captions. The kinetic energy spectra of the 1+, 2+, and 3+ fragments observed in the dissociation of NO are shown in Figs. 85-88. The full scale values of yields per unit charge and pressure are given in relative units in the figure captions. N_2O was bombarded with 1 MeV H^+, He^+, and O^+ projectiles. The dissociation fragments observed were N^+, O^+, NO^+, N_2^+, N^{2+}, and O^{2+}. Kinetic energy spectra of singly ionized fragments obtained using a time-energy spectroscopy (TES) technique were reported by Shah et al.[64] The kinetic energy spectra of the fragments observed in the dissociation of N_2O are shown in Figs. 89-92. Each spectrum was normalized to approximately the same height.

8. Conclusion

The experimental data on cross sections for the 5 keV - 3.5 MeV He^{+} and He^{++} impacts on gas targets with a single collision condition have been surveyed in the literatures from 1975 to the end of 1982. The experimental data on solid (foil) targets and the theoretical calculated values of the cross sections have not been here investigated. It will be necessary to compile the data on these fields in the near future. Further, with respect to the gas data, the cross section measurement for the dissociation process is very scarce. We also intend to investigate the data on the same collision systems as reported here in the collision energy less than 5 keV following this report. Finally, it should be noted that the JAERI-M of Nakai et al.[65] and Sataka et al.[66] complement the contents of this report.

REFERENCES

1. Y. Nakai and N. Oda
"Atomic and Molecular Processes for Fusion Research", (in Japanese)
Genshiryoku Gakkaishi 22, 3 (1980)

2. S. K. Allison, J. Cuevas and P. G. Murphy
Phys. Rev. 102, 1041 (1956)

3. P. R. Jones, F. P. Ziemba, H. A. Moses and E. Everhart
Phys. Rev. 113, 182 (1959)

4. L. I. Pivovar, V. Ma Tubaev and M. T. Novikov
Sov. Phys. JETP 15, 1035 (1962)

5. M. B. Shah, T. V. Goffe and H. B. Gilbody
J. Phys. B 10, L723 (1977)

6. I. S. Dmitriev, V. S. Nikolaev, L. N. Fateeva, and Ya. N. Teplova
Zh. Eksp. Teor. Fiz. 42, 16 (1962) (Sov. Phys. JETP 15, 11 (1962))

7. J. P. Keene
Phil. Mag. 40, 369 (1949)

8. N. V. Fedorenko, V. V. Afrosimov and D. M. Kaminker
Sov. Phys. Tech. Phys. 1, 1861 (1956)

9. H. B. Gilbody and J. B. Hasted
Proc. Roy. Soc. 240A, 382 (1957)

10. F. J. de Heer, W. Huizenga and J. Kistemaker
Physica 23, 181 (1957)

11. H. B. Gilbody, J. B. Hasted, J. V. Ireland, A. R. Lee, E. W. Thomas and A. S. Whiteman
Proc. Roy. Soc. 274A, 40 (1963)

12. F. J. de Heer, J. Schutten and H. Monstafa
Physica 32, 1793 (1966)

13. L. I. Pivovar, Yu. Z. Levchenko and A. N. Grigorev
Sov. Phys. JETP 27, 699 (1968)

14. R. A. Langley, D. W. Martin, D. S. Harmer, J. W. Hooper and E. W. McDaniel
Phys. Rev. 136, A379 (1964)

15. L. J. Puckett, G. O. Taylor and D. W. Martin
Phys. Rev. 178, 271 (1969)

16. N. V. Fedorenko and V. V. Afrosimov
Sov. Phys. Tech. Phys. 1, 1872 (1956)

17. E. S. Solov'ev, R. N. Il'in, V. A. Oparin and N. V. Fedorenko
Sov. Phys. JETP 18, 342 (1964)

18. P. S. Rudolph and Charles E. Melton
J. Chem. Phys. 45, 2227 (1966)

19. Z. Z. Latypov, I. P. Flaks and A. A. Shaporenko
Sov. Phys. JETP 30, 29 (1970)

20. B. G. O'Hare, R. W. McCullough and H. B. Gilbody
J. Phys. B 8, 2968 (1975)

21. V. V. Afrosimov, G. A. Leiko, Yu. A. Mamaev and M. N. Panov
Sov. Phys. JETP 40, 661 (1975)

22. V. V. Afrosimov, G. A. Leiko and M. N. Panov
Sov. Phys. Tech. Phys. 25, 313 (1980)

23. M. B. Shah and H. B. Gilbody
J. Phys. B 14, 2361 (1981)

24. M. B. Shah and H. B. Gilbody
J. Phys. B 15, 3441 (1982)

25. L. H. Toburen and W. E. Wilson
Phys. Rev. A 19, 2214 (1979)

26. M. Sataka, J. Urakawa and N. Oda

J. Phys. B 12, L729 (1979)

27. L. H. Toburen, W. E. Wilson and R. J. Popowich

Radiat. Res. 82, 27 (1980)

28. Steven T. Manson and L. H. Toburen

Phys. Rev. Lett. 46, 529 (1981)

29. L. H. Toburen, P. Ziem, N. Stolterfoht, D. Schneider and M. Prost

IEEE Tran. Nucl. Sci, NS-28, 1131 (1981)

30. A. Bordenave-Montesquieu, A. Gleizes and P. Benoit-Cattin

Phys. Rev. A 25, 245 (1982)

31. N. Tokoro, S. Takenouchi, J. Urakawa and N. Oda

J. Phys. B 15, 3737 (1982)

32. N. Stolterfoht and D. Schneider

Phys. Rev. A 11, 721 (1975)

33. R. H. McKnight and R. G. Rains

Phys. Rev. A 14, 1388 (1976)

34. R. Hippler and K. H. Schartner

Z. Phys. A 273, 123 (1975)

35. M. Rødbro, E. Horsdal Pedersen and C. L. Cocke

Phys. Rev. A 19, 1936 (1979)

36. Erik Horsdal-Pedersen and Nils-Henrik Pedersen

J. Phys. B 15, 2205 (1982)

37. P. Hvelplund, H. K. Haugen and H. Kundsen

Phys. Rev. A 22, 1930 (1980)

38. H. K. Haugen, L. H. Andersen, P. Hvelplund and H. Knudsen

Phys. Rev. A 26, 1950 (1982)

39. H. K. Haugen, L. H. Andersen, P. Hvelplund and H. Knudsen

Phys. Rev. A 26, 1962 (1982)

40. J. U. A. McKee, J. R. Sherdan, J. Geddes and H. B. Gilbody
J. Phys. B 10, 1679 (1977)

41. E. P. Andreev, V. A. Ankudinov and S. V. Bobashev
Sov. Phys. JETP 23, 375 (1966)
1967 Proc. 5th Int. Conf. on Physics of Electronic and Atomic Collisions, Leningrad (Leningrad: Nauka) pp309-11

42. B. van Zyl, D. Jaecks, D. Pretzer and R. Geballe
Phys. Rev. 158, 29 (1967)

43. R. A. Young, R. F. Stebbings and J. W. McGowan
Phys. Rev. 171, 85 (1968)

44. H. F. Beyer, R. Hippler and K. H. Schartner
Z. Phys. A 279, 345 (1976)

45. R. Hippler and K. H. Schartner
Z. Phys. A 270, 225 (1974)

46. R. Albat and N. Gruen
J. Phys. B 8, 959 (1975)

47. G. W. York, Jr, J. T. Park, V. Pol and D. H. Crandall
Phys. Rev. A 6, 1497 (1972)

48. R. Albat, N. Gruen and B. Wirsam
J. Phys. B 8, L82 (1975)

49. R. Hippler, K. H. Schartner and H. F. Beyer
J. Phys. B 11, L337 (1978)

50. R. Muller, G. von Oppen, W. D. Perschmann and W. Schilling
J. Phys. B 15, 3179 (1982)

51. F. J. de Heer and J. van den Bos
Physica 31, 365 (1965)

52. L. Wolterbeek Muller and F. J. de Heer
Physica 48, 345 (1970)

53. E. W. Thomas
Excitation in Heavy Particle Collisions (New York: Wiley-Interscience) (1972)

54. K. Kadota, D. Dijkkamp, R. L. van der Wonde, Pan Guang Yan and F. J. de Heer
J. Phys. B 15, 3297 (1982)

55. D. Leep and A. Gallagher
Phys. Rev. A 10, 1082 (1974)

56. J. L. Barrett and J. J. Leventhal
Phys. Rev. A 23, 485 (1981)

57. J. E. Aldag, J. L. Peacher, P. J. Martin, V. Sutcliffe, J. George, E. Redd, T. J. Kvale, D. M. Blankenchip and J. T. Park
Phys. Rev. A 23, 1062 (1981)

58. John H. Moore, Jr.
J. Geophysical Res. 80, 3727 (1975)

59. Paul J. Wehrenberg
Phys. Rev. A 15, 843 (1977)

60. A. K. Edwards, R. M. Wood and M. F. Steuer
Phys. Rev. A 15, 48 (1977)

61. M. F. Steuer, R. M. Wood and A. K. Edwards
Phys. Rev. A 16, 1873 (1977)

62. A. K. Edwards, J. E. Graves, R. M. Wood and M. F. Steuer
J. Chem. Phys. 69, 1985 (1978)

63. R. M. Wood, M. F. Steuer and A. K. Edwards
J. Chem. Phys. 69, 4487 (1978)

64. A. V. Shah, M. N. Monce, A. K. Edwords, M. F. Steuer and R. M. Wood
J. Chem. Phys. 73, 6174 (1980)

65. Y. Nakai, M. Sataka and T. Shirai
"Data on Collisions of Helium Atoms and Ions with Atoms and Molecules I.", (in Japanese) JAERI-M 8849 (1980)

66. M. Sataka, T. Shirai, A. Kikuchi and Y. Nakai
"Ionization Cross Sections for Ion-Atom and Ion-Molecule Collisions, I." JAERI-M 9310 (1981)

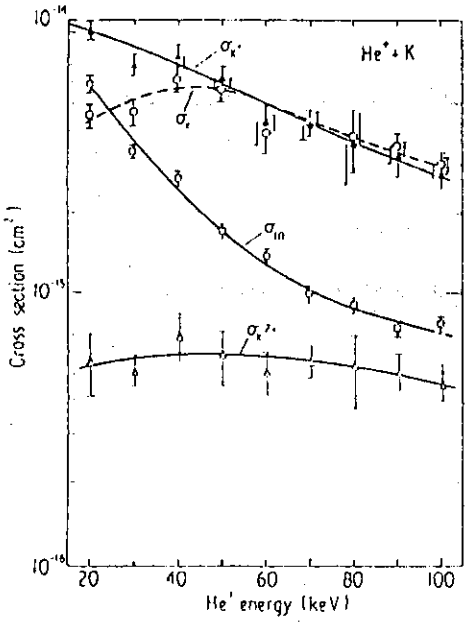

Energy dependence of measured cross sections σ_e for electron production, σ_{K^+} and $\sigma_{K^{2+}}$ for K^+ and K^{2+} production and σ_{10} for one-electron capture by He^+ ions in potassium vapour.

FIG.1

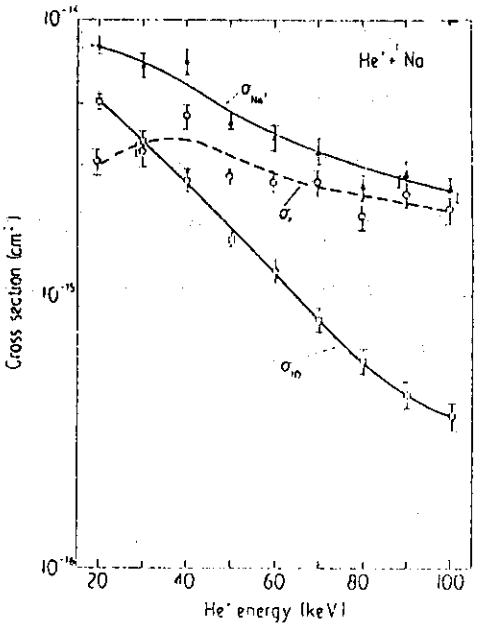

Energy dependence of measured cross sections σ_e for electron production, σ_{Na^+} for Na^+ production and σ_{10} for one-electron capture by He^+ ions in sodium vapour.

FIG.2

TABLE 1

Elementary processes with change of the charge states of colliding particles in the He^{2+} - He interaction.

№	Scheme of process	Name of process	Designation of process
1	$\overrightarrow{He^0} + He^{2+}$	Two-electron charge exchange	2002
2	$\overrightarrow{He^+} + He^+$	One-electron charge exchange	2011
3	$\overrightarrow{He^{2+}} + He \rightarrow \overrightarrow{He^{+3}} + He^{2+} + 2e$	Ionization with removal of two electrons	2022
4	$\overrightarrow{He^{2+}} + He^+ + e$	Ionization with removal of one electron	2021
5	$\overrightarrow{He^+} + He^{2+} + e$	Capture with ionization	2012

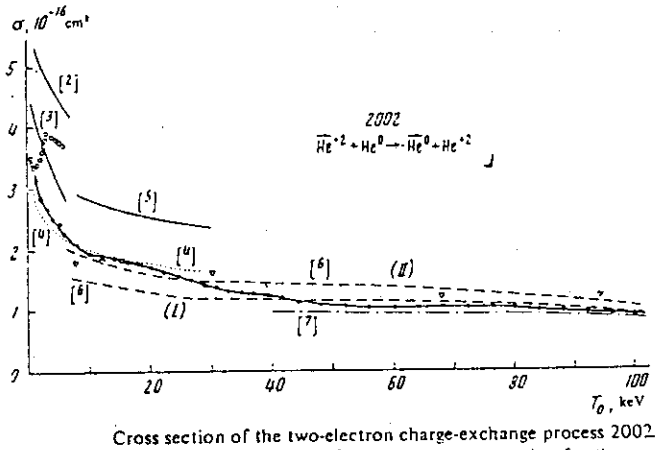

Cross section of the two-electron charge-exchange process 2002. Experiment: • – present paper, Δ – [8], O – total cross section for the production of slow He^{2+} ions from [19]. The theoretical cross sections of two-electron charge-exchange are designated by in the square brackets by the number of the corresponding reference.

FIG.3

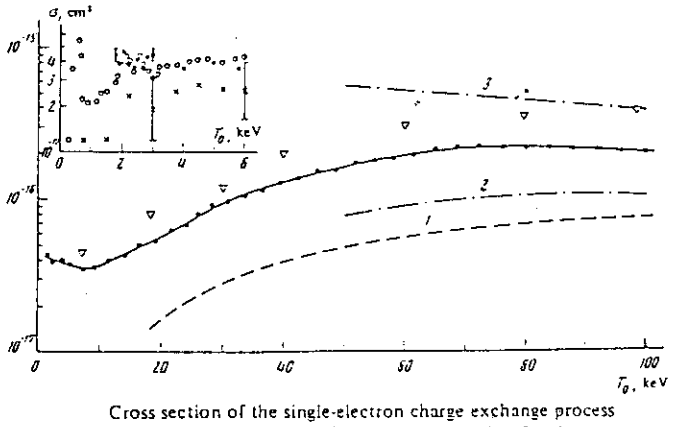

Cross section of the single-electron charge exchange process 2011. Experiment: • – present work, Δ – total cross section for the production of fast He ions from [8]. The insert shows a comparison of the present results (•) for the 2011 process with the cross sections for the production of slow He^+ ions at low energies from [9] (O) and [11] (×). Theory: 1 and 2 – charge exchange to the ground state from [6] and [7], respectively, 3 – charge exchange to the ground state and excited 2s and 2p states, from [7].

FIG.4

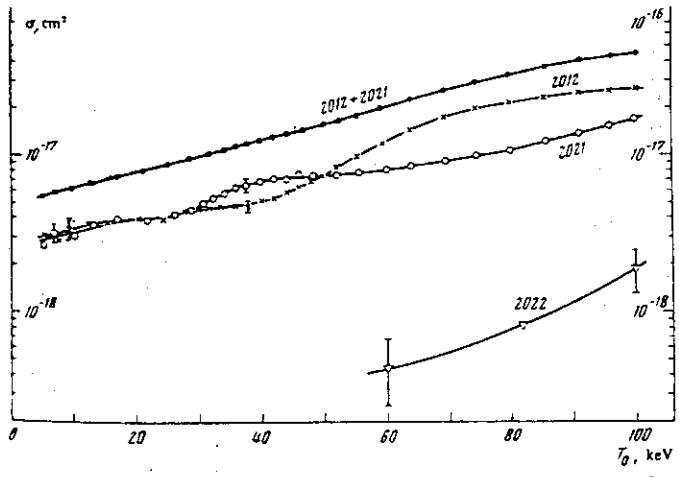

Cross section of the processes of ionization with removal of two electrons (2022), ionization with removal of one electron (2021), capture of one electron with ionization (2012), and the resultant cross section of the processes 2021 + 2012.

FIG.5

TABLE 2

Reaction	Number	Final state of target	Energy of slow ions, eV	Name	Notation
$He^{+2} + H_2 \rightarrow He^{+2} + H_2^+ + e^-$	1	$1s\sigma_g$	0	Pure ionization	$c_0^{20}H_2^+$
$He^{+2} + H_2 \rightarrow He^{+2} + H^+ + H^0 + e^-$	2a 2b	$1s\sigma_g$ $2p\sigma_u$	0 7	Dissociative ionization	$c_0^{22}H^+H^0$
$He^{+2} + H_2 \rightarrow He^{+2} + H^+ + H^+ + 2e^-$	3	$(H^+ + H^+)$	9	Double ionization	$c_0^{22}2H^+$
$He^{+2} + H_2 \rightarrow He^{+1} + H_2^+$	4	$1s\sigma_g$	0	Pure capture (charge exchange)	$c_0^{21}H_2^+$
$He^{+2} + H_2 \rightarrow He^{+1} + H^+ + H^0$	5a 5b	$1s\sigma_g$ $2p\sigma_u$	0 7	Dissociative capture	$c_0^{21}H^+H^0$
$He^{+2} + H_2 \rightarrow He^{+1} + H^+ + H^+ + e^-$	6	$(H^+ + H^+)$	9	Capture with ionization	$c_0^{21}2H^+$
$He^{+2} + H_2 \rightarrow He^0 + H^+ + H^+$	7	$(H^+ + H^+)$	9	Double capture	$c_0^{20}2H^+$

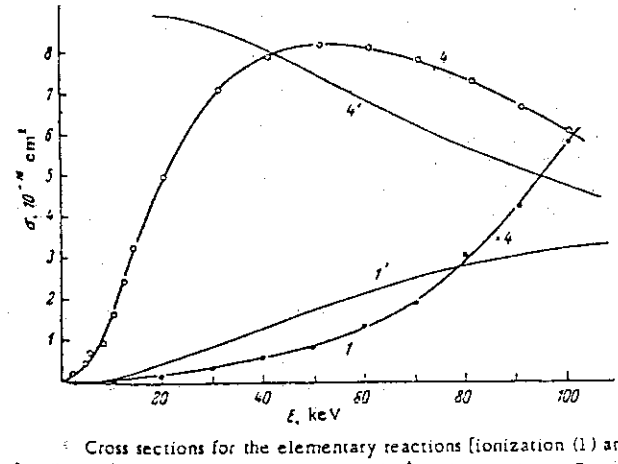

Cross sections for the elementary reactions [ionization (1) and capture (4)] accompanied by the formation of H_2^+ molecular ions. Curves 1' and 4' are the ionization and capture cross sections for the $H^+ - H_2$ pair.

FIG.6

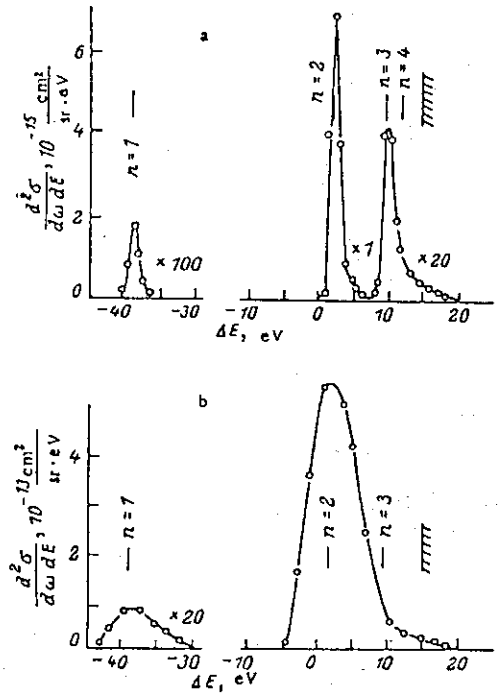

Distribution of the kinetic energies of the fast He^+ ions formed in the single-electron capture (reaction 4). Here ΔE is the change in the kinetic energy of the fast ion. a) E = 5.4; b) 30 keV. The values of ΔE corresponding to the formation of He^+ ions in states with different principal quantum numbers are shown by the vertical lines.

FIG.7

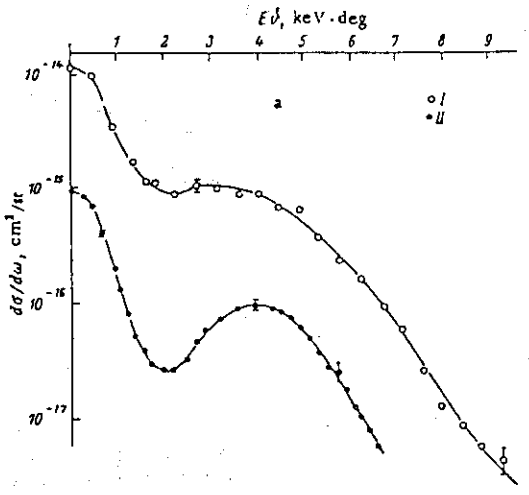

Differential cross sections for the scattering of He^+ ions in reaction 4. I) E = 5.4; II) 2.15 keV.

FIG.8

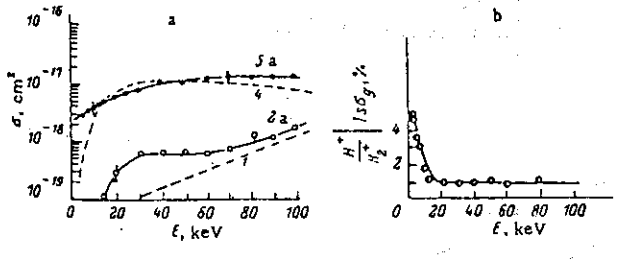

a: Cross sections for capture with dissociation from the $1s\sigma_g$ state of the H_2^+ ion (reaction 5a) and of ionization with dissociation (reaction 2a) from the same state. Dashed curves 4 and 1 show the capture and ionization cross sections, multiplied by 0.01. b: Probability for dissociation of the $H_2^+(1s\sigma_g)$ ion in the course of capture.

FIG.9

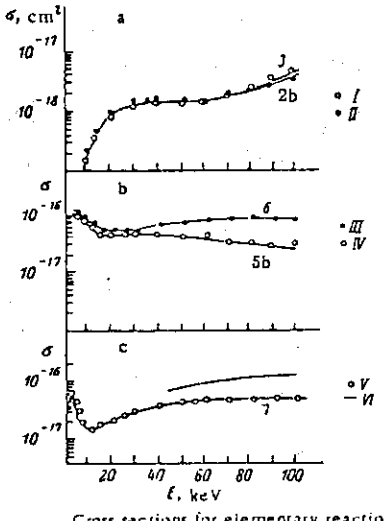

Cross sections for elementary reactions involving the formation of protons, H^+. a: I) Double ionization, $\sigma^{22}_{02}{}_{H^+}$ (reaction 3); II) ionization with dissociation from $2p\sigma_u\sigma^{22}_{0}{}_{H+H^0}$ (reaction 2b). b: III) cross section for capture with ionzation, $\sigma^{21}_{0}{}_{H+H^0}$ (reaction 6); IV) cross section for capture with dissociation from the $2p\sigma_u\sigma^{21}_{0}{}_{H+H^0}$ state, (reaction 5b). c: V) cross section for double capture, $\sigma^{20}_{0}{}_{2H^+}$ (reaction 7); VI) cross section for double capture from Ref. 2.

FIG.10

TABLE 3

Ionisation cross sections for the processes $H^+ + H(1s) \rightarrow H^+ + H^+ + e$ and $He^{2+} + H(1s) \rightarrow He^{2+} + H^+ + e$.

Energy (keV)	$\sigma(H^+)$ (10^{-17} cm^2)	$\sigma(He^{2+})$ (10^{-16} cm^2)
38	13.69±0.64	—
45	13.99±0.49	—
54	14.04±0.56	—
67	13.42±0.43	—
80	12.80±0.45	—
100	11.16±0.33	—
120	10.09±0.32	—
125	—	2.32±0.06
140	8.98±0.27	—
150	—	3.13±0.10
160	8.27±0.26	—
175	—	3.60±0.09
180	7.60±0.25	—
200	7.07±0.21	3.89±0.10
230	6.25±0.21	—
250	—	4.31±0.12
260	5.80±0.19	—
300	5.31±0.16	4.14±0.12
350	4.61±0.14	—
400	4.10±0.10	3.80±0.12
450	3.68±0.13	—
500	3.38±0.12	3.41±0.11
550	3.19±0.10	—
600	3.04±0.12	3.05±0.09
700	2.64±0.11	2.78±0.08
800	2.38±0.07	2.53±0.07
900	2.18±0.07	—
1000	1.97±0.06	2.16±0.06
1150	1.75±0.07	—
1200	—	1.89±0.08
1300	1.58±0.07	—
1400	—	1.70±0.07
1500	1.39±0.06	—
1600	—	1.55±0.04
1900	—	1.35±0.04
2200	—	1.18±0.04

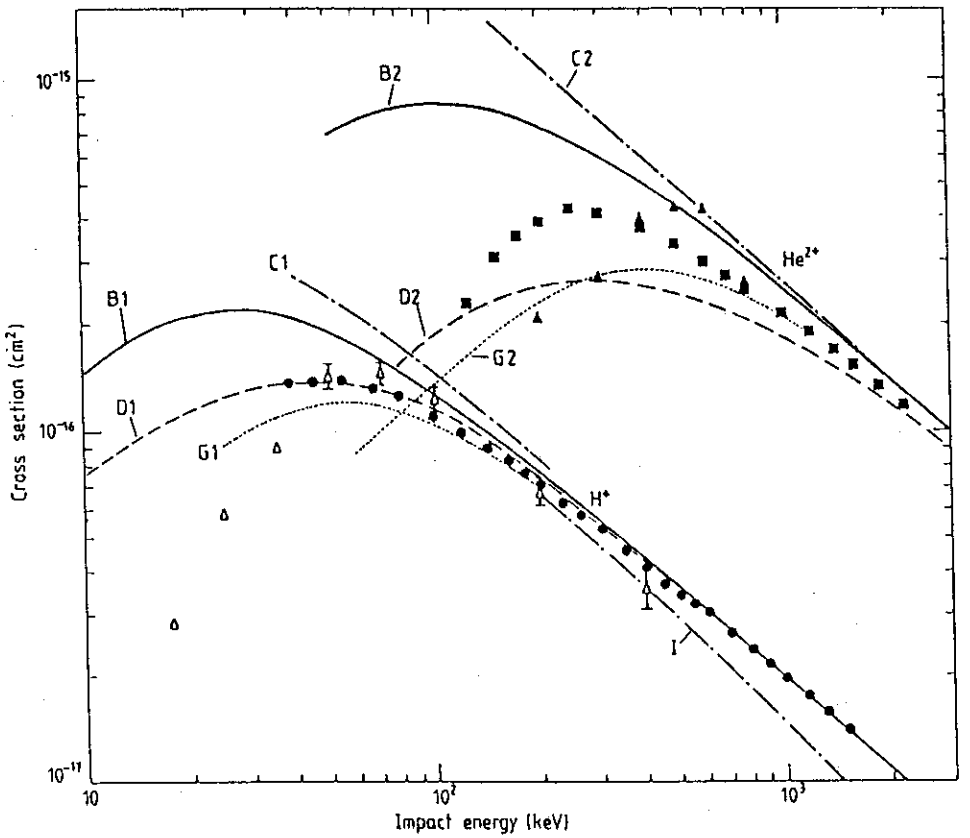

Cross sections $\sigma(H^+)$ and $\sigma(He^{2+})$ for H^+ and He^{2+} impact ionisation of atomic hydrogen. H^+ impact: ●, present results: curve B1, Born approximation (Bates and Griffing 1953); curve C1, CDW approximation (Belkić 1978); curve G1, Glauber approximation (Golden and McGuire 1975); curve I, Classical impulse approximation (Bates and Kingston 1970); curve D1, dipole close-coupling approximation (Janev and Presnyakov 1980); △, CTMC method (Banks *et al* 1976). He^{2+} impact: ■, present results; curve B2, Born approximation (Bates and Griffing 1953); curve C2, CDW approximation (Belkić 1980); curve G2, Glauber approximation (Golden and McGuire 1976); curve D2, dipole close-coupling approximation (Janev and Presnyakov 1980); ▲ CTMC method (Olson and Salop 1977).

FIG.11

TABLE 4

The cross sections σ_{ni} and σ_{di} for non-dissociative and dissociative ionisation, respectively, of H_2 by H^+ and He^{2+} ions.

Energy (keV)	H^+		He^{2+}	
	$\sigma_{ni}(10^{-17}\,cm^2)$	$\sigma_{di}(10^{-17}\,cm^2)$	$\sigma_{ni}(10^{-16}\,cm^2)$	$\sigma_{di}(10^{-16}\,cm^2)$
38.3	18.4±0.9	2.95±0.21	—	—
45	19.8±0.8	2.67±0.15	—	—
54	21.6±1.0	2.47±0.13	—	—
67	21.5±0.7	2.07±0.11	—	—
80	21.3±0.9	1.78±0.11	—	—
100	20.2±0.7	1.46±0.08	—	—
120	18.4±0.6	1.10±0.07	—	—
125	—	—	2.06±0.07	1.33±0.09
140	17.2±0.6	1.05±0.05	—	—
150	—	—	2.94±0.11	1.38±0.09
160	15.9±0.6	0.83±0.04	—	—
175	—	—	3.67±0.11	1.41±0.08
180	14.5±0.6	0.68±0.04	—	—
200	13.3±0.5	0.62±0.04	4.23±0.13	1.38±0.09
230	12.4±0.5	0.58±0.03	—	—
250	—	—	4.85±0.16	1.36±0.11
260	11.4±0.5	0.58±0.03	—	—
300	10.3±0.4	0.445±0.028	5.15±0.17	1.30±0.09
350	9.3±0.4	0.368±0.027	—	—
400	8.5±0.3	0.322±0.018	5.21±0.19	1.06±0.07
450	7.8±0.3	0.300±0.018	—	—
500	7.28±0.29	0.272±0.020	5.07±0.20	0.89±0.07
550	6.64±0.27	0.280±0.021	—	—
600	6.02±0.28	0.231±0.020	4.79±0.17	0.77±0.05
700	5.38±0.28	0.197±0.015	4.61±0.16	0.652±0.040
800	4.85±0.20	0.181±0.013	4.24±0.13	0.552±0.033
900	4.36±0.19	0.152±0.009	—	—
1000	4.00±0.17	0.154±0.012	3.92±0.13	0.435±0.028
1150	3.77±0.20	0.133±0.011	—	—
1200	—	—	3.64±0.16	0.343±0.025
1300	3.37±0.17	0.127±0.009	—	—
1400	—	—	3.26±0.15	0.266±0.019
1500	3.00±0.16	—	—	—
1600	—	—	3.01±0.09	0.238±0.015
1900	—	—	2.78±0.09	0.202±0.013
2200	—	—	2.55±0.09	0.153±0.011

TABLE 5

Transfer ionisation cross sections σ_{ti} in units of $10^{-17}\,cm^2$

Energy (keV)	H^+	Energy (keV)	He^{2+}
37.5	1.28±0.17	160	10.22±0.12
50	0.80±0.03	200	8.92±0.20
70	0.325±0.036	300	4.62±0.06
85	0.171±0.022	450	1.74±0.10
100	0.107±0.012	700	0.402±0.018
150	0.029±0.009	1000	0.120±0.026

Energy (keV)	C^{2+}	C^{3+}	C^{4+}
190	7.80±0.10	—	—
240	10.44±0.20	25.6±0.6	—
300	12.78±0.24	28.4±0.8	—
450	12.08±0.22	25.4±0.4	—
600	10.32±0.28	22.5±0.3	34.0±1.2
1000	4.86±0.12	13.4±0.3	25.3±1.1
1900	0.84±0.02	2.78±0.15	6.64±0.16

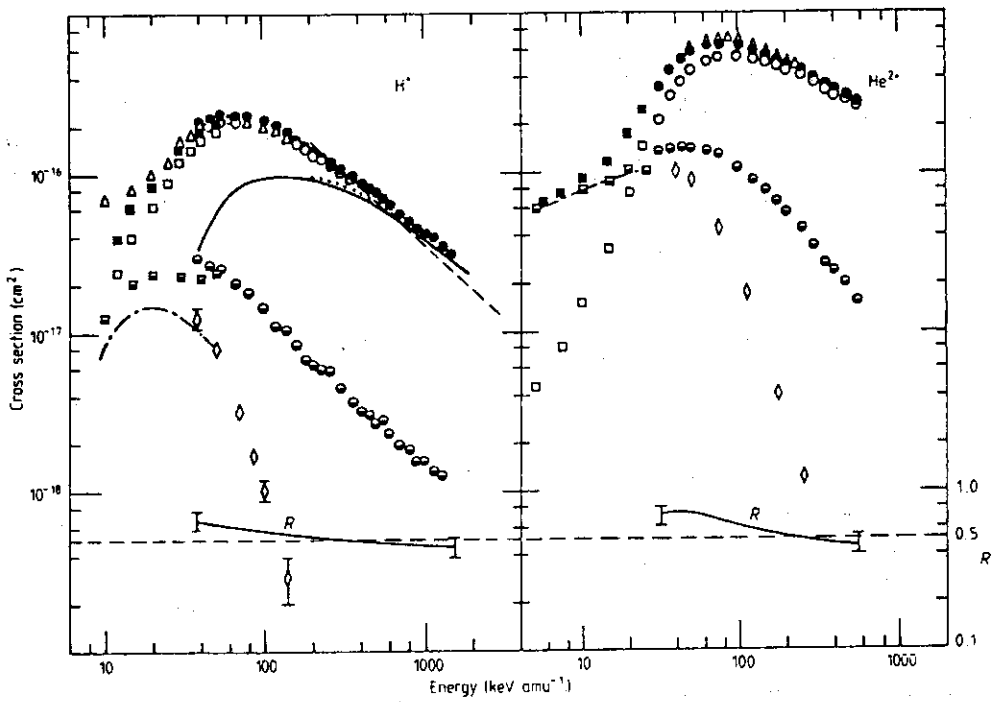

Cross sections σ_{ni} for non-dissociative ionisation, σ_{di} for dissociative ionisation and σ_{ti} for transfer ionisation, together with total cross sections $\sigma_i = (\sigma_{ni} + \sigma_{di})$ for H^+ and He^{2+} ions in H_2. The ratio $R = \sigma_i(H)/\sigma_i(H_2)$ is also shown. Present results: ○, σ_{ni}; ◒, σ_{di}; ◇, σ_{ti}. Results of Afrosimov *et al* (1969) for H^+ and Afrosimov *et al* (1980) for He^{2+}: □, σ_{ni}; ⬓, σ_{di}; − · −, σ_{ti}. Present results: ●, σ_i. Results of de Heer *et al* (1966) for H^+ and Puckett *et al* (1969) for He^{2+}: △, σ_i. Results of Afrosimov *et al* (1969) for H^+ and Afrosimov *et al* (1980) for He^{2+}: ■, σ_i. Results of Hooper *et al* (1961) in energy range 0.15–1.1 MeV and Pivovar and Levchenko (1967) in the range 1–3 MeV: − − −, σ_i. Results of equivelocity electron impact, Rapp and Englander-Golden (1965): ——, σ_i. Results of equivelocity electron impact, Cowling and Fletcher (1973): · · · ·, σ_i.

FIG.12

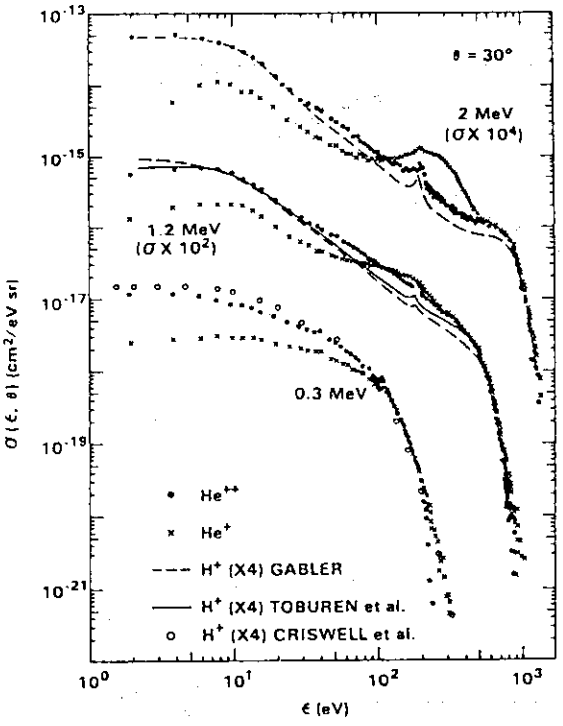

Representative electron spectra for electron emission from argon at 30° by equal velocity H^+, He^+, and He^{2+} impact. The scaled proton data are from Gabler (Ref. 10), Criswell *et al.* (Ref. 11), and Toburen *et al.* (Ref. 12).

FIG.13

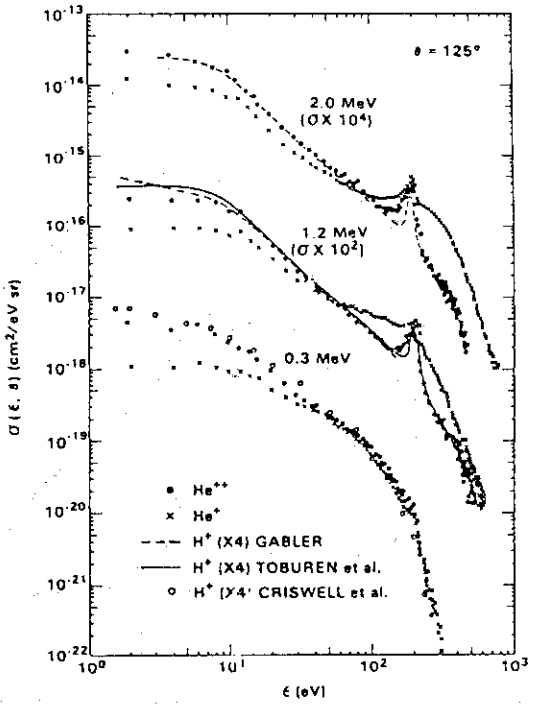

Representative electron spectra for electron emission from argon at 125° by equal velocity H^+, He^+, and He^{2+} impact. The scaled proton data are from Gabler (Ref. 10), Criswell *et al.* (Ref. 11), and Toburen *et al.* (Ref. 12).

FIG.14

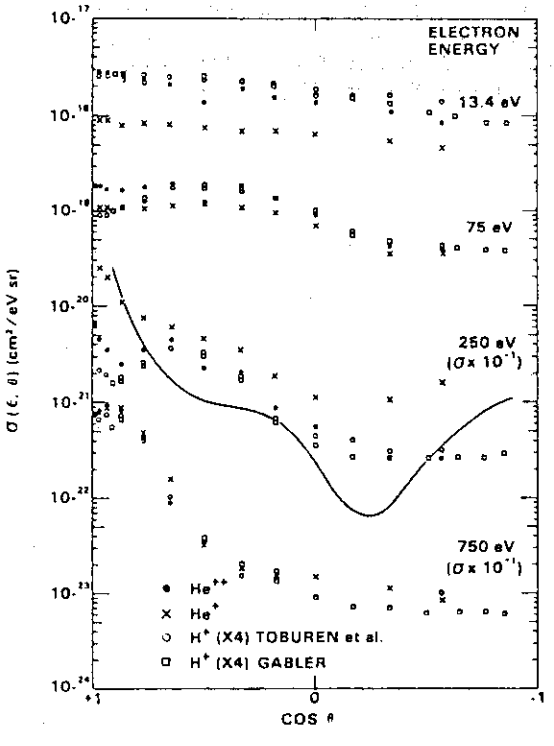

Angular distributions of electrons of selected energies ejected from 2-MeV helium ions and equal velocity protons. Scaled proton data are from Gabler (Ref. 10) and Toburen *et al.* (Ref. 12). The solid line represents elastic scattering cross sections of Williams and Willis (Ref. 16), in arbitrary units, for 250-eV electrons on argon.

FIG.15

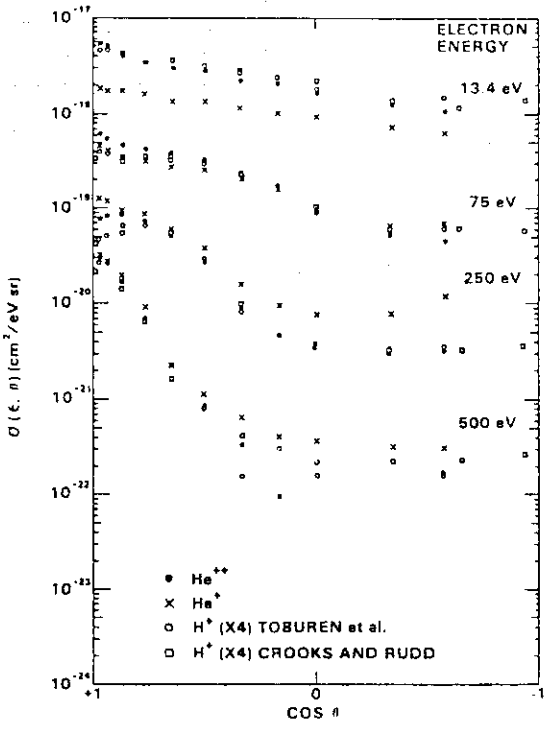

Angular distributions of electrons of selected energies ejected from argon by 1.2-MeV helium ions and equal velocity protons. The proton data are from the work of Toburen *et al.* (Ref. 12) and Crooks and Rudd (Ref. 19).

FIG.16

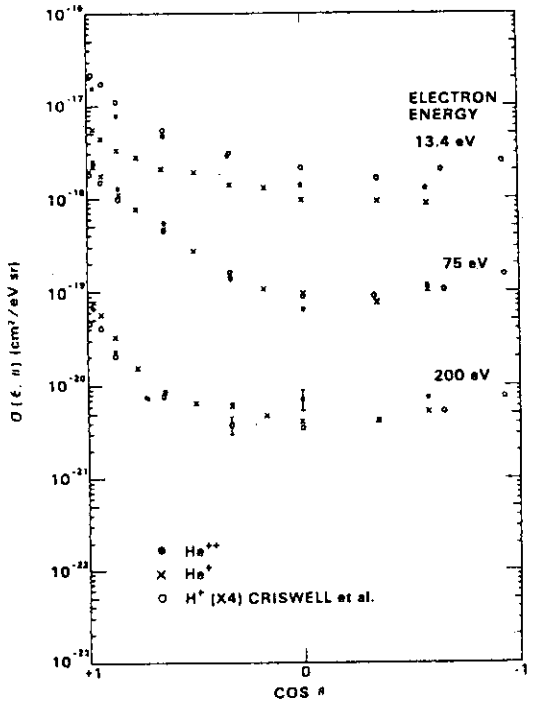

Angular distributions of electrons of selected energies ejected from argon by 0.3-MeV helium ions. The proton data of Criswell *et al*. (Ref. 11) are for 70-keV proton impact.

FIG.17

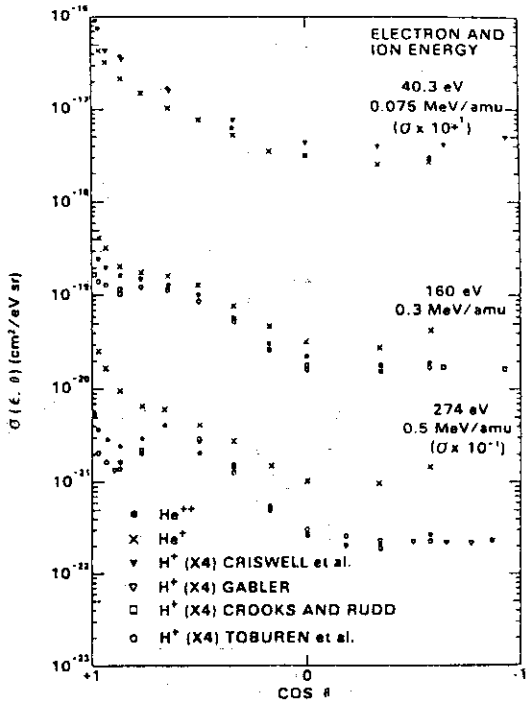

Angular distributions of electrons ejected with velocities similar to the incident ion velocities for 0.075-, 0.3-, and 0.5-MeV/amu helium ions and protons. Proton data are from Toburen *et al*. (Ref. 12), Gabler (Ref. 10), Criswell *et al*. (Ref. 11), and Crooks and Rudd (Ref. 19).

FIG.18

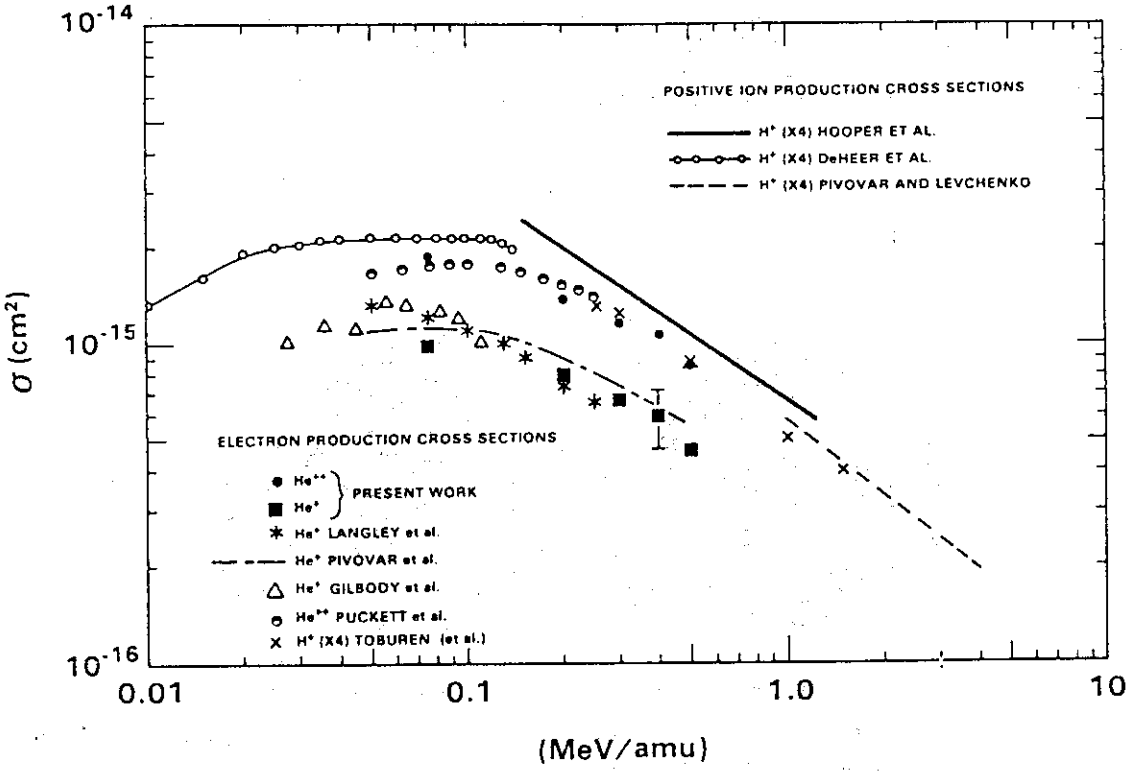

Total ionization cross sections for α particles and helium ions. The positive-ion production cross sections for proton impact of Hooper *et al*. (Ref. 33), De Heer *et al*. (Ref. 34), Pivovar and Levchenko (Ref. 35), and the proton-induced electron yield of Toburen *et al*. (Ref. 12) have been multiplied by 4 for comparison to the helium-ion data. Total electron yields for α particles of Puckett *et al*. (Ref. 31) are shown along with the He^+ results of Langley *et al*. (Ref. 28), Pivovar *et al*. (Ref. 29), and Gilbody *et al*. (Ref. 30).

FIG.19

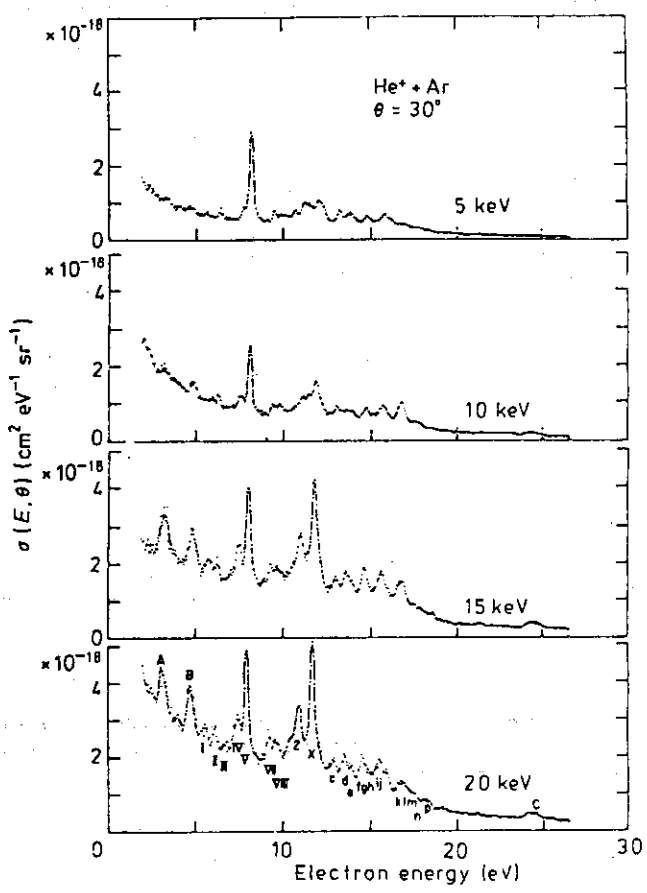

Double differential cross sections, differential in ejected-electron energy and angle, for incident 5, 10, 15 and 20 keV He^+ on argon at 30°. The peak labels (1, 2, . . . , a, b, . . . , I, II, . . .) defined by Jørgensen *et al* (1978) were used for 20 keV He^+ impact on argon except for A, B and C (see table 1 for A, B and C).

FIG.20

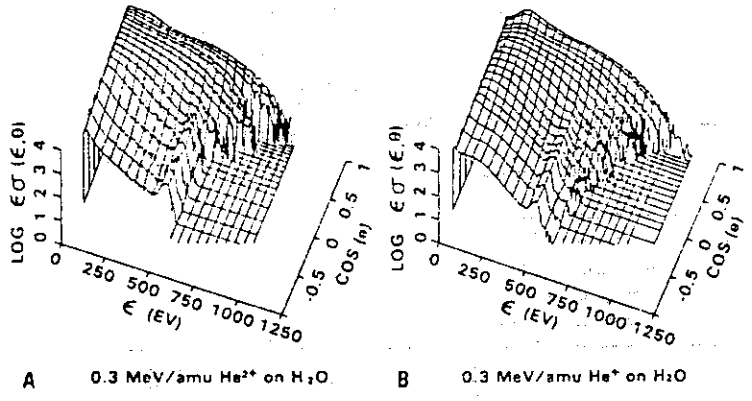

Double differential cross sections for ionization of water vapor by 0.3 MeV/amu helium ions: He^{2+} (α particle) impact and He^+ impact; $\epsilon\sigma(\epsilon,\theta)$ in units of 10^{-20} eVcm².

FIG.21

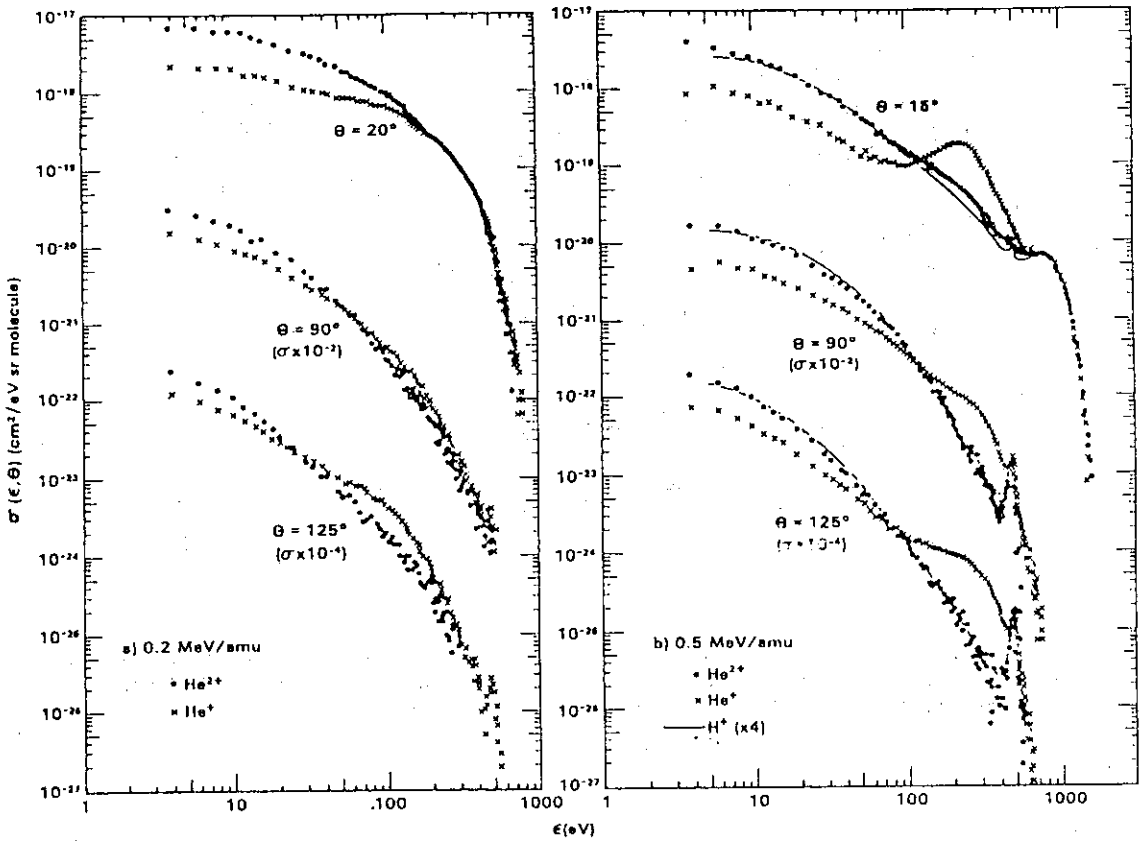

Ejected electron energy spectra for ionization of water vapor by equal velocity He^+, He^{2+}, and H^+ for selected electron emission angles. The proton data of Toburen and Wilson (7) are multiplied by 4 for Z^2 scaling.

FIG.22

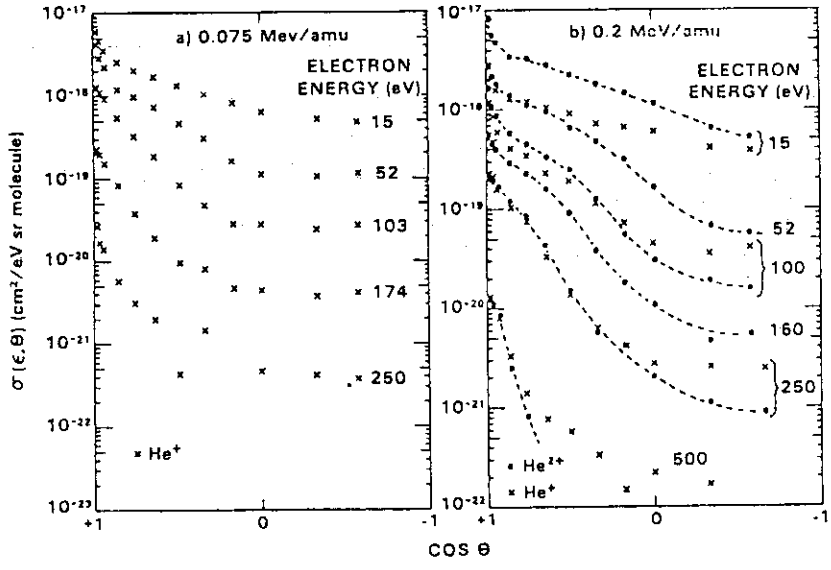

Angular distributions of electrons of selected energies ejected in the ionization of water vapor by (a) 0.075 MeV/amu He^+ ions, and (b) 0.2 MeV/amu He^+ and He^{2+} ions.

FIG.23

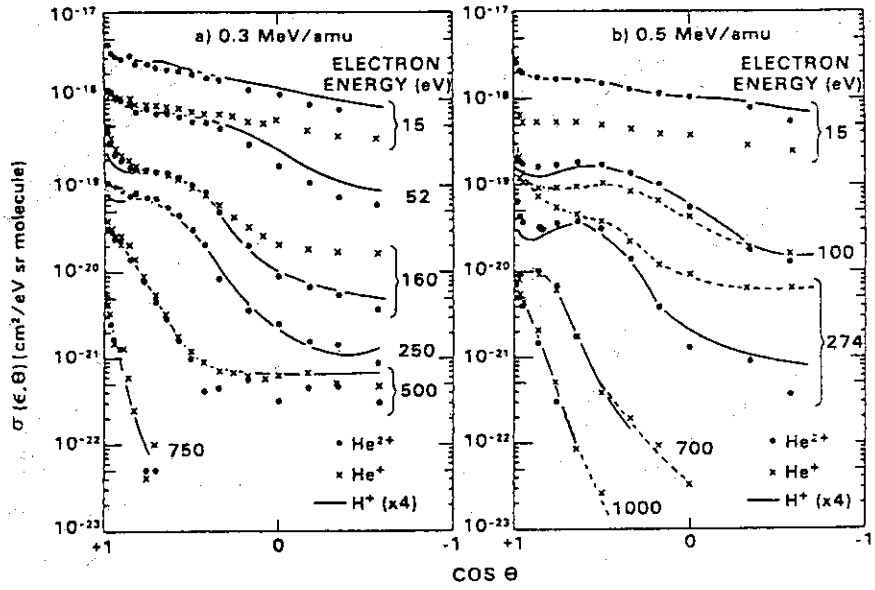

Angular distributions of electrons of selected energies ejected in ionization of water vapor by (a) 0.3 MeV/amu He^+, He^{2+}, and scaled H^+ ions, and (b) 0.5 MeV/amu He^+, He^{2+}, and scaled H^+ ions. The proton data of Toburen and Wilson (7) are multiplied by 4 for Z^2 scaling.

FIG. 24

TABLE 6

Mean Electron Energies, Total Ionization, and Partial Stopping Cross Sections

Ion energy	*He^{2+}*			*He^+*			*H^+*		
(MeV/amu)	σ_T[a]	$\bar{\varepsilon}$[b]	$\bar{\varepsilon}\sigma_T$[c]	σ_T	$\bar{\varepsilon}$	$\bar{\varepsilon}\sigma_T$	σ_T	$\bar{\varepsilon}$	$\bar{\varepsilon}\sigma_T$
0.075	1.23			0.838	39	33.0			
0.20	1.23	45	55.6	0.661	63	41.6			
0.30	0.90	52	47.1	0.557	78	43.3	0.257	45	11.6
0.40	0.95	49	46.7	0.476	92	44.1			
0.50	0.77	51	39.5	0.362	112	40.5	0.170	56	9.6

[a] σ_T in units of 10^{-15} cm².
[b] $\bar{\varepsilon}$ in units of eV.
[c] $\bar{\varepsilon}\sigma_T$ in units of 10^{-15} eVcm².

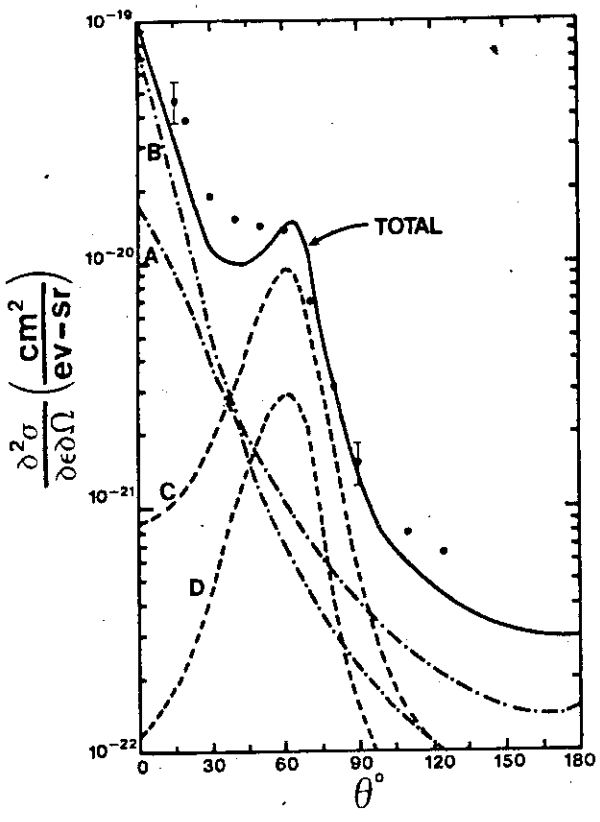

Double-differential cross section for ejecting electron of energy 16 Ry by 2-MeV He^+ incident on He. The points are experimental; the solid curve is the theoretical result which is the sum of the cross sections: line *A*, projectile ionization, target remains in ground state; line *B*, projectile ionization with simultaneous target excitation; line *C*, target ionization, projectile remains in ground state; and line *D*, target ionization with simultaneous projectile excitation.

FIG.25

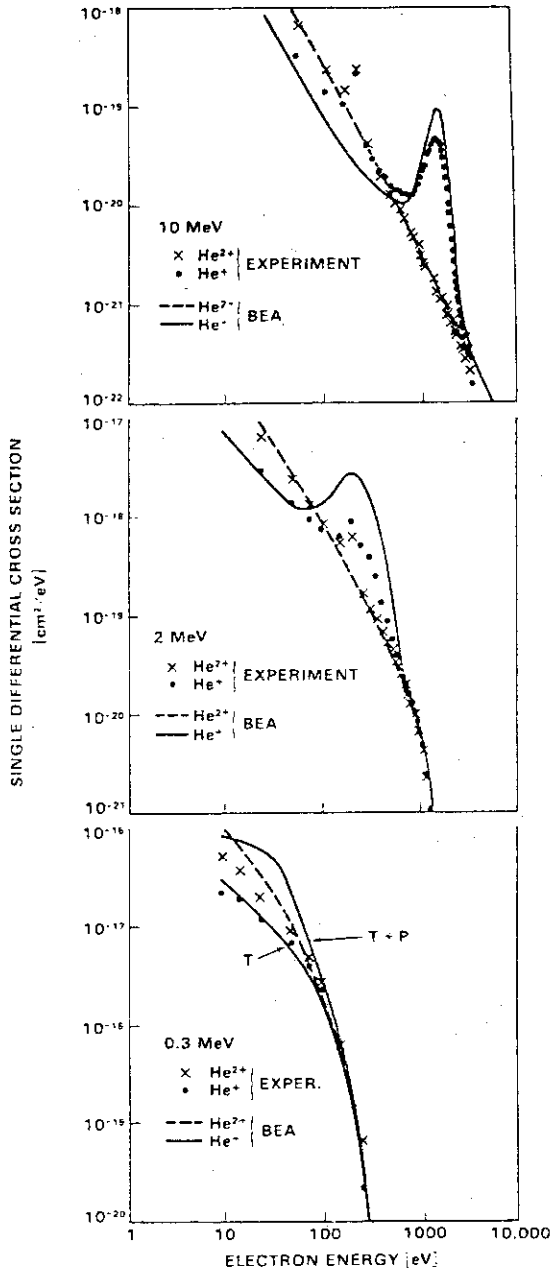

Single differential cross sections for ionization of argon by He^+ and He^{2+} ions. The 0.3 and 2.0 MeV experimental data are from Toburen and Wilson (Ref. 2), and the 10 MeV data are from Burch, et al. (Ref. 10).

FIG.26

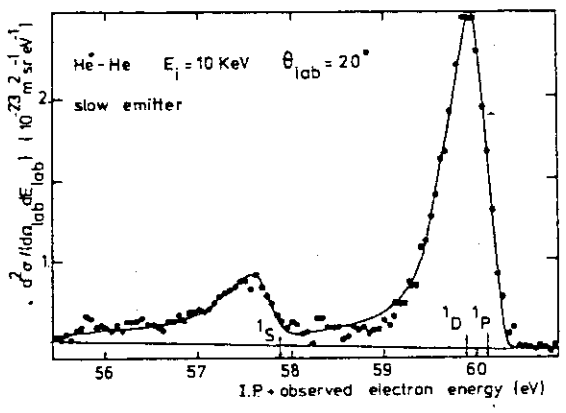

Spectra of electrons ejected by autoionization of the slow particle in He^* on He collisions at 10 keV and $\theta_{lab} = 20°$. The energy scale is calibrated against the $2p^2\,^1D$ energy state: 59.90 eV as obtained in Ref. 22. Energy resolution: 0.67% of the transmitted electron energy; channel width =0.055 eV. The continuous line is obtained by a fit of the experimental points (•) (see text).

FIG.27

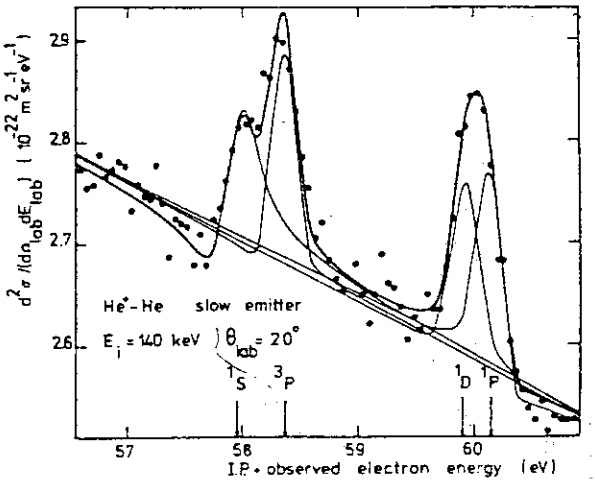

Spectra of electrons ejected by autoionization of the slow particle in He^* on He collisions at 140 keV, $\theta_{lab} = 20°$. The thin lines give the separated contributions of each autoionizing state. The other characteristics are the same as in Fig. 2, $\tilde{q}(^1S) = 2.4$, $\tilde{q}(^3P) = 15$, $\tilde{q}(^1D) = 22$, $\tilde{q}(^1P) = -7$.

FIG.28

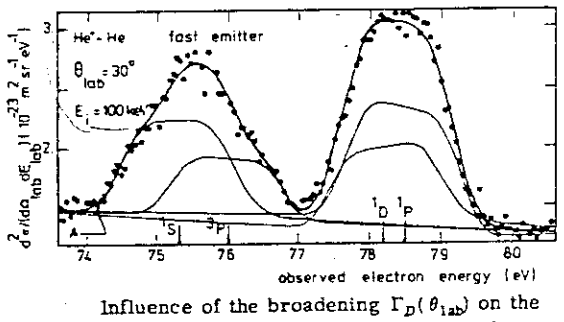

Influence of the broadening $\Gamma_D(\theta_{lab})$ on the lines issued from the fast particle at 100 keV, $\theta_{lab} = 30°$ ($\theta'_{em} = 48.3°$). Point A serves to find the ^1S line position as explained in the text. The heavy line gives the best fit obtained with the experimental points (•); the thin lines give the separated contributions of each autoionizing level. The analyzer energy resolution is equal to 1.1% of the transmitted electron energy; the channel width is equal to 0.058 eV. The abscissa is calibrated against the ^1D position; the ^1D-^1P distance is kept constant and equal to 0.360 eV [this value includes the Doppler shift and takes into account the different Doppler shift values for 35.32 eV (^1D) and 35.55 eV (^1P) electrons].

FIG.29

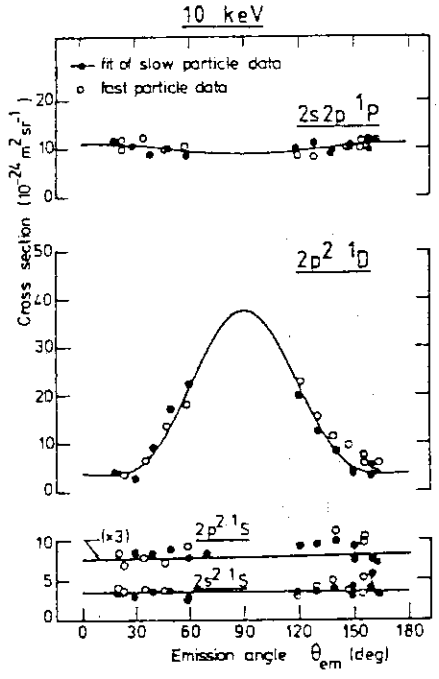

Angular distributions of the electrons emitted by the $2s^2\,^1S$, $2p^2\,^1D$, $2s2p\,^1P$, and $2p^2\,^1S$ autoionizing states at 10 keV. Only the fit of the slow-particle data (•) with relation (7′) is given by a continuous line; the fast-particle data are represented by open circles (o) and show that equal SDCS are obtained for the two particles in the emitter frame.

FIG.30

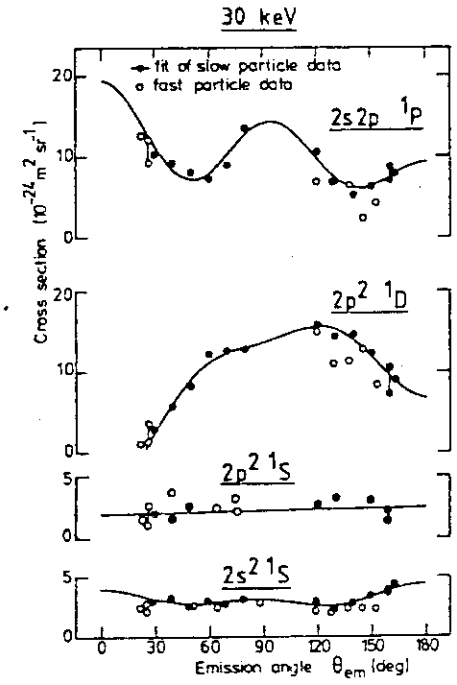

Same as Fig. 6 at 30 keV. The fit of the slow-particle data is obtained with relation (10).

FIG.31

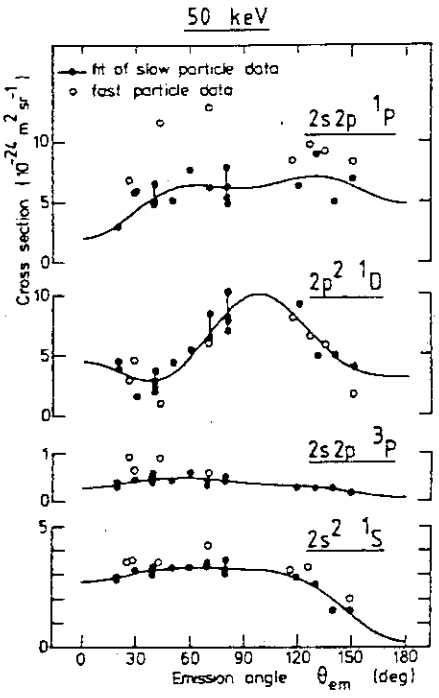

Same as Fig. 7 at 50 keV. The discrepancies between the fast- and slow-particle SDCS for the ^1P line must be noted.

FIG.32

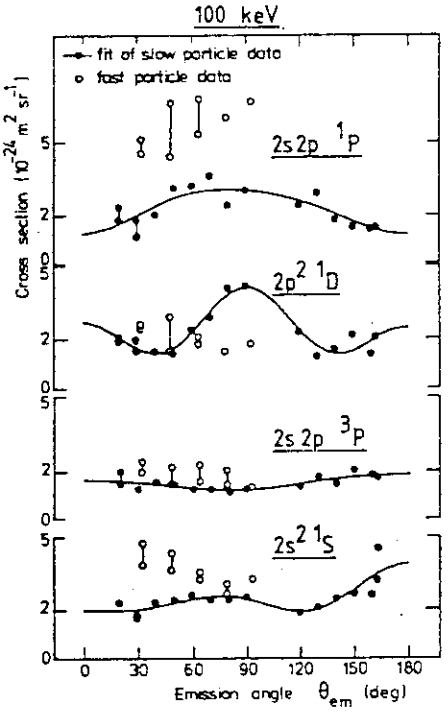

Same as Fig. 7 at 100 keV.

FIG.33

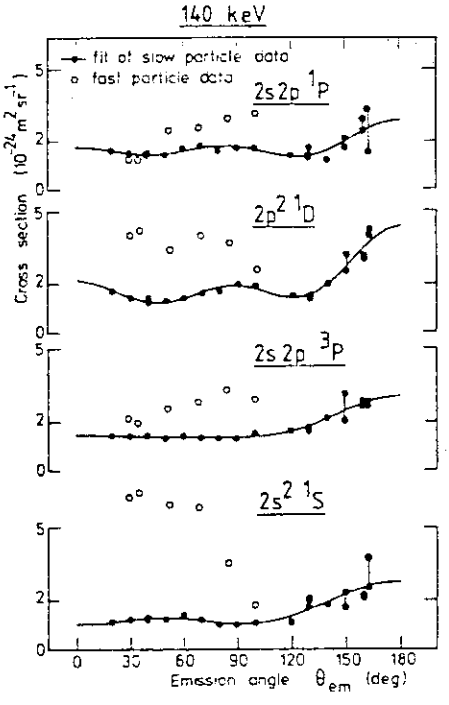

Same as Fig. 7 at 140 keV.

FIG.34

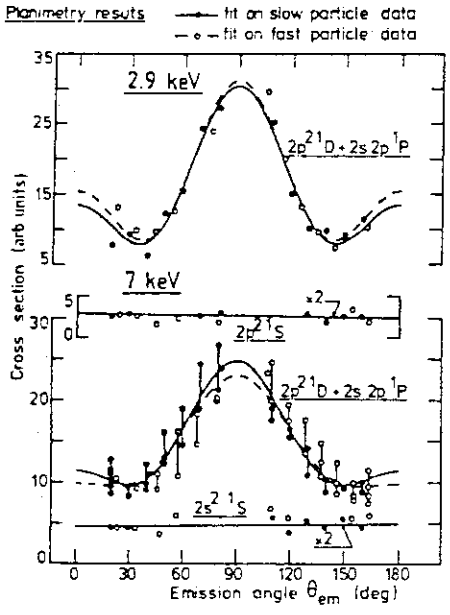

Angular dependence of the $(2p^{2\,1}D + 2s2p\,^1P)$ line as measured by planimetry at 2.9 and 7 keV. The $2s^{2\,1}S$ values are certainly affected by PCI interference with the ^1D and ^1P states (see the energy spectra given in Ref. 17 at 7 keV). The fit is obtained with relation (7').

FIG.35

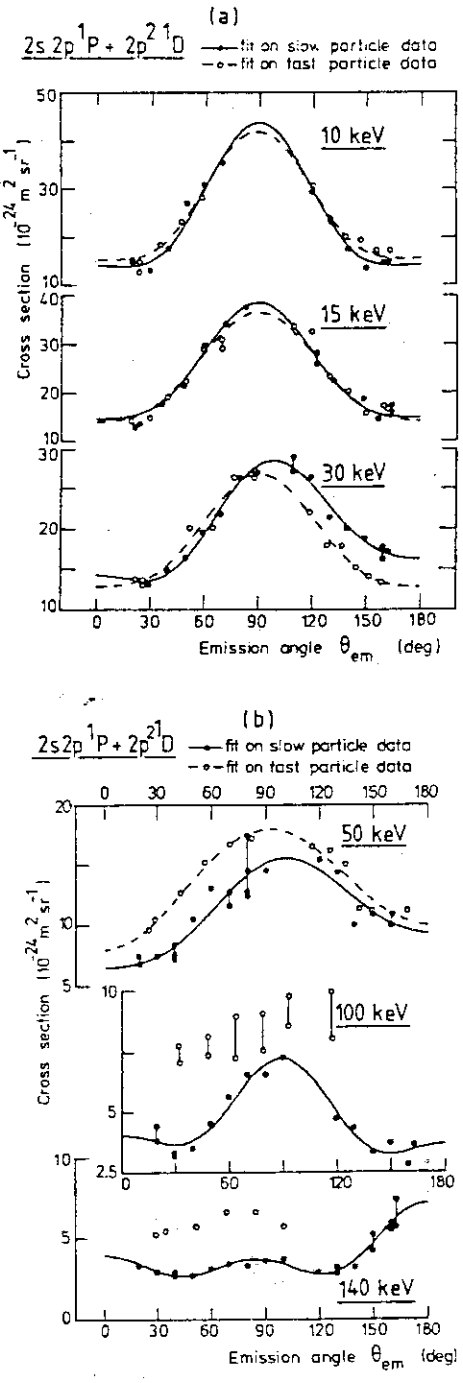

Angular dependence of the $(2p^{2\,1}D + 2s2p\,^1P)$ line. The separated fits of the fast-particle data (broken lines) and slow-particle data (continuous line) are obtained with relation (7') at 10 and 15 keV and with relation (10) at 30 keV and above. (a) Results obtained at 10, 15, and 30 keV. (b) 50, 100, and 140 keV data. The asymmetry of the angular distributions with respect to $\theta_{em} = 90°$ and the difference between fast- and slow-particle SDCS values are clearly seen at 30 keV and above.

FIG.36

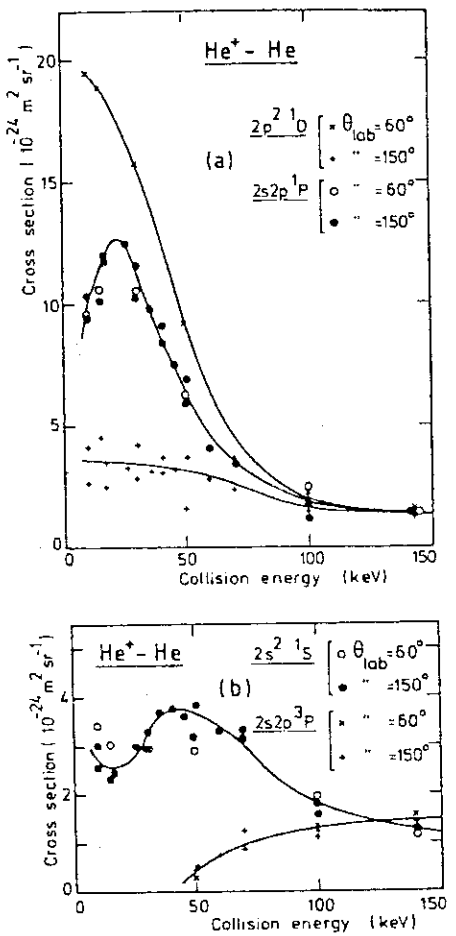

Energy dependence of the single differential cross section for the excitation of the $2s^2\,^1S$, $2s2p\,^3P$, $2p^2\,^1D$, and $2s2p\,^1P$ autoionizing states. (a) $2p^2\,^1D$: (×) $\theta_{lab} = 60°$; (+) $\theta_{lab} = 150°$. $2s2p\,^1P$: (○) $\theta_{lab} = 60°$; (●) $\theta_{lab} = 150°$. (b) $2s^2\,^1S$: (○) $\theta_{lab} = 60°$; (●) $\theta_{lab} = 150°$. $2s2p\,^3P$: (×) $\theta_{lab} = 60°$; (+) $\theta_{lab} = 150°$.

FIG. 37

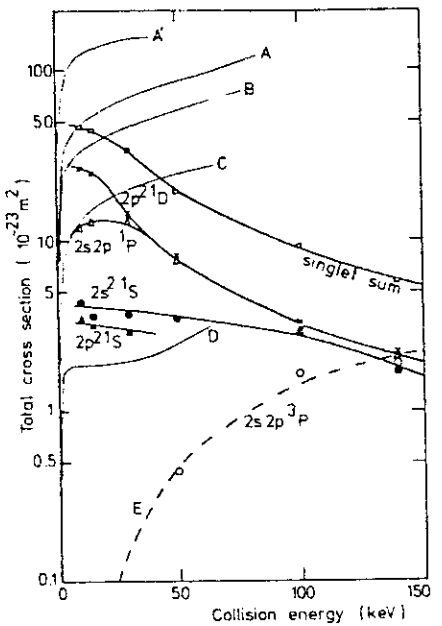

Variation of the experimental total cross section for excitation of the slow particle with collision energy. The theoretical curves labeled A', A, B, C, D are taken from Koike's papers for He^{2+} on He collision; they correspond to the excitation of the following molecular states (Ref. 55) (see Fig. 15): A ($B\Sigma_g + C\Sigma_g + \Delta_g$), B ($\Delta_g$), C ($B\Sigma_g$), D ($C\Sigma_g$). Curve A' is calculated from Ref. 59 with $Z_{eff} = 1.5$ as explained in the text and corresponds to the excitation of the $C\Sigma_g + \Delta_g$ molecular states. All these theoretical cross sections (Refs. 55 and 59), which give the excitation of both particles, are divided by two in order to be compared with the experimental data. Curve E gives the fit of the ^3P data with Demkov's formula $\sigma = k[1/\exp(a/v)]^{-1}$ with $k = 21.6$, $a = 2.7$; the collision velocity is given in atomic units.

FIG. 38

TABLE 7

Total cross sections for the various autoionizing states in He^+ on He collisions. All the values are given in 10^{-23} m² units; they have been obtained by a fit of the experimental values by relations (7') or (10) (see text). This explains small discrepancies between the values given for ($2p^2\,^1D + 2s2p\,^1P$) and the $2p^2\,^1D$ and $2s2p\,^1P$ sum of the separated contributions. The labels F and S mean that the fast- and slow-particle excitation are considered.

Collision energy (keV)		10	15	30	50	100	140
$2s^2\,^1S$	S	4.4	3.6	3.7	3.5	2.9	1.7
	F	4.6	3.6	3.1			
$2s2p\,^3P$	S				0.45	1.7	1.9
$2p^2\,^1D\,\lvert M_L\rvert = 2$	S	24.6	22.2				
	F	21.2	19.4				
$\lvert M_L\rvert = 1$	S	0.8	0.7				
	F	2.7	1.8				
$\lvert M_L\rvert = 0$	S	0.8	1.7				
	F	1.0	1.1				
total	S	26.2	(24.6)	14.5	8.1	3.3	2.2
	F	24.9	22.3				
$2s2p\,^1P\,\lvert M_L\rvert = 1$	S	7.1	8.4				
	F	6.5	8.2				
$\lvert M_L\rvert = 0$	S	4.6	4.3				
	F	4.7	4.6				
total	S	11.7	(12.6)	13.0	7.6	3.2	2.0
	F	11.2	12.8				
$2p^2\,^1D + 2s2p\,^1P$	S	36.7	(34.0)	27.5	15.6	6.5	4.3
	F	36.7	34.3	25.8	18.8		
$2p^2\,^1S$	S	3.5	3.2	2.9			
sum of the measured singlet cross sections	S	45.8	44.1	34.1	19.2	9.4	5.9

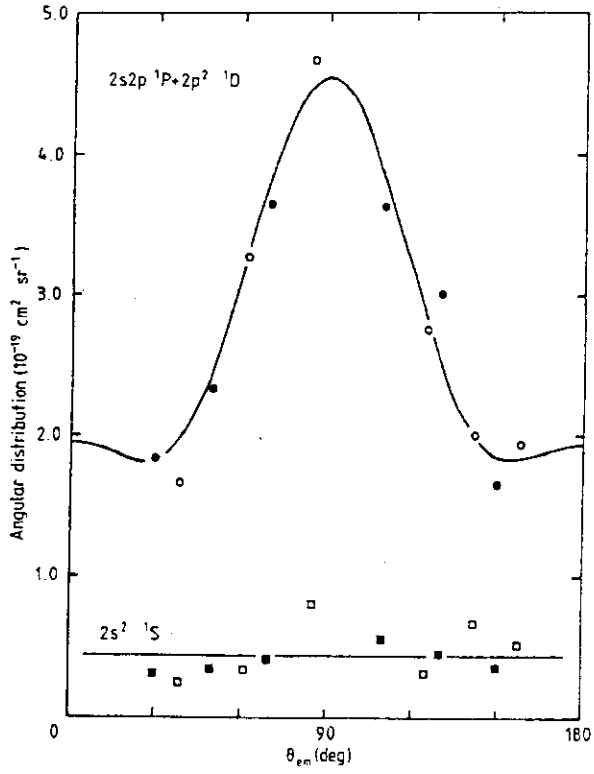

Angular distributions for electrons ejected from autoionisation states for 20 keV He^+–He collisions in the emitter frame. $2p^2\,{}^1D + 2s2p\,{}^1P$ states: ● from the target; ○ from the projectile. $2s^2\,{}^1S$ state: ■ from the target; □ from the projectile.

FIG.39

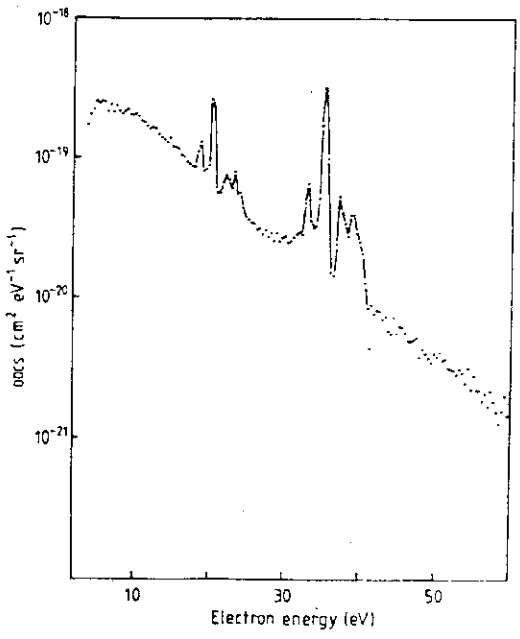

A typical ejected electron spectrum; double-differential cross sections, differential in ejected electron energy and angle, for 20 keV He^+ on He at 150°.

FIG.40

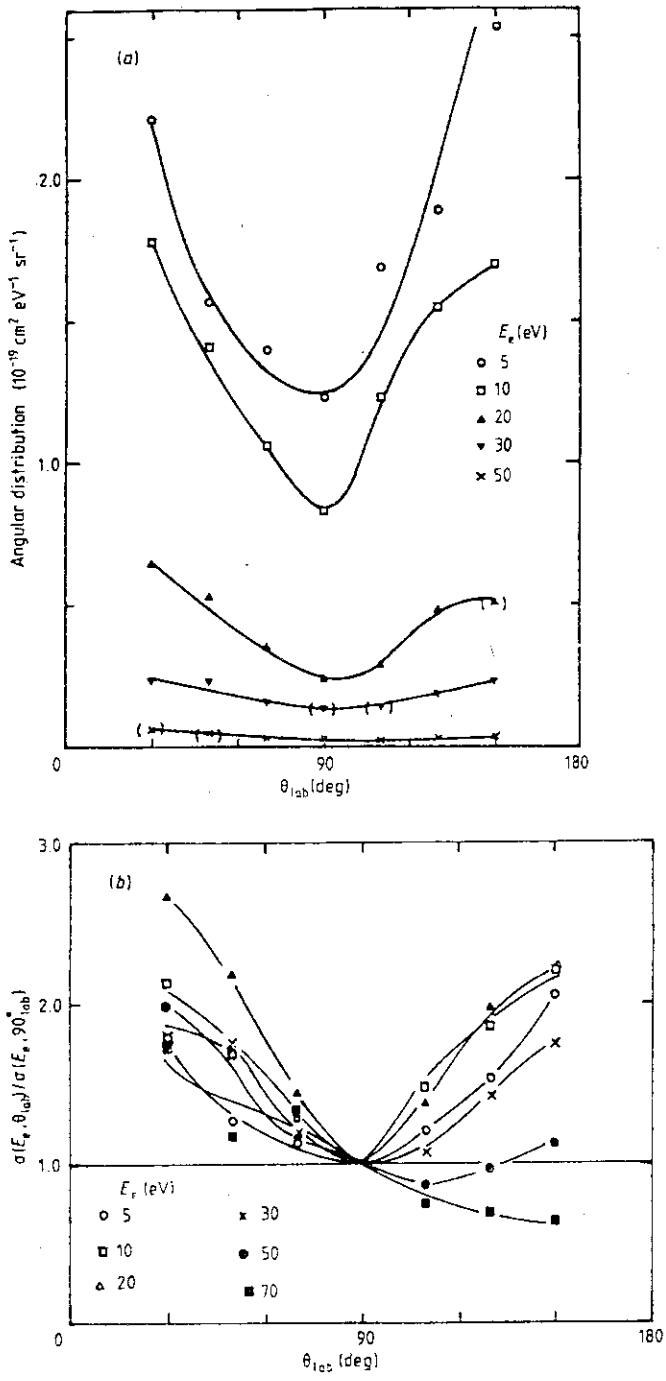

(*a*) Angular distributions for electrons in the continuous part of electron spectra for 20 keV He^+-He collisions in the laboratory system; electron energy: ○, 5 eV; □, 10 eV; △, 20 eV; ▽, 30 eV; ×, 50 eV. Data points given in parentheses are obtained by subtraction of the contribution of the autoionisation peak from the observed electron spectra using the subtraction procedure described in the text. (*b*) The ratios $\sigma(E_e, \theta_{lab})/\sigma(E_e, 90°_{lab})$. ○, 5 eV; □, 10 eV; △, 20 eV; ×, 30 eV; ●, 50 eV; ■, 70 eV.

FIG.41

TABLE 8

K-shell ionization cross sections of CH_4, N_2, and Ne by 50–600 keV H^+ and He^+ impact.

Energy / Mass (keV/amu)	H^+ impact CH_4	N_2 (10^{-20} cm^2)	Ne	He^+ impact CH_4	N_2 (10^{-20} cm^2)	Ne
600	95.4	···	4.54	···	···	····
500	92.4	38.9	3.59	···	···	···
400	84.2	36.2	2.61	···	···	···
300	74.6	25.9	1.66	···	···	···
250	···	···	1.25	···	···	···
200	50.1	14.7	0.624	···	···	···
150	32.3	9.0	0.283	132	30.0	0.512
125	24.0	6.05	0.161	93	15.5	0.242
100	16.1	3.54	0.073	49.1	7.9	0.123
75	8.3	1.46	···	17.2	2.83	0.039
62.5	4.9	0.85	···	9.0	1.25	···
60	3.95	0.72	···	···	···	···
50	2.37	0.422	···	4.52	0.59	0.0069
43.8	···	···	···	2.38	0.374	···
37.5	···	···	···	1.55	0.182	···
33.8	···	···	···	0.83	0.118	···

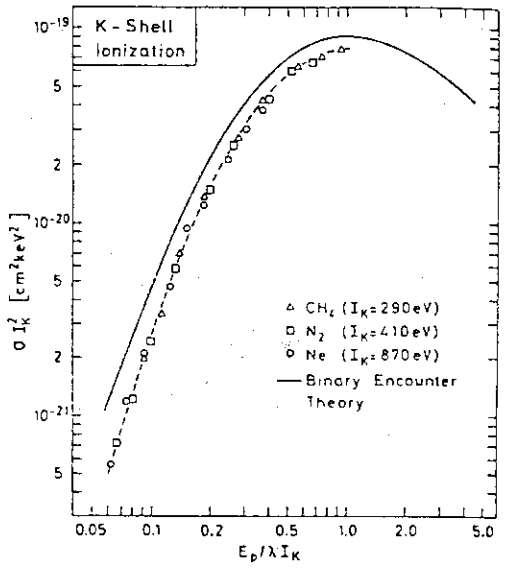

Scaled cross sections for K-shell ionization of CH_4, N_2, and Ne vs proton energy E_p. Scaling parameters are the K-shell ionization potential I_K and the mass ratio λ for protons and electrons. The binary encounter results are from Garcia *et al.* (Ref. 3).

FIG. 42

TABLE 9

K-shell ionization cross sections (in units of 10^{-19} cm^2).

Projectile energy (MeV)	N_2 H^+	N_2 He^+	F (SF_6) H^+	F (SF_6) He^+	Ne H^+	Ne He^+
1	6.0	9.74	0.94	0.21	1.30	0.74
2	4.60	20.4	1.00	1.33	1.42	2.67
3	4.36	25.2	0.990	2.40	1.29	3.70
4	3.51	21.8	0.92	3.40	1.06	4.40
5	2.81	18.7	0.846	3.89	0.95	4.70

FIG.43

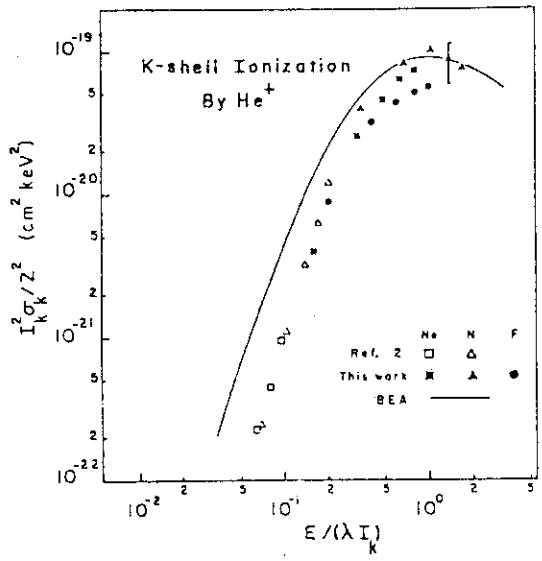

Experimental *K*-shell ionization cross sections for He^+ bombardment compared to BEA. The earlier work of Stolterfoht *et al.* (Ref. 2) is also shown.

FIG.44

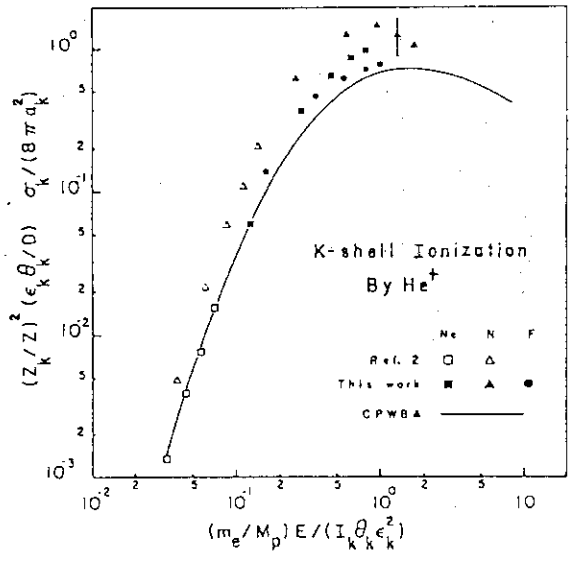

Experimental *K*-shell ionization cross sections for He^+ bombardment compared to the CPWBA. The earlier work of Stolterfoht *et al.* (Ref. 2) is also shown.

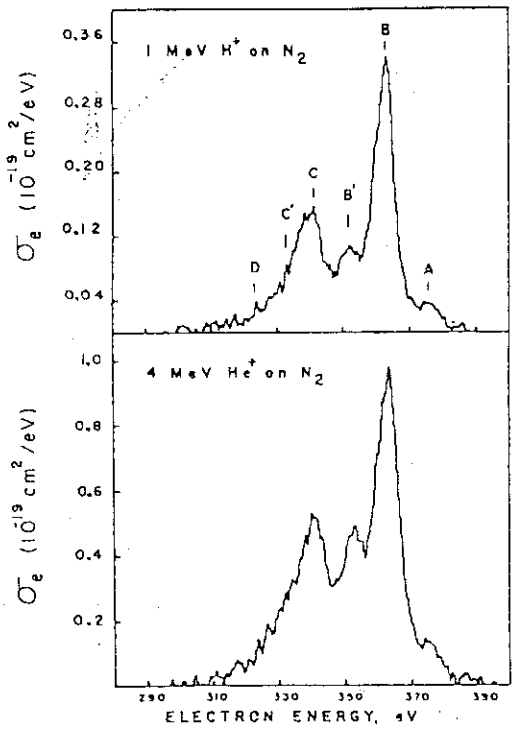

Typical N_2 (*KLL*) Auger-electron spectra for equal velocity H^+ and He^+ bombardment. Peak regions identified by Letters *A*–*D* are discussed in the text.

FIG.45

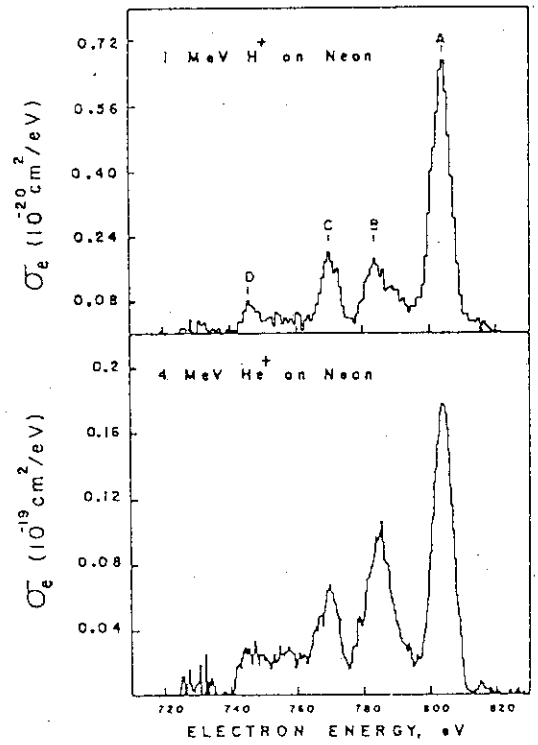

Neon (*KLL*) Auger-electron spectra produced by equal velocity H^+ and He^+ bombardment. Peak regions A, B, C, and D are discussed in the text.

FIG.46

TABLE 10

Cross sections (in units of 10^{-18} cm^2) for the Ne−2*s*, Ar−3*s*, and Kr−4*s* vacancy production with (a) H_2^+ impact and (b) He^+ impact as a function of the projectile energy *E*

(a) H_2^+ impact				(b) He^+ impact			
E [keV]	Ne−2*s*	Ar−3*s*	Kr−4*s*	*E* [keV]	Ne−2*s*	Ar−3*s*	Kr−4*s*
100	43.3	40.6	38.8	100			31.7
125	49.4	39.3	39.5	125		36.2	27.1
150	52.0	38.1	40.2	150	70.6	32.4	25.0
175	53.8	35.0	37.9	175		30.3	
200	53.2	33.7	35.5	200	70.2	28.5	23.5
250	51.5	30.5	29.6	250	66.8	27.7	24.2
300	49.5	27.8	26.3	300	67.4	27.3	24.3
350	47.6	26.0	24.6				
400	43.9	24.5	23.2	400	60.9	26.4	24.4
500	39.6	21.7	20.0	500	57.0	24.3	23.5
600	36.6	19.8	18.1	600	53.9	23.8	22.4
700	32.3	17.5	16.2	700	53.2	23.5	20.9
800	30.4	16.4	15.0	800	49.7	22.1	20.3
900	28.8	14.5	13.5	900	47.0	21.4	19.5
1000	27.3	13.6	12.4	1000	45.2	20.2	18.2

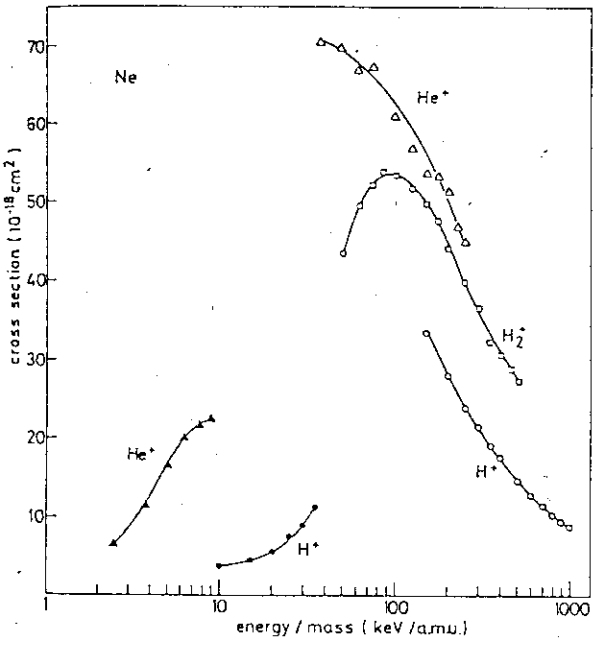

Comparison of cross section data for the Ne−2*s* ionization with: H^+: ● Van Eck *et al.* [2]. ○ Hippler and Schartner [1]; H_2^+: □ present results; He^+: ▲ Van Eck *et al.* [2]. △ present results

FIG. 47

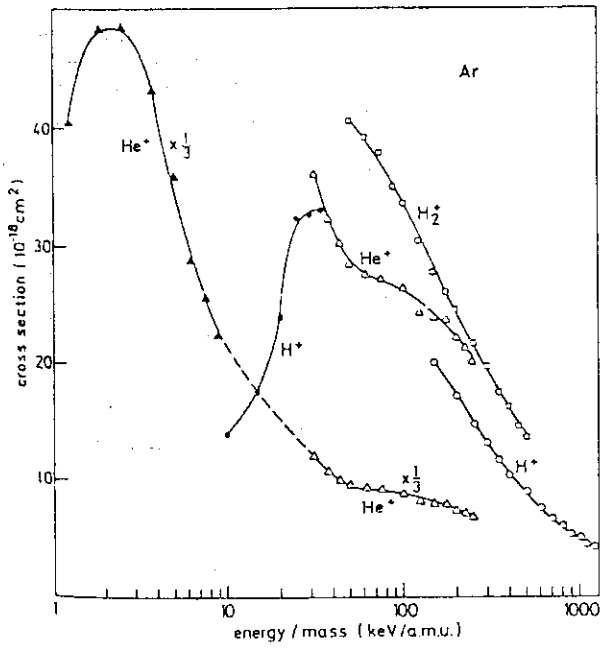

Comparison of cross section data for the Ar−3*s* ionization with: H^+: ● Van Eck *et al.* [2]. ○ Hippler and Schartner [1]; H_2^+: □ present results; He^+: ▲ Van Eck *et al.* [2]. △ present results

FIG. 48

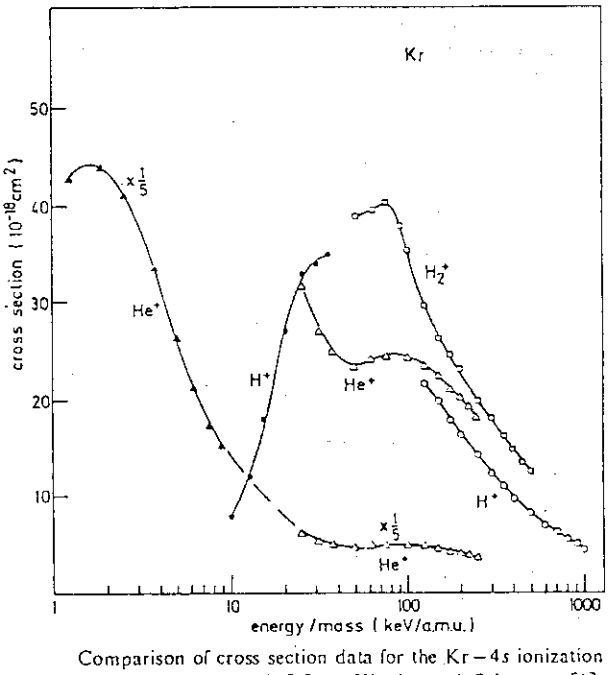

Comparison of cross section data for the Kr−4*s* ionization with: H^+: ● Van Eck *et al.* [2]. ○ Hippler and Schartner [1]; H_2^+: □ present results; He^+: ▲ Van Eck *et al.* [2]. △ present results

FIG. 49

TABLE 11

Total Ne *K*-Auger cross sections.

Projectile	E/m (MeV/amu)	$\sigma(10^{-20}$ cm$^2)$
H^+	0.3	1.91, 1.66[a]
	0.4	3.35, 2.6[a]
	0.5	4.51, 3.5[a], 3.9[b]
	0.6	5.47, 4.8[b]
	0.7	6.54
	0.8	7.37
	0.9	7.90
	1.0	8.2, 8.5[b]
	1.5	9.63, 10.4[b]
$^{3,4}He^{2+}$	0.30	11.0
	0.40	15.6
	0.50	22.5
	0.67	28.0
	0.75	31.6
	1.0	36.7
	1.08	37.5
	1.33	39
	1.53	33.5
	2.01	31.7
	3.02	31.8
	4.04	30.3
$^{7}Li^{3+}$	0.714	74.8
	0.914	88.3
	1.14	102
	1.43	102
	1.71	111
	2.14	105
	2.89	89.7

[a] Stolterfoht and Schneider, Ref. 19.
[b] Woods *et al.*, Ref. 38.

TABLE 12

Total *C K*-Auger cross sections.

Projectile	E/m (MeV/amu)	$\sigma(10^{-18}$ cm$^2)$
H^+	0.2	0.62, 0.50[a]
	0.25	0.68
	0.3	0.84, 0.75[a]
	0.4	0.99, 0.84[a]
	0.5	1.01, 0.92[a]
	0.6	1.07, 0.95[a]
	0.8	1.08
	1.0	0.90, 1.08[b]
	1.5	0.82, 0.85[b]
	2.0	0.68, 0.80[b]
$^{3,4}He^{2+}$	0.15	2.0
	0.20	2.9
	0.25	3.6
	0.30	3.8
	0.40	4.8
	0.50	5.1
	0.67	5.2
	0.75	5.3
	1.016	4.7
	1.53	3.8
	2.01	2.8
	3.02	2.1
	4.04	2.1
$^{7}Li^{3+}$	0.714	10.8
	0.914	9.7
	1.14	10.1
	1.43	9.2
	1.71	8.2
	2.14	7.1

[a] Stolterfoht and Schneider, Ref. 19.
[b] Toburen, Ref. 20.

TABLE 13

Coincidence ratios and *K*-shell capture cross sections from Ne.

Projectile	E/m (MeV/amu)	σ_{CK}/σ_{VK}(%)	$\sigma_{CK}(10^{-21}$ cm$^2)$
H^+	0.4	5.1 ± 0.8	1.53 ± 0.23
	0.45	4.1 ± 0.8	1.77 ± 0.15
	0.5	5.9 ± 0.5	2.50 ± 0.21
	0.6	4.6 ± 0.2	2.46 ± 0.1
	0.7	4.95 ± 0.2	3.13 ± 0.13
	0.8	4.5 ± 0.4	3.20 ± 0.28
	1.0	3.17 ± 0.15	2.60 ± 0.12
	1.25	2.45 ± 0.3	2.25 ± 0.27
	1.5	1.75 ± 0.2	1.70 ± 0.20
$^{3}He^{2+}$	0.5	30.5 ± 3	67.1 ± 6.6
	0.667	24 ± 1.5	69.6 ± 4.4
	0.80	22 ± 3	71.5 ± 10
	1.2	14.5 ± 1.5	56.6 ± 6
	1.33	12.8 ± 1.5	50.6 ± 6
$^{7}Li^{3+}$	1.0	30 ± 6	285 ± 57
	1.41	22.5 ± 2	259 ± 24
	1.71	17.5 ± 2	193 ± 21
	2.0	15 ± 2	162 ± 22
	2.5	8.6 ± 1.5	86 ± 15
	3.0	6.8 ± 1.0	63 ± 10

TABLE 14

Coincidence ratios and *K*-shell capture cross sections from CH_4.

Projectile	E/m (MeV/amu)	σ_{CK}/σ_{VK}(%)	$\sigma_{CK}(10^{-19}$ cm$^2)$
H^+	0.2	10.9 ± 0.7	0.63 ± 0.04
	0.25	10.7 ± 0.8	0.74 ± 0.06
	0.3	10.4 ± 0.5	0.83 ± 0.04
	0.4	9.35 ± 0.5	0.87 ± 0.05
	0.5	7.4 ± 0.3	0.74 ± 0.03
	0.6	5.3 ± 0.15	0.55 ± 0.02
	0.8	3.2 ± 0.2	0.33 ± 0.02
	1.0	2.0 ± 0.2	0.20 ± 0.02
	1.25	1.32 ± 0.1	0.12 ± 0.01
	1.50	0.72 ± 0.04	0.060 ± 0.003
	1.75	0.54 ± 0.05	0.042 ± 0.004
	2.0	0.32 ± 0.03	0.023 ± 0.002
$^{3}He^{2+}$	0.23	40 ± 4	13.6 ± 1.4
	0.27	46 ± 5	17.5 ± 1.9
	0.33	37 ± 3	16.0 ± 1.9
	0.40	37 ± 3	17.6 ± 1.3
	0.46	36 ± 3	18.0 ± 1.6
	0.50	35 ± 1.5	17.9 ± 0.8
	0.53	32 ± 1.5	17.1 ± 0.8
	0.60	28.5 ± 1	14.8 ± 0.5
	0.67	24.8 ± 1	12.8 ± 0.6
	0.8	17.7 ± 1	8.80 ± 0.6
	0.92	13.6 ± .8	6.6 ± 0.4
	1.0	12.2 ± 0.8	5.7 ± 0.4
	1.2	8.1 ± 0.5	3.0 ± 0.22
$^{7}Li^{3+}$	1.14	17 ± 1.5	16.6 ± 1.5
	1.41	10 ± 1	8.7 ± 0.9
	1.71	6.6 ± 0.7	5.3 ± 0.6
	2.0	4.3 ± 0.6	3.1 ± 0.4

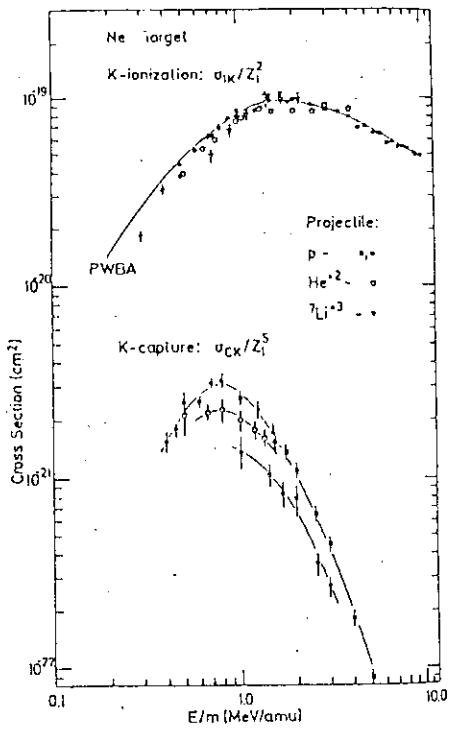

Scaled experimental ionization and capture cross sections for the Ne K shell. The filled squares are data from Ref. 4, the other points from this work. See text for definition of σ_{iK}. PWBA is from Ref. 21.

FIG.50

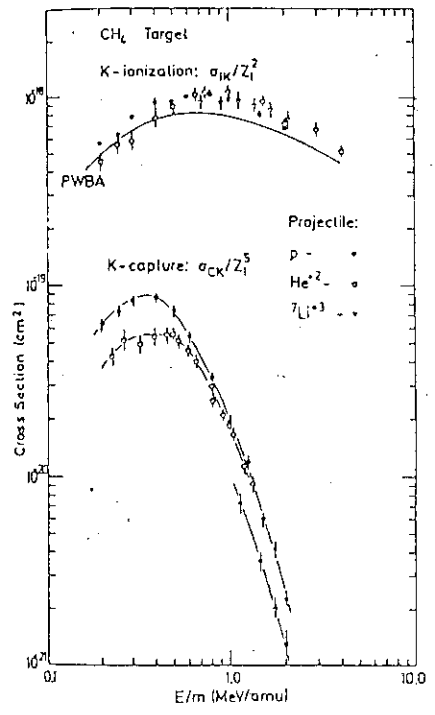

Scaled experimental ionization and capture cross sections for the C K shell. See text for definition of σ_{iK}. PWBA is from Ref. 21.

FIG.51

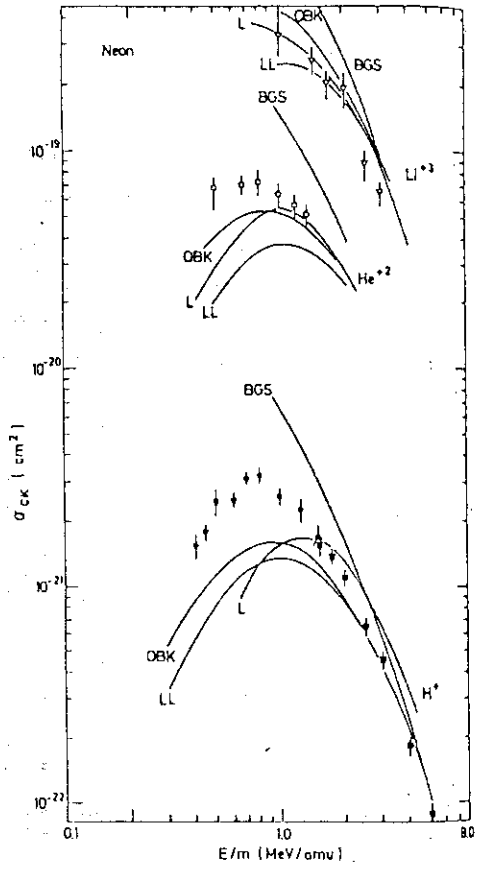

K-capture cross sections from Ne by H^+, He^{2+}, and Li^{3+}, compared with theoretical calculations of: Nikolaev,[27] σ^K_{OBK}, divided by 3 (OBK); Lapicki and Losonsky[14] (LL); Lin[34] (L); Belkić, Gayet, and Salin[36] (BGS).

FIG.52

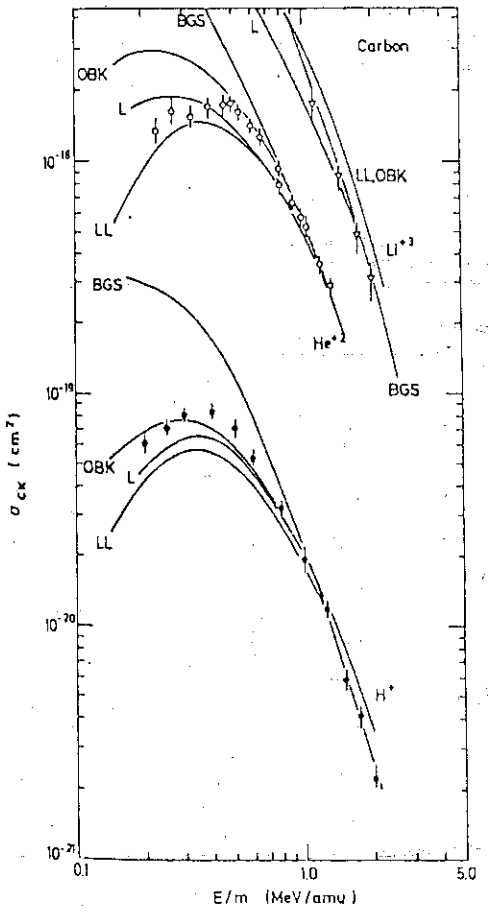

K-capture cross sections from C (in methane) by H^+, He^{2+}, and Li^{3+}. Comparisons with theory are as in Fig. 9.

FIG.53

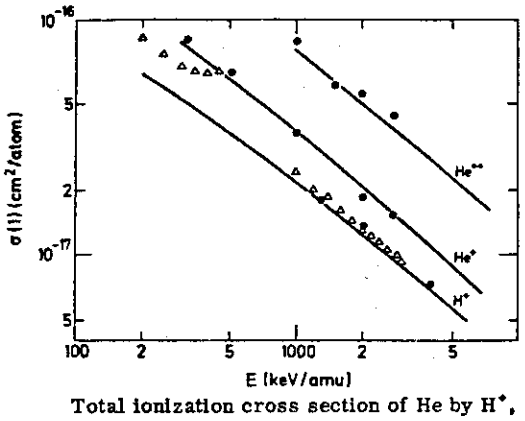

Total ionization cross section of He by H^+, He^+, and He^{2+}. Solid line represents the Bethe-Born calculation of Gillespie (Ref. 22). • denotes present experimental results; Δ experimental results of Pivovar *et al.* (Ref. 27) and Pivovar and Levchenko (Ref. 26).

FIG.54

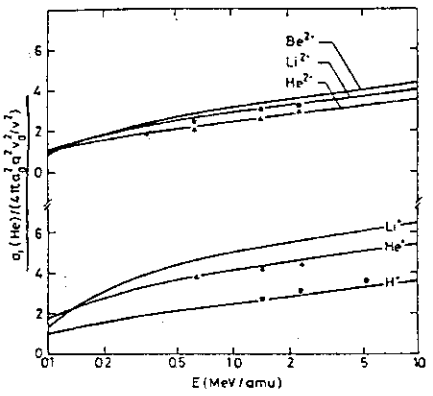

Fano plot showing comparison of present experimental data for H (●), He (▲), and Li (■) ions with the calculations of Gillespie.

FIG.55

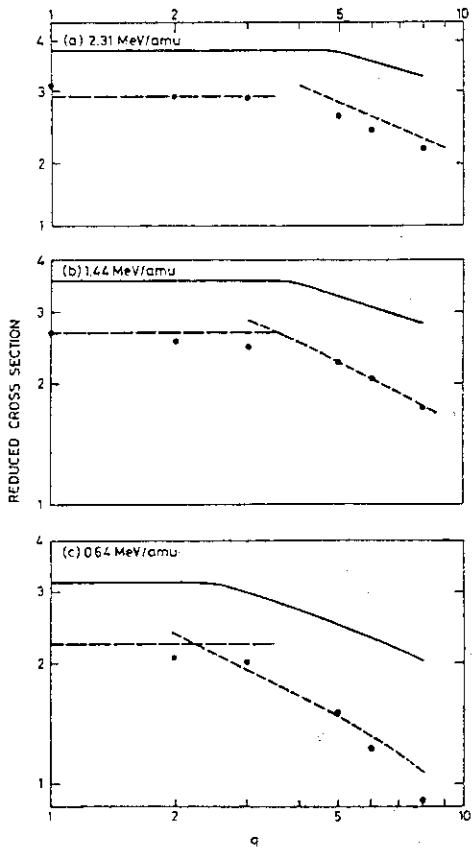

$\sigma_i/(4\pi a_0^2 q^2 v_0^2/v^2)$ for incident bare projectiles at three reduced energies. Points represent experimental data, while the theoretical models of Bohr (solid), Janev (short dash), and Bethe (long dash) are indicated as continuous curves.

FIG.56

TABLE 15

Cross sections $\sigma_{2p}(H_2)$, $\sigma_{2s}(H_2)$, $\sigma_{2p}(H)$ and $\sigma_{2s}(H)$ in units of 10^{-17} cm^2 for formation of H(2p) and H(2s) in He^+–H_2 and He^+–H collisions.

Energy (keV)	$\sigma_{2p}(H_2)$	$\sigma_{2s}(H_2)$	$\sigma_{2p}(H)$	$\sigma_{2s}(H)$
5	3·77 ± 0·40	no data	3·44 ± 1·18	no data
6	3·61 ± 0·18	0·81 ± 0·21	3·98 ± 0·78	1·40 ± 1·31
7	3·79 ± 0·13	0·26 ± 0·50	3·43 ± 0·44	0·26 ± 1·51
8	3·72 ± 0·20	1·05 ± 0·34	4·92 ± 0·59	0·66 ± 1·25
9	3·72 ± 0·30	0·61 ± 0·43	5·07 ± 0·42	0·40 ± 0·43
10	4·28 ± 0·28	1·04 ± 0·44	4·15 ± 0·38	—
11	4·02 ± 0·40	0·50 ± 0·38	4·58 ± 0·37	0·42 ± 0·36
12	4·50 ± 0·21*	0·85 ± 0·44	4·44 ± 0·35	0·37 ± 0·42
13	4·50 ± 0·16	0·91 ± 0·38	4·24 ± 0·38	0·08 ± 0·49
14	4·64 ± 0·30	0·59 ± 0·36	4·38 ± 0·15	0·59 ± 0·62
15	4·76(norm)	0·98 ± 0·25	4·07 ± 0·20	0·22 ± 0·71
16	4·61 ± 0·15	0·70 ± 0·29	4·62 ± 0·29	0·64 ± 0·59
17	4·79 ± 0·23	0·41 ± 0·29	4·14 ± 0·23	0·47 ± 0·40
18	4·83 ± 0·13	0·69 ± 0·19	4·65 ± 0·41	1·52 ± 0·66
19	4·89 ± 0·25	0·75 ± 0·36	4·55 ± 0·22	0·78 ± 0·36
20	4·78 ± 0·16	0·31 ± 0·23	5·19 ± 0·38	2·17 ± 0·85
21	4·99 ± 0·10	0·47 ± 0·23	4·54 ± 0·57	0·69 ± 0·35
22	5·11 ± 0·12	0·59 ± 0·25	4·02 ± 0·24	0·90 ± 0·45
23	5·16 ± 0·16	0·67 ± 0·20	3·70 ± 0·38	0·45 ± 0·33
24	5·14 ± 0·35	0·34 ± 0·13	3·28 ± 0·22	0·78 ± 0·22
25	5·12 ± 0·08	0·36 ± 0·10	3·81 ± 0·25	0·47 ± 0·32
26	4·99 ± 0·28	0·40 ± 0·14	3·54 ± 0·08	0·60 ± 0·33

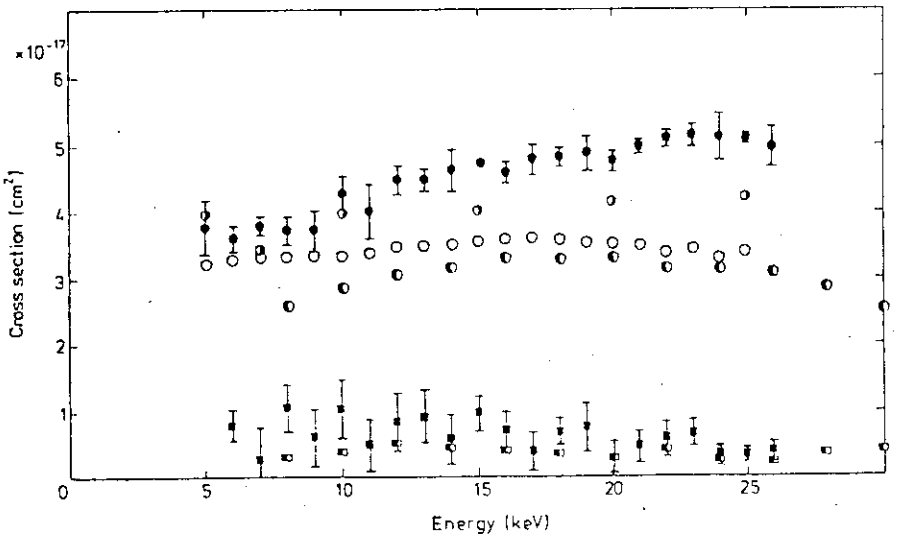

Cross sections $\sigma_{2p}(H_2)$ and $\sigma_{2s}(H_2)$ for formation of H(2p) and H(2s) atoms in He^+–H_2 collisions. $\sigma_{2p}(H_2)$: ● present results; ◑ Young *et al* (1968); ◐ Andreev *et al* (1967); ○ van Zyl *et al* (1967). $\sigma_{2s}(H_2)$: ■ present results; ◧ Andreev *et al* (1967).

FIG.57

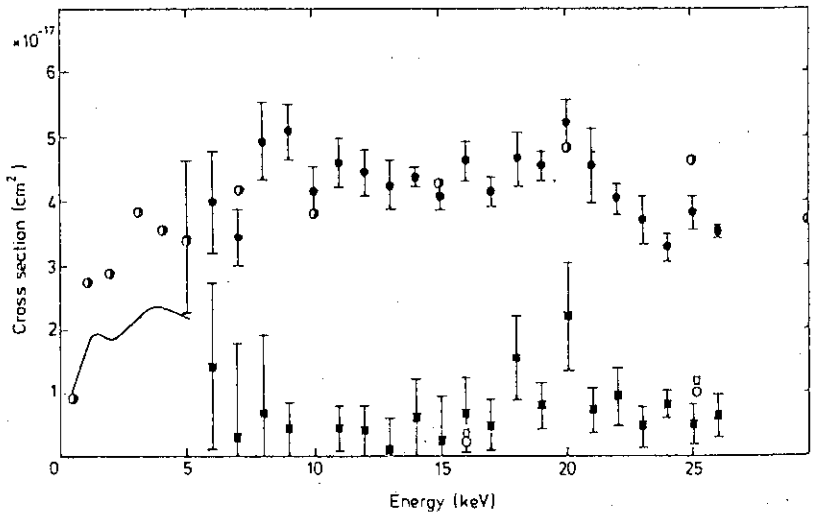

Cross sections σ_{2p}(H) and σ_{2s}(H) for formation of H(2p) and H(2s) atoms in He^+-H collisions. σ_{2p}(H): ● present results; ◑ Young *et al* (1968); —— Fayeton *et al* (1976) theory; ○ Flannery (1969) theory. σ_{2s}(H): ■ present results; □ Flannery (1969) theory.

FIG.58

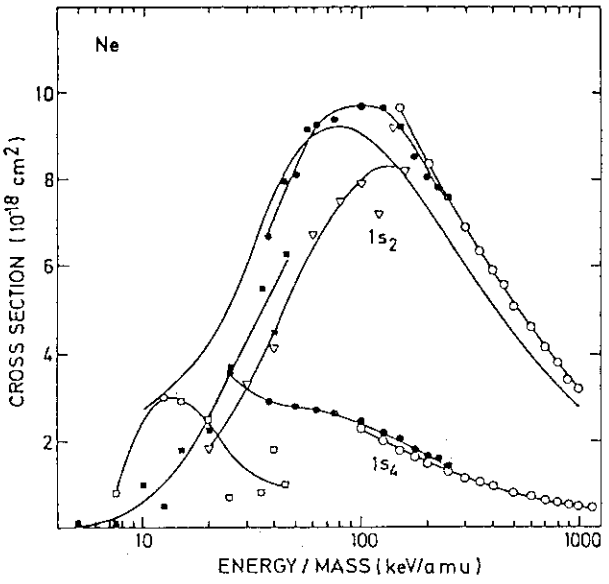

Absolute cross sections for the $1s_2$- and $1s_4$-level in neon: *a*) emission cross sections: —●— present He^+ impact results, —○— Hippler and Schartner (H^+ impact) [1]. *b*) Excitation cross sections: —▽— York et al. [2], H^+ impact, —■— and —□— York et al. [2], He^+ impact results for the $1s_2$- and the sum of the $1s_3$-, $1s_4$-, and $1s_5$-levels respectively, —— Albat et al. (theory) [11]

FIG.59

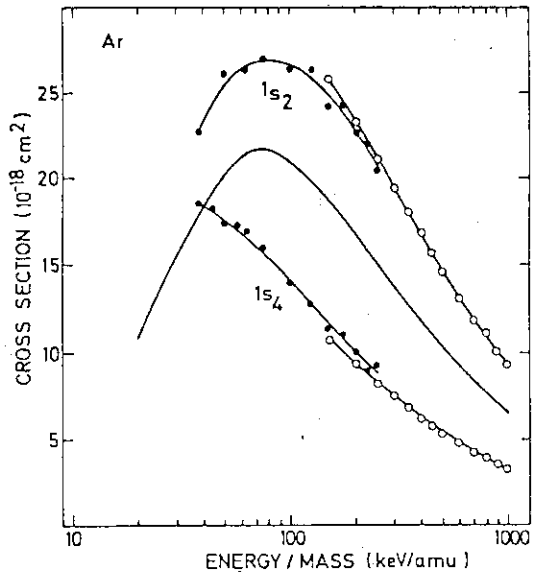

Absolute cross sections for the $1s_2$- and $1s_4$-level in argon: *a*) emission cross sections: —●— present He^+ impact results, —○— Hippler and Schartner (H^+ impact) [1]. *b*) Excitation cross sections: —— Albat et al. (theory) [11]

FIG.60

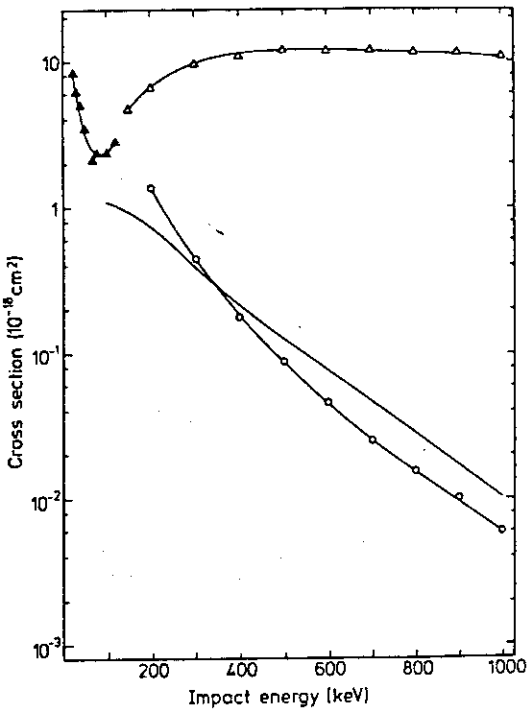

Cross section for the (*a*) direct and (*b*) charge-exchange excitation of the 2^1P level in He^+–He collisions as a function of the impact energy. (*a*) Δ, present results; ▲, Pol *et al* (1973); (*b*) ○, present results; ——, Winter and Lin (1975).

FIG.61

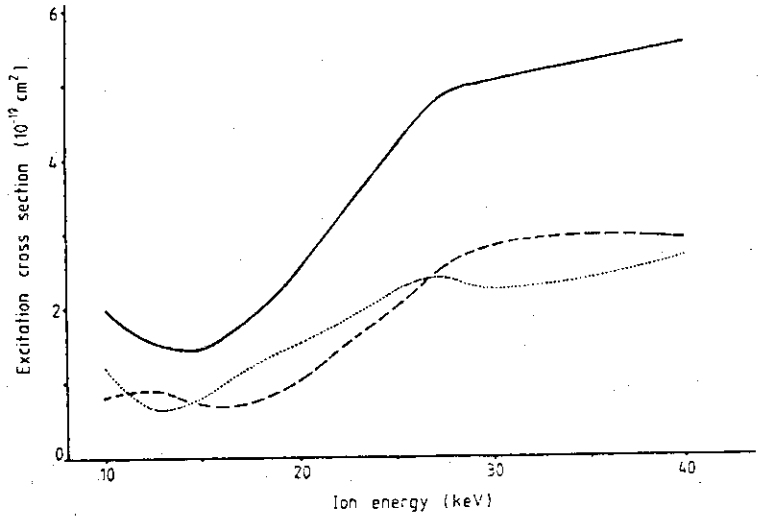

Total excitation cross section (full curve) of the 1s4d $^1D_2$ level for He^+–He collisions including direct (broken curve) and charge transfer (dotted curve) processes according to de Heer *et al* (Thomas 1972).

FIG.62

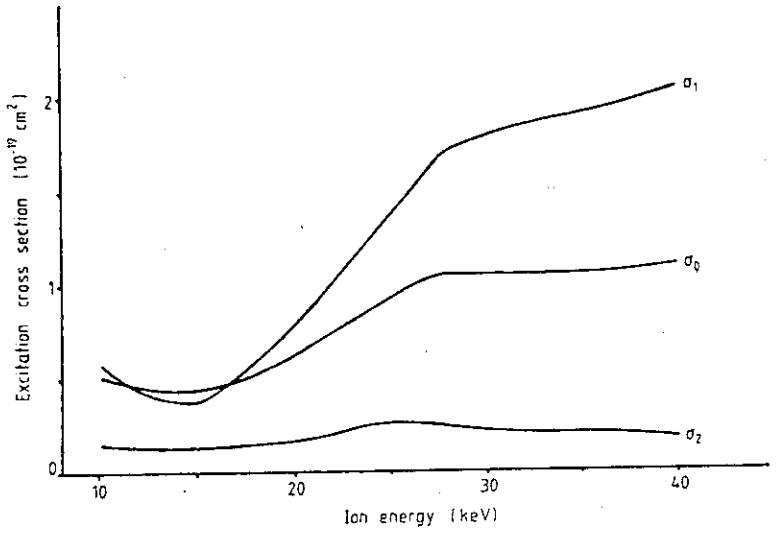

Excitation cross sections $\sigma_{|m|}$ of Zeeman sublevels of the 1s4d $^1D_2$ level.

FIG.63

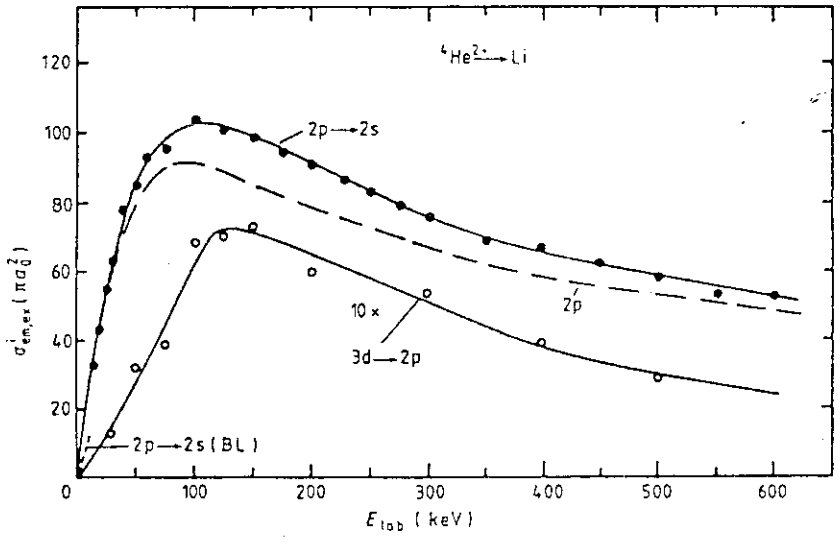

Cross sections for emission of Li I 2p → 2s, Li I (3d → 2p) and excitation of Li I 2p in the case of He^{2+} on Li. The results of Barrett and Leventhal (1981) are referred to as BL.

FIG.64

TABLE 16

Cross sections for emission and excitation of Li by $^4He^{2+}$ impact in units of πa_0^2.

Energy (laboratory) (keV)	$\sigma^i_{em}(2p \rightarrow 2s)$	$\sigma^i_{ex}(2p)$	$\sigma^i_{em}(3d \rightarrow 2p)$
15	33.3	32.1	
20	43.5	41.9	
25	55.1	53.3	
30	63.1	60.5	1.3
40	78.8	74.9	
50	84.6	79.5	3.2
60	92.8	86.6	
75	95.0	86.8	3.9
100	103	92.1	6.9
125	101	87.5	7.1
150	99.1	86.3	7.3
175	94.3	82.1	
200	90.7	79.0	6.0
225	86.3	75.5	
250	82.3	72.1	
275	79.0	69.3	
300	75.2	66.3	5.4
350	68.0	60.2	
400	66.3	59.6	3.9
450	62.3	56.4	
500	58.5	53.2	2.8
550	53.7	49.0	
600	52.9	48.5	

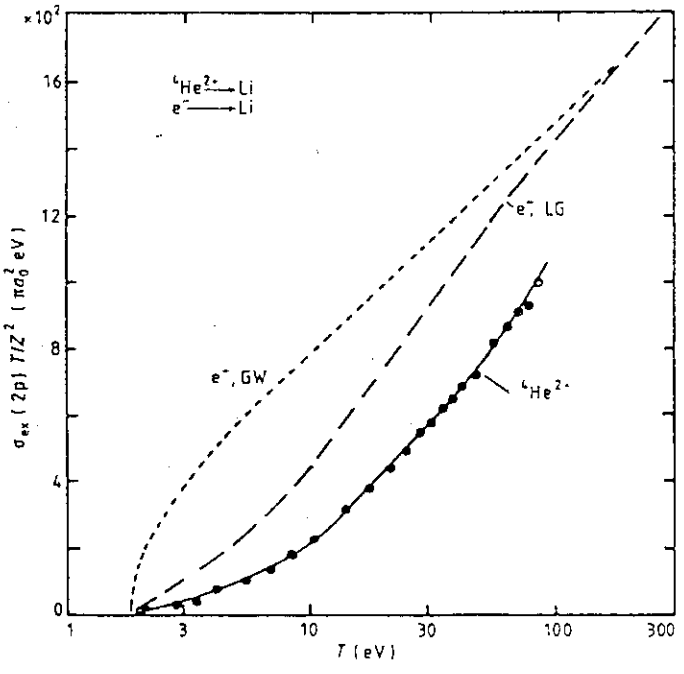

Comparison of Li I 2p excitation by He^{2+} and e^- impact. $T = \frac{1}{2}m_e v^2$ (m_e is the electron mass, v is the velocity of the projectile). Z is the charge of the projectile. The curves are: LG, experiment of Leep and Gallagher (1974); GW, Born theory of Greene and Williamson (1974).

FIG.65

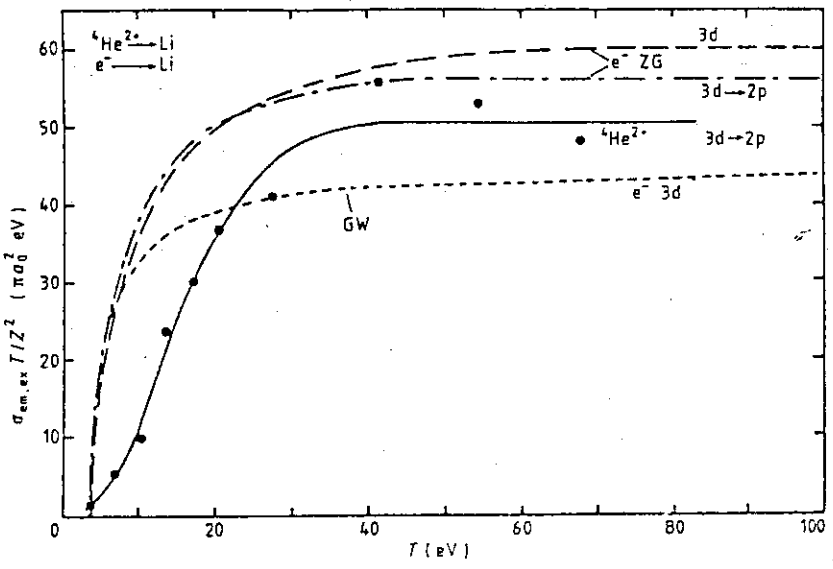

Comparison of Li I 3d excitation (or 3d→2p emission) induced by He^{2+} and e^- impact. For symbols also see caption to figure 3. The results of Zajonc and Gallagher (1979) are referred to as ZG. This curve for 3d excitation is derived from that of 3d→2p emission, correcting for cascade and polarisation effects. Finally, GW are the Born theory results of Greene and Williamson (1974).

FIG.66

TABLE 17

Differential cross sections for excitation of atomic hydrogen to the $n=2$ state by helium-ion impact. (Angles and cross sections are in center-of-mass units. The ion impact energies are given in laboratory units. The $[d\sigma/d\Omega\,(\mathrm{cm}^2/\mathrm{sr})]_{fm}$ are the results of the forward modeling procedures discussed in the text.)

Angle (c.m.) (10^{-3} rad)	15 keV (lab) $\frac{d\sigma}{d\Omega}\left(\frac{\mathrm{cm}^2}{\mathrm{sr}}\right)$	20 keV (lab) $\frac{d\sigma}{d\Omega}\left(\frac{\mathrm{cm}^2}{\mathrm{sr}}\right)$	25 keV (lab) $\frac{d\sigma}{d\Omega}\left(\frac{\mathrm{cm}^2}{\mathrm{sr}}\right)$
0.0	$(1.4 \pm 0.4) \times 10^{-12}$	$(4.0 \pm 2.0) \times 10^{-12}$	$(5.8 \pm 2.1) \times 10^{-12}$
0.4	$(1.0 \pm 0.3) \times 10^{-12}$	$(2.3 \pm 1.2) \times 10^{-12}$	$(3.4 \pm 1.3) \times 10^{-12}$
0.8	$(9.7 \pm 2.2) \times 10^{-13}$	$(1.4 \pm 0.4) \times 10^{-12}$	$(1.9 \pm 0.9) \times 10^{-12}$
1.3	$(8.9 \pm 2.6) \times 10^{-13}$	$(1.1 \pm 0.3) \times 10^{-12}$	$(1.4 \pm 0.7) \times 10^{-12}$
1.7	$(7.5 \pm 2.1) \times 10^{-13}$	$(9.0 \pm 2.9) \times 10^{-13}$	$(1.2 \pm 0.7) \times 10^{-12}$
2.1	$(6.9 \pm 2.3) \times 10^{-13}$	$(9.3 \pm 2.9) \times 10^{-13}$	$(1.1 \pm 0.7) \times 10^{-12}$
2.5	$(6.7 \pm 2.1) \times 10^{-13}$	$(8.1 \pm 2.8) \times 10^{-13}$	$(9.4 \pm 5.4) \times 10^{-13}$
3.3	$(5.4 \pm 2.5) \times 10^{-13}$	$(5.6 \pm 1.7) \times 10^{-13}$	$(6.2 \pm 3.8) \times 10^{-13}$
4.2	$(3.9 \pm 1.6) \times 10^{-13}$	$(4.1 \pm 1.3) \times 10^{-13}$	$(4.0 \pm 2.7) \times 10^{-13}$
5.0	$(3.5 \pm 1.4) \times 10^{-13}$	$(2.9 \pm 1.2) \times 10^{-13}$	$(2.8 \pm 1.9) \times 10^{-13}$
5.8	$(2.6 \pm 1.0) \times 10^{-13}$	$(1.9 \pm 1.0) \times 10^{-13}$	$(1.9 \pm 1.4) \times 10^{-13}$
6.7	$(2.1 \pm 0.8) \times 10^{-13}$	$(1.6 \pm 1.0) \times 10^{-13}$	$(1.0 \pm 0.8) \times 10^{-13}$
7.5	$(1.8 \pm 0.6) \times 10^{-13}$	$(1.1 \pm 0.7) \times 10^{-13}$	$(1.1 \pm 0.7) \times 10^{-13}$

Angle (c.m.) (10^{-3} rad)	30 keV (lab) $\frac{d\sigma}{d\Omega}\left(\frac{\mathrm{cm}^2}{\mathrm{sr}}\right)$	40 keV (lab) $\frac{d\sigma}{d\Omega}\left(\frac{\mathrm{cm}^2}{\mathrm{sr}}\right)$	45 keV (lab) $\frac{d\sigma}{d\Omega}\left(\frac{\mathrm{cm}^2}{\mathrm{sr}}\right)$
0.0	$(1.5 \pm 0.7) \times 10^{-11}$	$(4.5 \pm 2.4) \times 10^{-11}$	$(3.2 \pm 0.5) \times 10^{-11}$
0.4	$(7.2 \pm 2.5) \times 10^{-12}$	$(1.6 \pm 0.6) \times 10^{-11}$	$(1.3 \pm 0.2) \times 10^{-11}$
0.8	$(2.7 \pm 1.1) \times 10^{-12}$	$(4.8 \pm 2.4) \times 10^{-12}$	$(4.5 \pm 1.0) \times 10^{-12}$
1.3	$(1.6 \pm 0.8) \times 10^{-12}$	$(2.1 \pm 0.9) \times 10^{-12}$	$(1.6 \pm 0.5) \times 10^{-12}$
1.7	$(1.3 \pm 0.6) \times 10^{-12}$	$(1.2 \pm 0.6) \times 10^{-12}$	$(8.0 \pm 2.9) \times 10^{-13}$
2.1	$(1.0 \pm 0.6) \times 10^{-12}$	$(8.5 \pm 3.3) \times 10^{-13}$	$(4.5 \pm 1.9) \times 10^{-13}$
2.5	$(8.7 \pm 4.7) \times 10^{-13}$	$(6.3 \pm 2.4) \times 10^{-13}$	$(3.1 \pm 1.3) \times 10^{-13}$
3.3	$(5.3 \pm 2.8) \times 10^{-13}$	$(4.0 \pm 2.1) \times 10^{-13}$	$(1.5 \pm 0.7) \times 10^{-13}$
4.2	$(2.9 \pm 1.7) \times 10^{-13}$	$(2.0 \pm 0.9) \times 10^{-13}$	$(8.9 \pm 7.9) \times 10^{-14}$
5.0	$(1.7 \pm 0.9) \times 10^{-13}$	$(1.1 \pm 0.7) \times 10^{-13}$	$(4.3 \pm 2.9) \times 10^{-14}$
5.8	$(1.4 \pm 0.7) \times 10^{-13}$	$(1.2 \pm 1.0) \times 10^{-13}$	$(1.8 \pm 1.6) \times 10^{-14}$
6.7	$(8.3 \pm 4.3) \times 10^{-14}$		$(1.7 \pm 1.4) \times 10^{-14}$
7.5	$(6.8 \pm 5.8) \times 10^{-14}$		

Angle (c.m.) (10^{-3} rad)	50 keV (lab) $\frac{d\sigma}{d\Omega}\left(\frac{\mathrm{cm}^2}{\mathrm{sr}}\right)$	$\left[\frac{d\sigma}{d\Omega}\left(\frac{\mathrm{cm}^2}{\mathrm{sr}}\right)\right]_{fm}$
0.0	$(8.0 \pm 3.6) \times 10^{-11}$	1.4×10^{-10}
0.4	$(2.8 \pm 1.3) \times 10^{-11}$	3.1×10^{-11}
0.8	$(6.6 \pm 4.1) \times 10^{-12}$	4.4×10^{-12}
1.3	$(2.0 \pm 1.6) \times 10^{-12}$	1.2×10^{-12}
1.7	$(8.7 \pm 6.2) \times 10^{-13}$	8.0×10^{-13}
2.1	$(5.0 \pm 3.0) \times 10^{-13}$	4.8×10^{-13}
2.5	$(3.3 \pm 2.0) \times 10^{-13}$	3.4×10^{-13}
3.3	$(1.6 \pm 1.0) \times 10^{-13}$	1.9×10^{-13}
4.2	$(8.5 \pm 5.6) \times 10^{-14}$	9.6×10^{-14}
5.0	$(4.5 \pm 2.5) \times 10^{-14}$	4.4×10^{-14}
5.8	$(1.3 \pm 0.6) \times 10^{-14}$	1.3×10^{-14}
6.7	$(4.4 \pm 2.5) \times 10^{-15}$	4.8×10^{-15}
7.5	$(2.6 \pm 1.9) \times 10^{-15}$	2.5×10^{-15}

Angle (c.m.) (10^{-3} rad)	60 keV (lab) $\frac{d\sigma}{d\Omega}\left(\frac{\mathrm{cm}^2}{\mathrm{sr}}\right)$	$\left[\frac{d\sigma}{d\Omega}\left(\frac{\mathrm{cm}^2}{\mathrm{sr}}\right)\right]_{fm}$
0.0	$(1.0 \pm 0.1) \times 10^{-10}$	1.8×10^{-10}
0.4	$(2.7 \pm 0.4) \times 10^{-11}$	2.3×10^{-11}
0.8	$(4.7 \pm 0.9) \times 10^{-12}$	1.6×10^{-12}
1.3	$(1.4 \pm 0.3) \times 10^{-12}$	9.1×10^{-13}
1.7	$(5.1 \pm 0.7) \times 10^{-13}$	4.6×10^{-13}
2.1	$(2.7 \pm 0.5) \times 10^{-13}$	3.0×10^{-13}
2.5	$(1.8 \pm 0.6) \times 10^{-13}$	1.9×10^{-13}
3.3	$(8.0 \pm 0.4) \times 10^{-14}$	8.4×10^{-14}
4.2	$(3.0 \pm 1.3) \times 10^{-14}$	3.0×10^{-14}
5.0	$(2.9 \pm 0.3) \times 10^{-14}$	2.3×10^{-14}
5.8	$(9.6 \pm 0.8) \times 10^{-15}$	1.4×10^{-14}

Angle (c.m.) (10^{-3} rad)	75 keV (lab) $\frac{d\sigma}{d\Omega}\left(\frac{\mathrm{cm}^2}{\mathrm{sr}}\right)$	$\left[\frac{d\sigma}{d\Omega}\left(\frac{\mathrm{cm}^2}{\mathrm{sr}}\right)\right]_{fm}$
0.0	$(1.4 \pm 0.4) \times 10^{-10}$	5.6×10^{-10}
0.4	$(3.9 \pm 0.3) \times 10^{-11}$	2.5×10^{-11}
0.8	$(7.6 \pm 2.7) \times 10^{-12}$	1.2×10^{-12}
1.3	$(1.5 \pm 0.5) \times 10^{-12}$	4.6×10^{-13}
1.7	$(3.9 \pm 1.4) \times 10^{-13}$	3.0×10^{-13}
2.1	$(1.6 \pm 0.9) \times 10^{-13}$	1.9×10^{-13}
2.5	$(8.6 \pm 5.4) \times 10^{-14}$	1.2×10^{-13}
3.3	$(4.6 \pm 3.2) \times 10^{-14}$	5.2×10^{-14}
4.2	$(2.5 \pm 2.3) \times 10^{-14}$	2.0×10^{-14}
5.0	$(2.3 \pm 1.4) \times 10^{-14}$	1.1×10^{-14}
5.8	$(1.8 \pm 1.4) \times 10^{-14}$	2.9×10^{-14}

Angle (c.m.) (10^{-3} rad)	100 keV (lab) $\frac{d\sigma}{d\Omega}\left(\frac{\mathrm{cm}^2}{\mathrm{sr}}\right)$	$\left[\frac{d\sigma}{d\Omega}\left(\frac{\mathrm{cm}^2}{\mathrm{sr}}\right)\right]_{fm}$
0.0	$(1.1 \pm 0.5) \times 10^{-10}$	7.9×10^{-10}
0.4	$(3.7 \pm 0.5) \times 10^{-11}$	2.1×10^{-11}
0.8	$(9.1 \pm 4.2) \times 10^{-12}$	1.2×10^{-12}
1.3	$(2.0 \pm 1.4) \times 10^{-12}$	2.2×10^{-13}
1.7	$(4.3 \pm 3.2) \times 10^{-13}$	6.0×10^{-14}
2.1	$(8.0 \pm 6.7) \times 10^{-14}$	3.7×10^{-14}
2.5	$(2.4 \pm 1.6) \times 10^{-14}$	2.6×10^{-14}
3.3	$(1.1 \pm 0.4) \times 10^{-14}$	1.1×10^{-14}
4.2	$(5.3 \pm 3.8) \times 10^{-15}$	5.5×10^{-15}
5.0	$(2.9 \pm 3.5) \times 10^{-15}$	3.2×10^{-15}
5.8	$(1.8 \pm 1.5) \times 10^{-15}$	9.5×10^{-16}

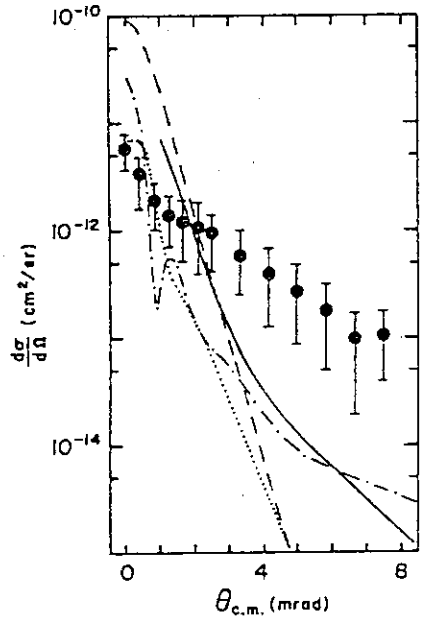

Angular differential cross section at 25 keV. The solid circles with error bars are the present results. The error bars represent one standard deviation from the mean and include only random statistical error. The curves are the theoretical results: ——— Symmetrized first-order Glauber (Ref. 5); — — Born (Ref. 8); —·— Four-state eikonal close coupling (Ref. 8); ..... Two-state eikonal close coupling (Ref. 8).

FIG.67

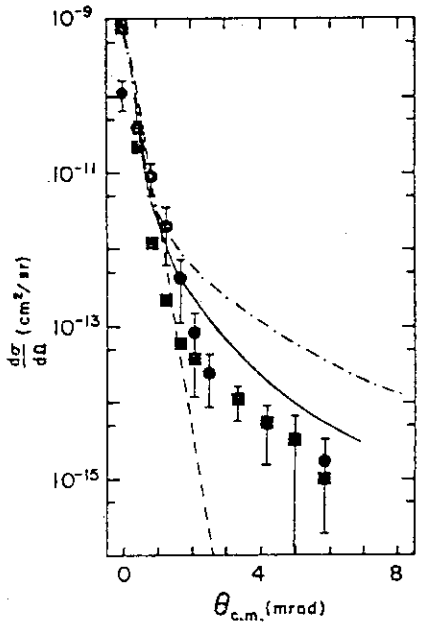

Angular differential cross section at 100 keV. The solid circles with error bars are the present results. The solid squares are the present results obtained using the forward modeling technique discussed in the text. The error bars represent one standard deviation from the mean and include only random statistical error. The curves are the theoretical results: ——— Symmetrized first-order Glauber (Ref. 5); — — Born (Ref. 8); —·— Four-state eikonal close coupling (Ref. 8).

FIG.68

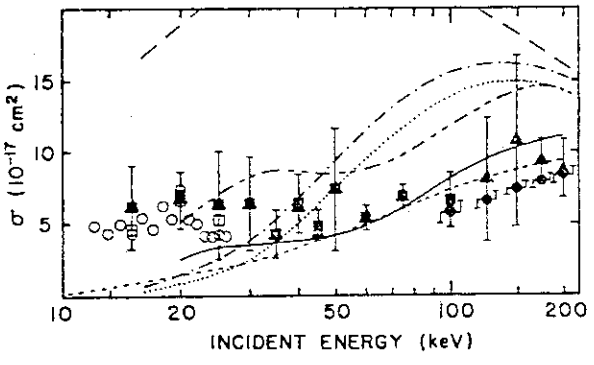

Total cross section results. The symbols represent experimental results: ■ Present total cross section results (σ); ▲ Present apparent total cross section (s); ● 1976 results (Ref. 19); ○ Young *et al.* (Ref. 22); ○ McKee *et al.* (Ref. 24). The curves represent theoretical results: — — — First-order Glauber (Ref. 6); ——— Symmetrized first-order Glauber (Ref. 5); — — Born (Refs. 7 and 8); —·— Four-state eikonal close coupling (Refs. 7 and 8); ..... Two-state eikonal close coupling (Refs. 7 and 8); — — — — VPSA (Ref. 27).

FIG.69

TABLE 18

Apparent angular differential cross sections. (Angle and cross sections are in center-of-mass coordinates.)

Laboratory incident energy θ(rad)	15 keV $\frac{ds}{d\Omega}$ (cm²/sr)	20 keV $\frac{ds}{d\Omega}$ (cm²/sr)	25 keV $\frac{ds}{d\Omega}$ (cm²/sr)	30 keV $\frac{ds}{d\Omega}$ (cm²/sr)
0	1.1×10^{-12}	2.4×10^{-12}	2.7×10^{-12}	6.5×10^{-12}
4.16×10^{-4}	9.6×10^{-13}	1.9×10^{-12}	2.3×10^{-12}	5.0×10^{-12}
8.33×10^{-4}	8.8×10^{-13}	1.4×10^{-12}	1.7×10^{-12}	2.7×10^{-12}
1.25×10^{-3}	8.1×10^{-13}	1.1×10^{-12}	1.3×10^{-12}	1.6×10^{-12}
1.67×10^{-3}	6.9×10^{-13}	8.9×10^{-13}	9.9×10^{-13}	1.2×10^{-12}
2.08×10^{-3}	6.1×10^{-13}	8.7×10^{-13}	8.4×10^{-13}	9.0×10^{-13}
2.50×10^{-3}	5.8×10^{-13}	7.7×10^{-13}	7.6×10^{-13}	7.7×10^{-13}
3.33×10^{-3}	4.7×10^{-13}	5.6×10^{-13}	5.4×10^{-13}	4.9×10^{-13}
4.16×10^{-3}	3.5×10^{-13}	4.2×10^{-13}	3.7×10^{-13}	2.9×10^{-13}
5.00×10^{-3}	3.4×10^{-13}	3.0×10^{-13}	2.6×10^{-13}	1.7×10^{-13}
5.83×10^{-3}	2.5×10^{-13}	2.1×10^{-13}	1.9×10^{-13}	1.3×10^{-13}
6.66×10^{-3}	2.1×10^{-13}	1.6×10^{-13}	1.0×10^{-13}	8.8×10^{-14}
7.49×10^{-3}	1.8×10^{-13}	1.1×10^{-13}	9.4×10^{-14}	6.5×10^{-14}

θ(rad)	35 keV $\frac{ds}{d\Omega}$ (cm²/sr)	40 keV $\frac{ds}{d\Omega}$ (cm²/sr)	45 keV $\frac{ds}{d\Omega}$ (cm²/sr)	50 keV $\frac{ds}{d\Omega}$ (cm²/sr)
0	5.5×10^{-12}	1.6×10^{-11}	8.7×10^{-12}	2.8×10^{-11}
4.16×10^{-4}	4.3×10^{-12}	9.8×10^{-12}	7.1×10^{-12}	2.0×10^{-11}
8.33×10^{-4}	2.5×10^{-12}	4.4×10^{-12}	4.3×10^{-12}	9.7×10^{-12}
1.25×10^{-3}	1.3×10^{-12}	2.2×10^{-12}	2.1×10^{-12}	3.1×10^{-12}
1.67×10^{-3}	7.9×10^{-13}	1.3×10^{-12}	1.1×10^{-12}	1.1×10^{-12}
2.08×10^{-3}	6.1×10^{-13}	9.0×10^{-13}	5.7×10^{-13}	6.0×10^{-13}
2.50×10^{-3}	4.7×10^{-13}	6.3×10^{-13}	3.8×10^{-13}	3.9×10^{-13}
3.33×10^{-3}	2.7×10^{-13}	3.6×10^{-13}	1.8×10^{-13}	1.9×10^{-13}
4.16×10^{-3}	1.6×10^{-13}	2.0×10^{-13}	9.5×10^{-14}	9.6×10^{-14}
5.00×10^{-3}	9.7×10^{-14}	1.2×10^{-13}	4.9×10^{-14}	4.9×10^{-14}
5.83×10^{-3}	6.2×10^{-14}	7.7×10^{-14}	2.0×10^{-14}	1.6×10^{-14}
6.66×10^{-3}	3.6×10^{-14}		1.6×10^{-14}	5.5×10^{-15}
7.49×10^{-3}				2.6×10^{-15}

θ(rad)	60 keV $\frac{ds}{d\Omega}$ (cm²/sr)	75 keV $\frac{ds}{d\Omega}$ (cm²/sr)	100 keV $\frac{ds}{d\Omega}$ (cm²/sr)	125 keV $\frac{ds}{d\Omega}$ (cm²/sr)
0	2.8×10^{-11}	3.9×10^{-11}	1.8×10^{-11}	7.3×10^{-11}
4.16×10^{-4}	2.0×10^{-11}	2.5×10^{-11}	1.6×10^{-11}	4.1×10^{-11}
8.33×10^{-4}	7.0×10^{-12}	1.0×10^{-11}	9.8×10^{-12}	1.0×10^{-11}
1.25×10^{-3}	2.0×10^{-12}	2.8×10^{-12}	4.5×10^{-12}	1.3×10^{-12}
1.67×10^{-3}	6.8×10^{-13}	7.1×10^{-13}	1.2×10^{-12}	3.2×10^{-13}
2.08×10^{-3}	3.4×10^{-13}	2.7×10^{-13}	2.3×10^{-13}	1.3×10^{-13}
2.50×10^{-3}	2.1×10^{-13}	1.3×10^{-13}	5.8×10^{-14}	5.8×10^{-14}
3.33×10^{-3}	9.4×10^{-14}	5.7×10^{-14}	1.6×10^{-14}	2.6×10^{-14}
4.16×10^{-3}	3.4×10^{-14}	2.7×10^{-14}	6.2×10^{-15}	1.5×10^{-14}
5.00×10^{-3}	2.3×10^{-14}	1.4×10^{-14}	3.6×10^{-15}	
5.83×10^{-3}	1.4×10^{-14}	2.3×10^{-14}	1.3×10^{-15}	

θ(rad)	150 keV $\frac{ds}{d\Omega}$ (cm²/sr)	175 keV $\frac{ds}{d\Omega}$ (cm²/sr)	200 keV $\frac{ds}{d\Omega}$ (cm²/sr)
0	7.9×10^{-11}	4.5×10^{-11}	4.6×10^{-11}
4.16×10^{-4}	4.9×10^{-11}	3.6×10^{-11}	3.5×10^{-11}
8.33×10^{-4}	1.7×10^{-11}	1.7×10^{-11}	1.4×10^{-11}
1.25×10^{-3}	2.6×10^{-12}	3.6×10^{-12}	2.7×10^{-12}
1.67×10^{-3}	4.4×10^{-13}	3.4×10^{-13}	3.8×10^{-13}
2.08×10^{-3}	1.3×10^{-13}	7.2×10^{-14}	4.6×10^{-13}
2.50×10^{-3}	5.0×10^{-14}	4.0×10^{-14}	5.9×10^{-13}
3.33×10^{-3}	1.6×10^{-14}	3.7×10^{-14}	
4.16×10^{-3}	9.5×10^{-15}		

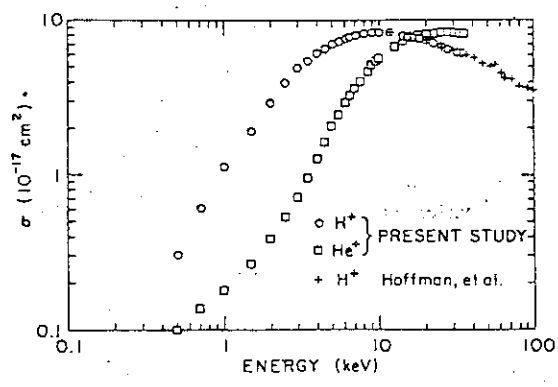

3914-Å emission from N_2 target as a function of projectile energy.

FIG.70

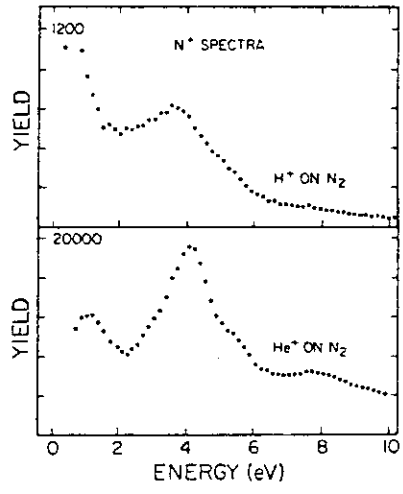

Kinetic energy spectra of N^+ produced by 1-MeV H^+ and He^+.

FIG.71

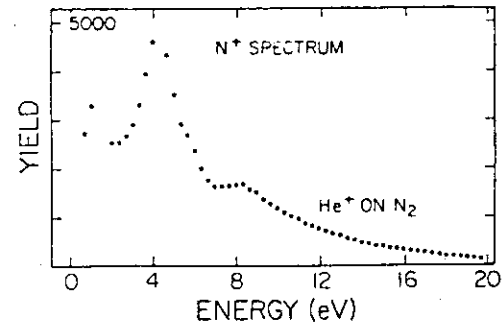

Kinetic energy spectra of N^+ produced by He^+ showing the high-energy tail.

FIG.72

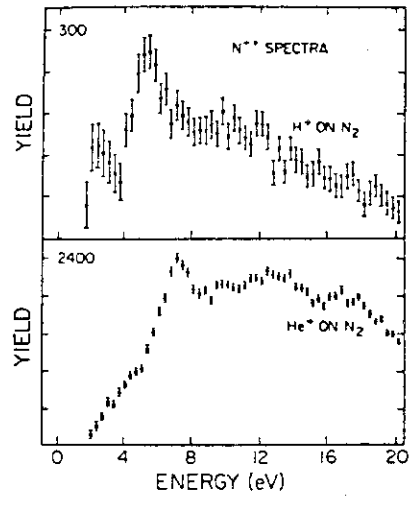

Kinetic energy spectra of N^{++} produced by 1-MeV H^+ and He^{++}.

FIG.73

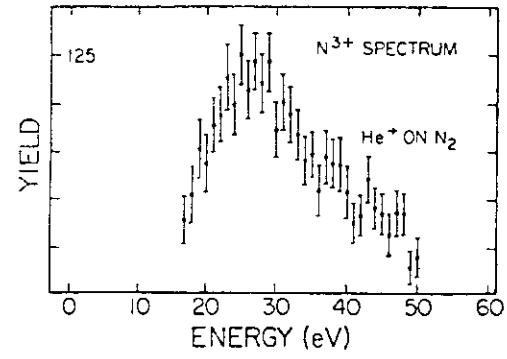

Kinetic energy spectrum of N^{3+} produced by 1-MeV He^+.

FIG.74

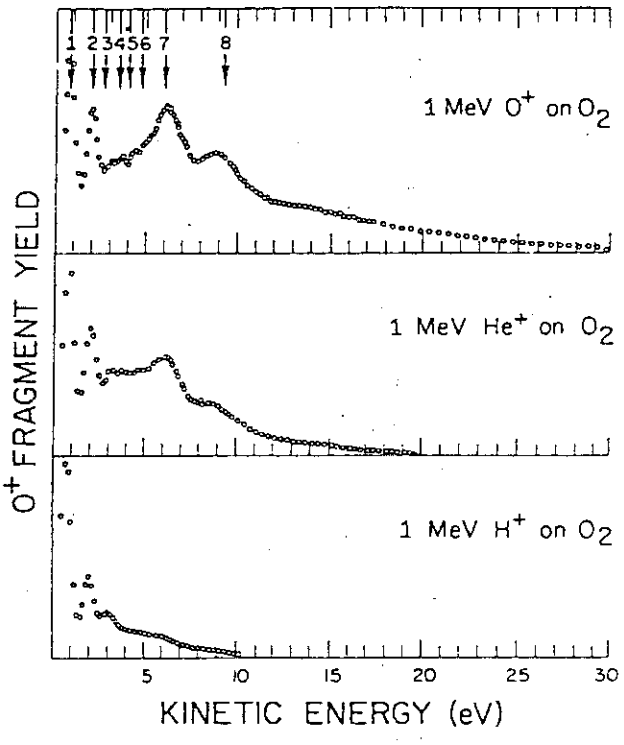

O^+ fragment energy distribution for each kind of projectile. The yield is expressed in arbitrary units. The energy scales for the He^+ and O^+ projectile data have been corrected as described in the text. The energy scale for the data obtained with H^+ projectiles was obtained by normalization as described in the text. The statistical errors are less than the size of the data points. Some adjacent data points were averaged to reduce the density of points in the figure. The data represent a combination of data obtained with different sweep voltages. The total estimated uncertainty is comparable to the size of the data points.

FIG.75

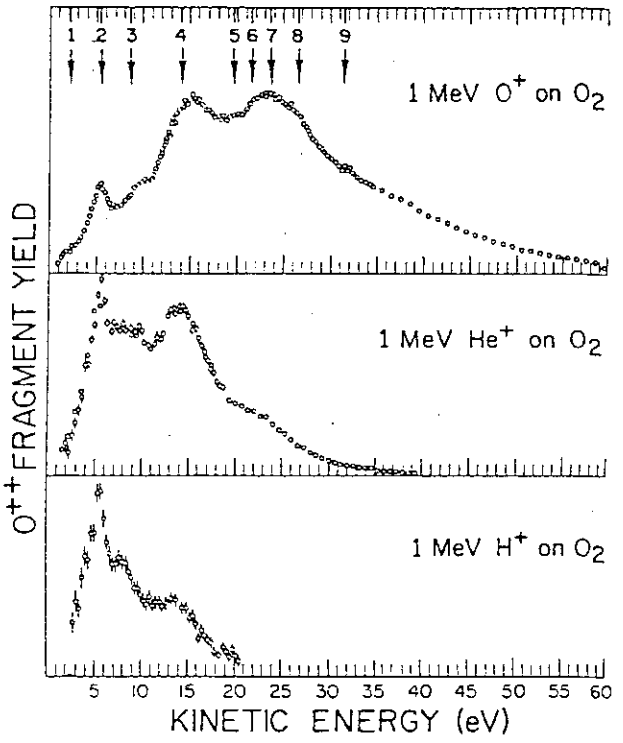

O^+ fragment energy distribution for each kind of projectile. The yield is expressed in arbitrary units. The energy scales for the He^+ and O^+ projectile data have been corrected as described in the text. The energy scale for the data obtained with H^+ projectiles was obtained by normalization as described in the text. The statistical errors, except where indicated, are less than the size of the data points. Some adjacent data points were averaged to reduce the density of points in the figure. The data represent a combination of data obtained with different sweep voltages. The probable error is estimated to be less than 1.5 times the statistical standard devistion.

FIG.76

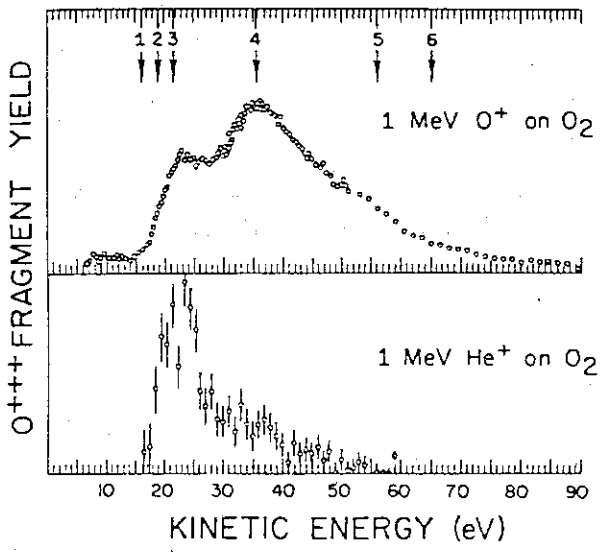

O^{3+} fragment energy distribution for each kind of projectile. The yield is expressed in arbitrary units. The energy scales for the He^+ and O^+ projectile data have been corrected as described in the text. The statistical errors, except where indicated, are less than the size of the data points. Some adjacent data points were averaged to reduce the density of points in the figure. The data represent a combination of data obtained with different sweep voltages. The probable error is estimated to be less than 1.5 times the statistical standard deviation.

FIG.77

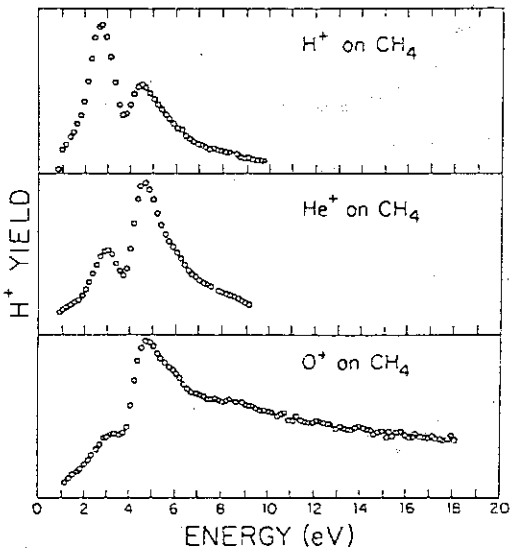

The kinetic-energy spectrum of H^+ fragments from CH_4 bombarded by 1 MeV H^+, He^+, and O^+ projectiles.

FIG.78

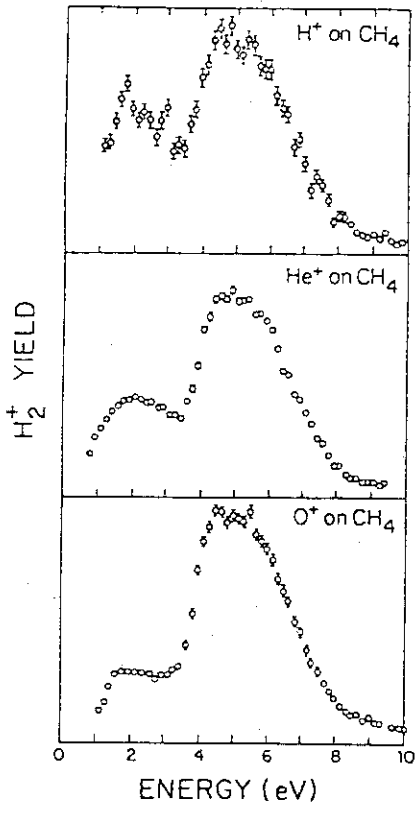

The kinetic-energy spectra of H_2^+ fragments from CH_4 bombarded by 1 MeV H^+, He^+, and O^+ projectiles.

FIG.79

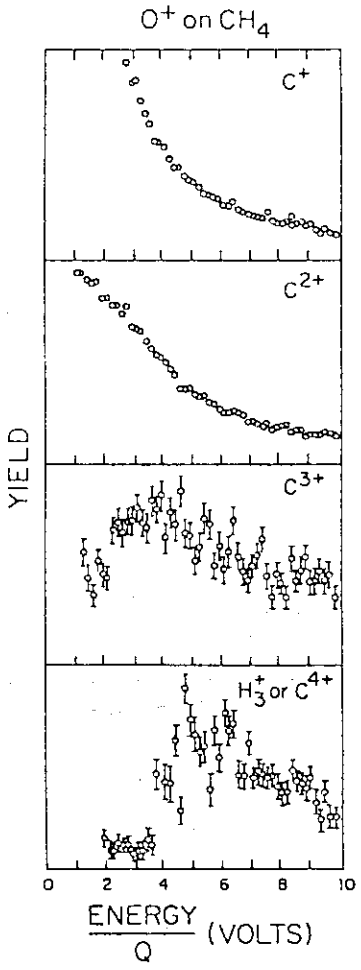

The kinetic-energy spectra of C^+, C^{2+}, C^{3+}, and C^{4+} (and/or H_3^+) produced by bombarding CH_4 with 1 MeV O^+ projectiles. The energy scale is in eV per unit charge of the fragment.

FIG.80

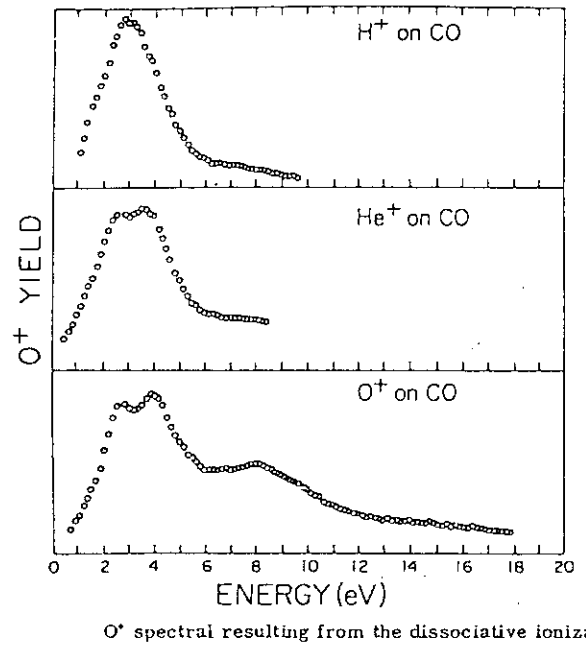

O^+ spectral resulting from the dissociative ionization of CO. Statistical uncertainties are smaller than the symbols. The ordinate full scale values are 137 (H^+), 594 (He^+), and 1332 (O^+).

FIG.82

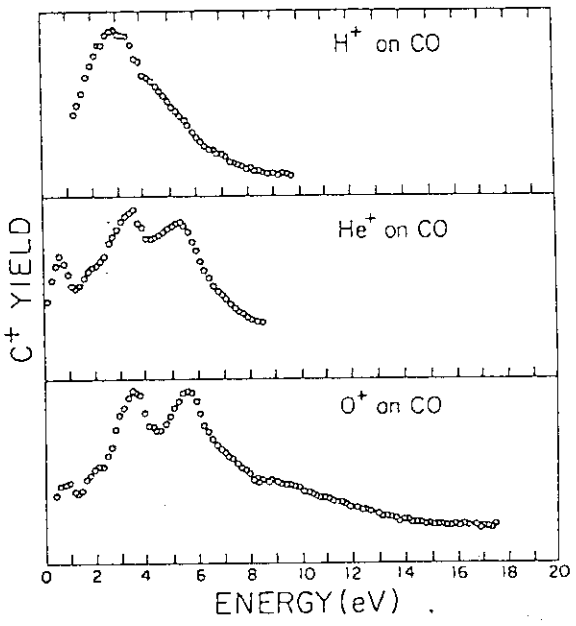

C^+ spectra resulting from the dissociative ionization of CO. Statistical uncertainties are smaller than the symbols. The ordinate full scale values are 114 (H^+), 420 (He^+), and 1000 (O^+).

FIG.81

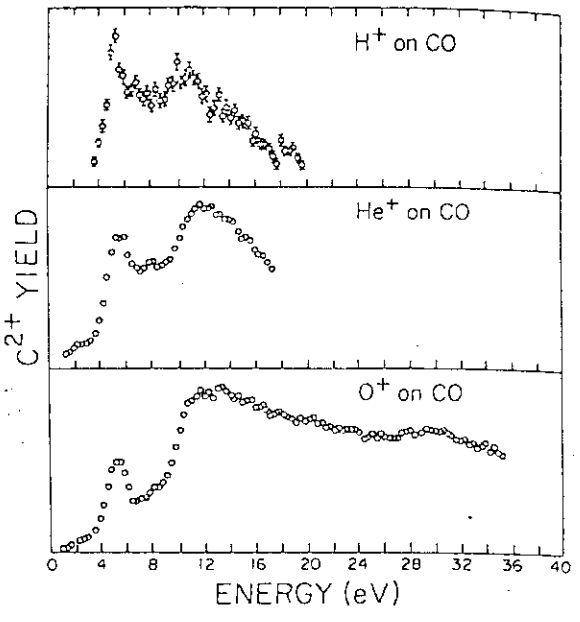

C^{2+} spectra resulting from the dissociative ionization of CO. Statistical uncertainties are indicated by the error flags or are smaller than the symbols. The ordinate full scale values are 8 (H^+), 42 (He^+), and 443 (O^+).

FIG.83

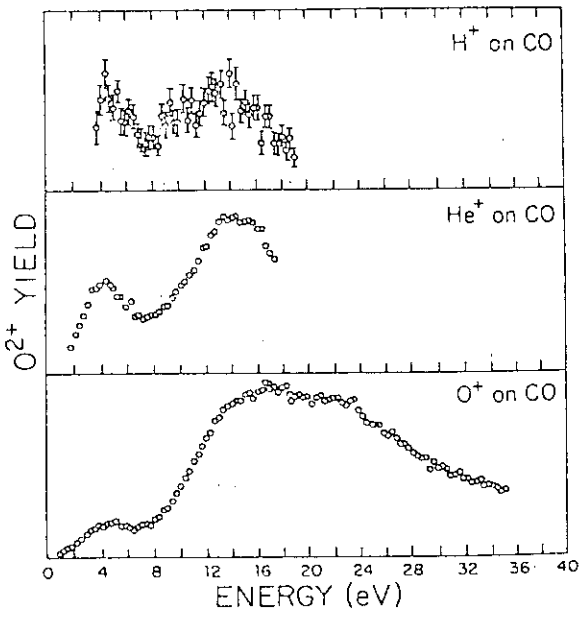

O^{2+} spectra resulting from the dissociative ionization of CO. Statistical uncertainties are indicated by the error flags or are smaller than the symbols. The ordinate full scale values are 2.6 (H^+), 42 (He^+), and 360 (O^+).

FIG.84

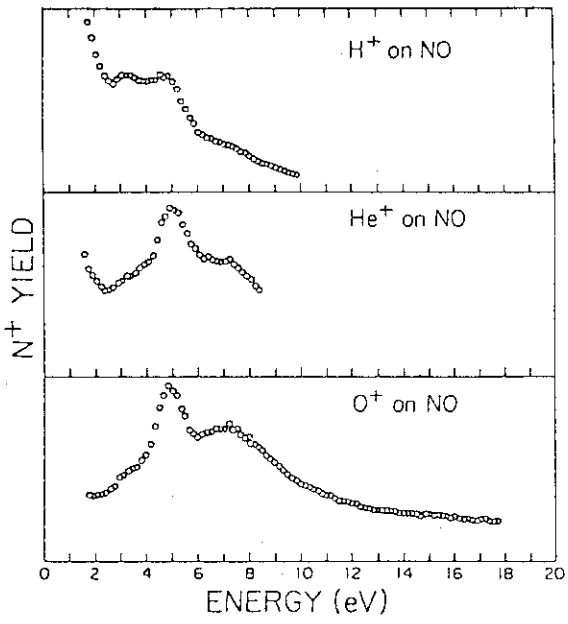

N^+ spectra resulting from the dissociative ionization of CO. Statistical uncertainties are smaller than the symbols. The ordinate full scale values are 40 (H^+), 556 (He^+), and 1000 (O^+).

FIG.85

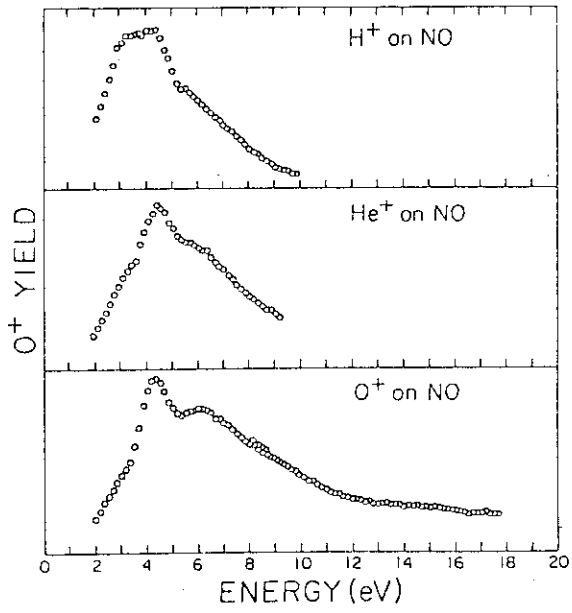

O^+ spectra resulting from the dissociative ionization of CO. Statistical uncertainties are smaller than the symbols. The ordinate full scale values are 35 (H^+), 584 (He^+), and 1167 (O^+).

FIG.86

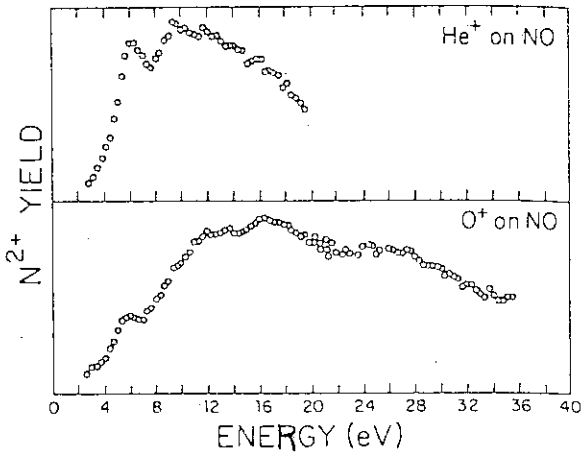

N^{2+} spectra resulting from the dissociative ionization of NO. Statistical uncertainties are smaller than the symbols. The ordinate full scale values are 67 (He^+) and 298 (O^+).

FIG.87

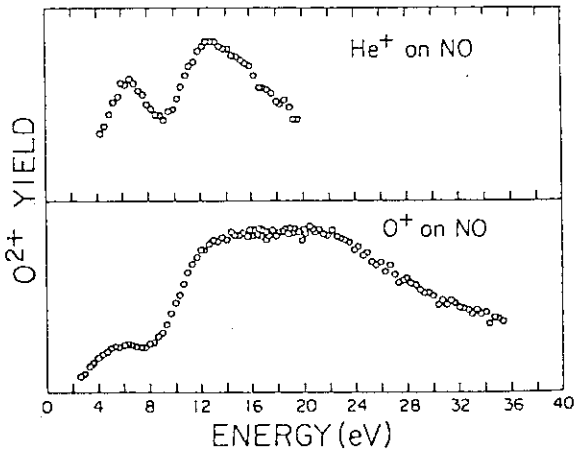

O^{2+} spectra resulting from the dissociative ionization of NO. Statistical uncertainties are smaller than the symbols. The ordinate full scale values are 44 (He^+) and 267 (O^+).

FIG.88

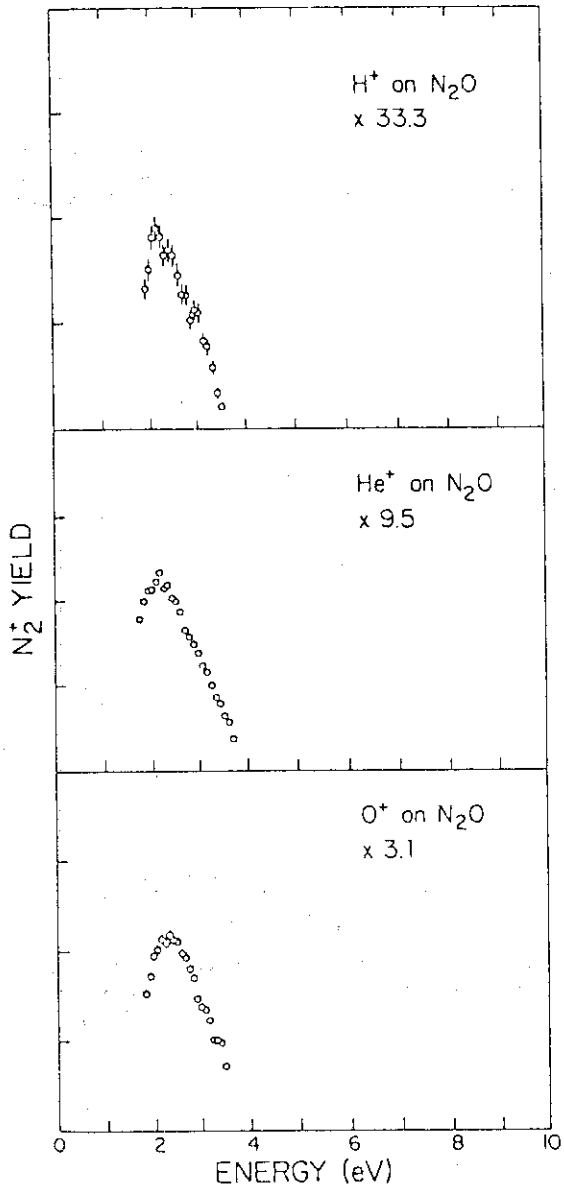

N_2^+ spectra resulting from the dissociative ionization of N_2O. Statistical uncertainties are smaller than the symbols. Actual yields per unit charge and pressure have been multiplied by 33.3 (H^+), 9.5 (He^+), and 3.1 (O^+) to facilitate visual presentation.

FIG.89

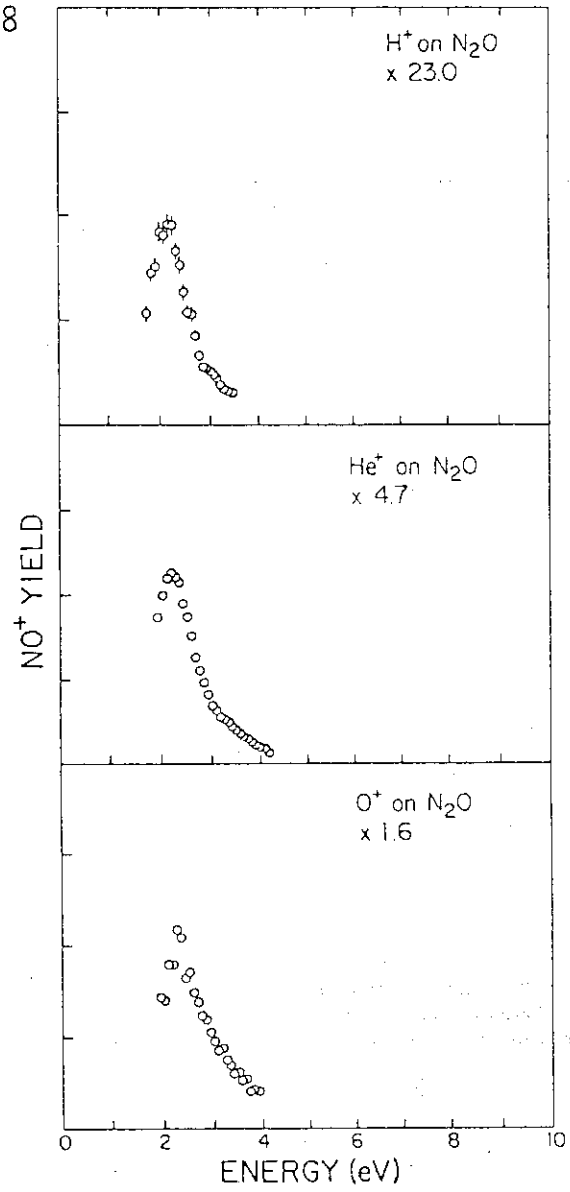

NO^+ spectra resulting from the dissociative ionization of N_2O. Statistical uncertainties are smaller than the symbols. Actual yields per unit charge and pressure have been multiplied by 23.0 (H^+), 4.7 (He^+), and 1.6 (O^+) to facilitate visual presentation.

FIG.90

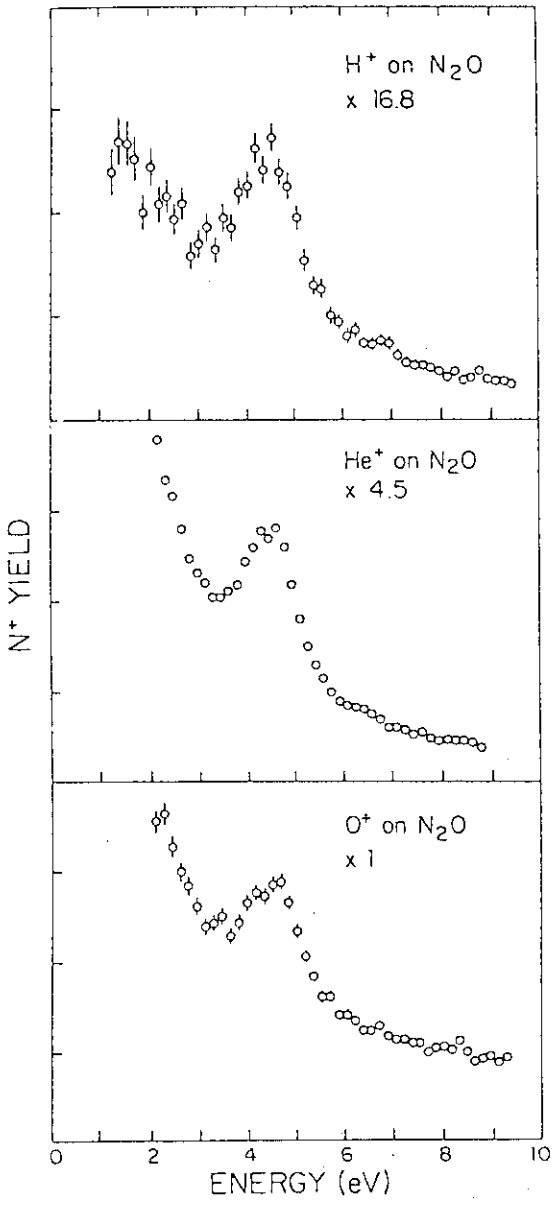

N^+ spectra resulting from the dissociative ionization of N_2O. Statistical uncertainties are smaller than the symbols. Actual yields per unit charge and pressure have been multiplied by 16.8 (H^+), 4.5 (He^+), and 1.0 (O^+) to facilitate visual presentation.

FIG. 91

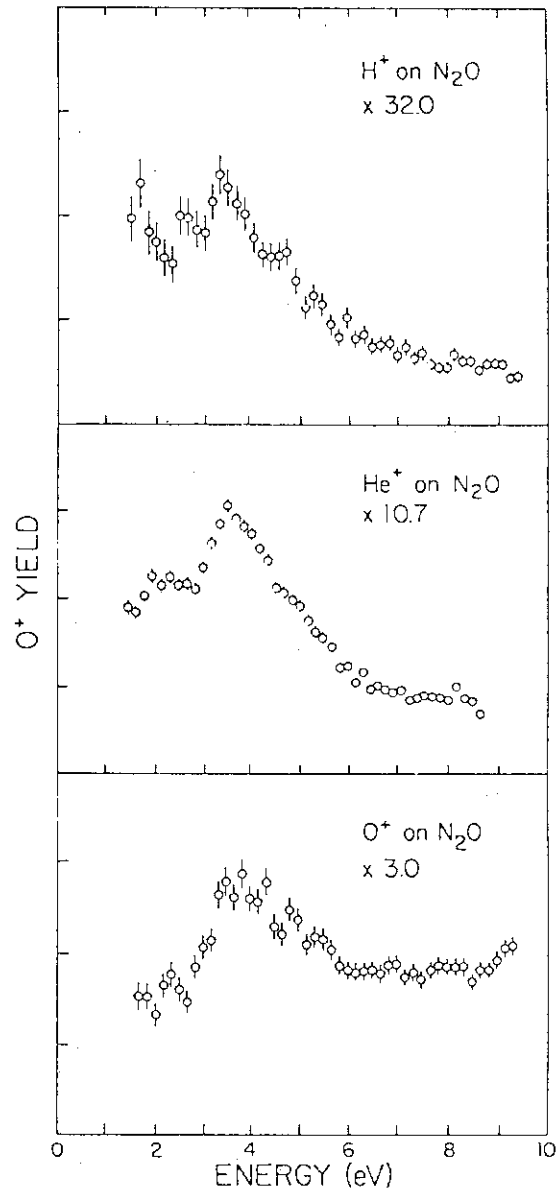

O^+ spectra resulting from the dissociative ionization of N_2O. Statistical uncertainties are smaller than the symbols. Actual yields per unit charge and pressure have been multiplied by 32.0 (H^+), 10.7 (He^+), and 3.0 (O^+) to facilitate visual presentation.

FIG. 92